Aerodynamic Performance of Backward Centrifugal Fan with Rectangular Casing

By

WAR WAR MIN SWE

This dissertation is submitted to Graduate School of Engineering in Fulfilment of the requirements for the degree of Doctor of Philosophy in Engineering.

Graduate School of Engineering
Nagasaki University

2017.07

ACKNOWLEDGEMENT

I would like to express my deepest gratitude to motivator, my supervisor, Prof. Hidechito HAYASHI, Professor, Fluid Dynamic Engineering Laboratory, Department of Science and Technology, Nagasaki University, for his valuable guidance, sympathy and co-operation for providing necessary facilities and sources during the entire period of this research. I would like to special think to him. I am also thankful to Prof. Daisaku Sakaguchi, Prof. Hironobu Ueki, Associate Prof. Tetsuya Okumura, Graduate School of Engineering, Nagasaki university.

I would also like to thank to Mr. Seigo Kaji, Technician, Fluid dynamic laboratory, he provides the equipment and setup for doing experiment.

I would also like to thank to the all students, especially my tutor, Mr. Hiroya MORIMATSU, Master student and Mr.Shingo Terashima, Doctoral student, at Fluid dynamic Laboratory, for giving me the opportunity for carrying out my experiment by co-operating in spite of his busy work schedule took time off to guide me and help me.

I am also thankful to Prof. Shigeru Katamine, President, Nagasaki University and Prof. Yasuhiro Shimizu, Dean, Graduate School of Engineering and School of Engineering, Nagasaki university.

I would like to special think to my respective Union Minister, Ministry of Education, Myanmar, for permitting to attend Ph. D (Project for Enhancement of Engineering Higher Education in Myanmar), three years course hold in Japan.

Finally, I would like to special think to the organization, JICA – Long Term Program, for permitting to join the Project for Enhancement of Engineering Higher Education 2014-2017 at Nagasaki University, in Japan.

Abstract

Small size centrifugal fan is sometimes used not with the conventional scroll casing but with the complicated casing. The section geometry of the casing varies complicatedly in circumference location and sometimes has the very large outlet. In this research, it is cleared the influence of the circumferential variation of the casing geometry to the performance and flow characteristics of the fan. The performance of fan was examined with experiments. And the performance and flow characteristics analyses are carried out with computational simulations. At first, the fan performance and the flow characteristics with complex geometry casing, rectangular casing, are examined with comparing to the conventional scroll casing. The flow characteristics and energy loss are analyzed for the casings. The air flow in centrifugal fan is highly complex with the interaction between the impeller and casing. But the performance of fan with rectangular casing is improved over the design flow rate compared to that of scroll casing fan. Even though, the complex geometry of rectangular casing, the energy loss of the rectangular casing fan is smaller than the scroll casing fan. The energy loss near the outlet of the casing (tongue region in duct) is large in scroll casing. In the rectangular casing, the large outlet section of the casing improved the casing performance at large flow rate. Next, it is analyzed the influence of the circumferential variation of casing geometry to the simulation results. The steady and unsteady simulation are compared for rectangular casing fan that the flow pattern is varied in circumference. It is clear that the flow behavior in the passage of the impeller is quite different in the steady simulation to unsteady one. When the flow separation occurs in the blade passage, the flow separation becomes larger in steady simulation compared to that in unsteady simulation. And the variation of the flow pattern in circumferences direction becomes large in steady simulation. But, when the flow separation doesn’t occur in blade passage, the difference between the steady and unsteady simulation is comparatively small. When the circumferential variation of the fan casing is large, it is pointed out that the steady flow simulation is not suitable, but the unsteady flow simulation is suitable.

TABLE OF CONTENTS

CHAPTER 4 AERODYNAMIC PERFORMANCES AND FLOW CHARACTERISTICS OF CENTRIFUGAL FAN UNDER THE INFLUENCE OF CASING GEOMETERES (RECTANGULAR CASING

LIST OF SYMBOLS

Nomenclature

U	Circumferential Velocity, Instantons velocity	[m/s]
P	Fluid pressure	[Pa]
u	Velocity fluctuating	[m/s]
$\bar{U}$	Mean velocity	[m/s]
$\bar{S}_{ij}$	Mean rate of strain tensor	[-]
S_M	Sum of body forces	[N]
$\boldsymbol{i}$	Position vectors of i, j, k	[-]
V	Control volume	[-]
$\dot{m}_{ip}$	Mass flow rate	[m^3/s]
Δt	Time step	[s]
Δn_j	Discrete outward surface vector	[-]
D_1	Inlet diameter	[mm]
D_2	Outlet diameter	[mm]
H	Exit blade height	[mm]
B	Number of blades	[-]
t	Blade thickness	[mm]
P_1	Pressure on the upstream side	[Pa]
P_2	Pressure on the downstream side	[Pa]
F_r	Area of the throttle hole	[mm^2]
C	Outflow coefficient	[-]
Re_D	Reynold number	[-]
P_t	Total pressure	[mmH_2O]
P_s	Static pressure	[mmH_2O]
ΔP	Differential pressure	[mmH_2O]
N	Rotational speed	[rpm]
T	Impeller torque	[N.m]

ΔP_{t_C} : Casing pressure loss…… [Pa]

ΔP_{t_im} : Impeller pressure rise…… [Pa]

C_p : Static pressure recovery ratio…… [-]

E_p : Energy loss…… [N.m/s]

Greek letters

μ_t : Turbulence viscosity…… [N.s/m^2]

β' : Model constant…… [-]

α : Model constant …… [-]

β : Model constant…… [-]

σ_k : Model constant…… [-]

σ_ω : Model constant…… [-]

ν_t : Eddy-viscosity…… [m^2/s]

β_{1d} : Inlet angle…… [°]

β_{2d} : Outlet angle…… [°]

ε : Expansion coefficient of the gas…… [-]

β : Throttle diameter ratio…… [-]

ρ_w : Density of water…… [kg/m^3]

ρ_a : Density of air…… [kg/m^3]

ϕ : Flow rate coefficient…… [-]

ψ_s : Static pressure coefficient …… [-]

ψ_t : Total pressure coefficient …… [-]

η_s : Efficiency base on static pressure…… [-]

η_t : Efficiency base on total pressure…… [-]

ω : Angular speed…… [rad/s]

η_c : Casing efficiency…… [-]

CHAPTER 1

INTRODUCTION

There are two general classifications of fans: the propeller or axial flow fan and the centrifugal or radial flow fan. In the broadest sense, what sets them apart is how the air passes through the impeller. The propeller or axial flow fan propels the air in an axial direction with a swirling tangential motion created by the rotating impeller blades. In a centrifugal fan, the air enters the impeller axially and is accelerated by the blades and discharged radially. Centrifugal fans use a rotating impeller to increase the velocity of an airstream. As the air moves from the impeller hub to the blade tips, it gains kinetic energy. This kinetic energy is then converted to a static pressure increase as the air slows before entering the discharge. Centrifugal fans can generate relatively high pressures. Centrifugal fans are classified into three basic types per blade configuration: forward curve, backward and radial. For the forward curve, the blade outlet angle ($\beta_{2d} > 90°$) is inclined in the direction of rotation. For the backward curve, the blade outlet angle ($\beta_{2d} < 90°$) is inclined in the opposite direction of rotation. For the radial, the blade outlet angle ($\beta_{2d} = 90°$) is oriented radially. In this research, the centrifugal fan with backward blade is used.

The target of centrifugal fan is used to the air cleaner, the air conditioner, the cooling of the computer and room ventilation. In this study, the centrifugal fan is used in the air cleaner which is shown in Fig. 1.1. The fan is to be use with uniform air flow that the additional functions are closely arranged to the fan. The additional functions are casing geometries, impeller geometries and the gap between the fan and Bellmouth. The casing geometries: i.e., the scroll casing (SC casing) and rectangular casing (RC casing), are important role in performance characteristics of fan. Fan's performance is examined in according to the pressure coefficient, flow coefficient and fan efficiency. The air flow enters the fan from the impeller inlet and then it is accelerated with centrifugal force and it comes out from impeller outlet toward the circumference of fan. That flow is deviated when it goes to the circumference and it can reduce the fan performance, pressure rise. The flow deviation is caused by the casing geometry and thus my research was studied with respect to the following contents.

The turbofan design is usually made with the steady flow simulation. Then the flow out of the impellers are connected to the casing region only at a fixed location in the steady simulation, even though the impeller is rotating and the flow characteristics are varied with the impeller location. When the flow separation is occurred in the impeller, the influence of the separation is restricted in the casing located at the impeller. But in the actual flow, the influence of separation of the impeller is spread wide to the circumferential location. In most cases, flow separation is responsible for lower performances and higher energy loss. Generally, the efficiency and loss calculations, however, revealed a significant discrepancy between the steady and unsteady simulation. Flow pattern in centrifugal fans are uneven having flow separation and recirculation zones in the flow passages. Hence, many researchers contributed to increasing the efficiency of the fan by novel approaches both numerically and experimentally. The discrepancy between the steady and unsteady simulation will be studied with the following contents.

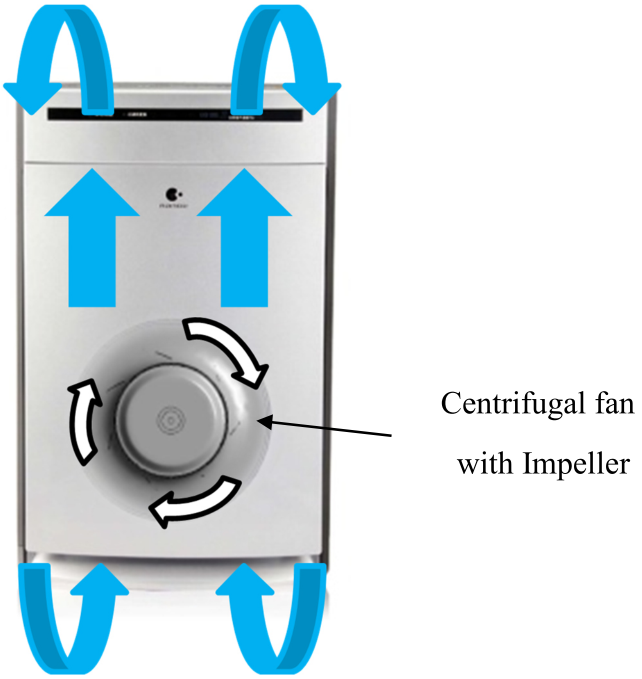

Fig. 1.1 Air cleaner

1.1 Research Background

The backward-curved centrifugal fan is obtained relatively high efficiency and low noise. The small size of this type of fan is used in the air conditioner and air cleaner. In the recent application, the fan is not used the scroll casing but the rectangular casing, because of the compact size and flexible design. The backward-curved centrifugal fans have been studied almost the case with the scroll casing [1], [4]. The flow characteristics are researched to improve the fan performance [1], [2], [4] that is mainly concerned to the interaction between the tongue and the impeller [3], [5]. The various geometries of the impeller and shroud are examined in the performance with experiments [6]. For the case of the air conditioner, there are studies in concerned to the interaction between the impeller and the heat exchanger [7], [9]. In the case, the air from the fan flows in all directions. The centrifugal fan uses the centrifugal force generated from the rotation of impellers to increase the pressure [11]. The air near the impeller is thrown-off from the impeller due to the centrifugal force and then moves into the fan casing [11]. The flow characteristics of the turbofan with a rectangular casing; the length of the rectangular casing does not influence the performance of the fan [8].

1.2 Objectives

The objectives of this research are intent as followings:

- to analyze flow characteristics of fan in relating to fan performance
- to improve performance of fan

The contents of this research are:

1. Aerodynamic and performances of fan with rectangular casing
2. Flow characteristics of fan with rectangular casing
3. Flow characteristics of fan with scroll casing
4. Flow characteristics of fan with changing blade outlet angle

The first purpose of this research is to make clear the influence of casing shapes, i.e., rectangular (RC) and scroll casing (SC), on flow characteristics and the energy loss in the impeller, the casings and fan. The flow characteristics and energy balance in the casing at each circumferential location are discussed. From simulation, analysis and comparison, the goal had been given that how the casing shapes was influences on the energy loss.

The second purpose is to understand the influence of unsteady behavior in the impeller, the casing and the fan on performance, internal flow patterns. And thus, it is discussed the responsibility for the above discrepancy, considering the physical aspects of the computations, steady Reynolds-averaged Navier-Stokes (RANS) and unsteady Reynolds-averaged Navier-Stokes (URANS). The third purpose is to compare the simulation results with respect to experimental results.

1.3 Scope of Thesis

There are five chapters in this thesis. Chapter 1 is about introduction, which is introduce about the centrifugal fan and its application, research background and objectives. Chapter 2 consists of theory background about Computational Fluid Dynamics (CFD). Chapter 3 describes about Experimental Apparatus and Measurements. Chapter 4 describes Investigation on Aerodynamic Performance of Centrifugal Fan under the influenced of Casing Geometries (Rectangular Casing and Scroll Casing). Chapter 5 describes Unsteady Flow Characteristics of Backward Impeller with Rectangular Casing. Chapter 6 describes Conclusion.

CHAPTER 2

COMPUTATIONAL FLUID DYNAMICS(CFD)

In this numerical study, the computational fluid dynamics (CFD) analysis code ANSYS-CFX 14.5 software was used to analysis the internal flow of centrifugal fan. Computational Fluid Dynamics (CFD) is a computer-based tool for simulating the behavior of systems involving fluid flow over a region of interest, with specified conditions on the boundary of the region. CFD is now an established industrial design tool, helping to reduce design time scales and improve processes throughout the engineering world. CFD provides a cost-effective and accurate alternative to scale model testing, with variations on the simulation being performed quickly, offering obvious advantages. CFD can be used to determine the performance of a component at the design stage, or it can be used to analyze difficulties with an existing component and lead to its improved design. This software can simulate a wide range of phenomena: aerodynamics, combustion, hydrodynamics, mixtures of liquids/solids/gas, particle dispersions, reacting flows, heat transfer, and much more. Steady-state and transient flow phenomena are easily and quickly solved.

2.1 Analysis Theory

ANSYS CFX is a high-performance computational fluid dynamics (CFD) software tool that delivers reliable and accurate solutions quickly and robustly across a wide range of CFD and multi-physics applications. CFX is recognized for its outstanding accuracy, robustness and speed with rotating machinery such as pumps, fans, compressors, gas and hydraulic turbines. It can solve wide-ranging fluid flow problems of all levels of complexity within the Workbench environment. It offers a comprehensive range of physical models that can be applied to a broad range of industries and applications, with extensive capabilities for customization and automation.

In this research, I had approach the centrifugal fan performance with the simulations by using ANSYS CFX 14.5. The predetermined performance was obtained from the simulations. The simulations were done both steady state and transient. The time dependence of the flow characteristics can be specified as either steady state or transient.

Steady state simulations are assumed that the flow characteristics do not change with time and have been reached after a relatively long-time interval. They therefore require no real-time information to describe them.

Transient simulations require real time information to determine the time intervals at which the CFX-Solver calculates the flow field. Transient behavior can be caused by the initially changing boundary conditions of the flow, as in startup, or it can be inherently related to the flow characteristics, so that a steady state condition is never reached, even when all other aspects of the flow conditions are unchanging.

Sometimes simulations that are run in steady state mode will have difficulty converging, and no matter what action taking mesh quality and time step size, the solution does not converge. This could be an indication of transient behavior.

For the setting of the Navier-Stokes equations, if the flow of a real fluid is non-linear, it is difficult to obtain an exact solution by solving analytically except a simple flow model. In simulations, CFD is used for obtaining a numerical approximation solution by using computer. There are a number of different solution methods that are used in CFD codes. The most common, and the one on which CFX is based, is known as the finite volume technique. In this technique, the region of interest is divided into small sub-regions, called control volumes. The equations are discretized and solved iteratively for each control volume. Thus, an approximation of the value of each variable at specific points throughout the domain can be obtained. In this way, one derives a full geometry of the behavior of the flow.

This software assisted to get predetermined performance of the centrifugal fan and if it is necessary, this step could do repeat. If this simulation step was over, the next steps could continue for manufacturing and modification of the impeller design. Therefore, this software assisted to complete the above steps during the short time.

2.2 Basic equation

2.2.1 Navier Stokes equation

The NavierStokes equations are the basic governing equations for a viscous fluid. It is a vector equation obtained by applying Newton's Law of Motion to a fluid element and is also called the momentum equation. It is supplemented by the mass conservation equation, also called continuity equation.

Governing equations of incompressible Navier-Stokes equations in conservation form are as following.

Continuity equation,

$$\frac{\partial \rho}{\partial t}+\frac{\partial U_j}{\partial x_j}=0 \tag{2.1}$$

Momentum equation,

$$\rho\frac{\partial U_i}{\partial t}+\rho\frac{\partial}{\partial x_j}\left(U_jU_i\right)=-\frac{\partial P}{\partial x_i}+\frac{\partial}{\partial x_j}2\mu S_{ij} \tag{2.2}$$

Where, the strain-rate tensor S_{ij} is given by,

$$S_{ij}=\frac{1}{2}\left(\frac{\partial U_i}{\partial x_j}+\frac{\partial U_j}{\partial x_i}\right) \tag{2.3}$$

The equation of motion of fluid is:

$$\rho\frac{\partial U_i}{\partial t}+\rho\frac{\partial}{\partial x_j}\left(U_jU_i\right)=-\frac{\partial P}{\partial x_i}+\mu\frac{\partial^2 U_i}{\partial x_j\partial x_j} \tag{2.4}$$

U is Velocity of fluid [m/s]

P is Fluid pressure [Pa]

ρ is Density of fluid [kg/m^3].

μ is Dynamic viscosity [Pa-s].

i, j is Direction of fluid flow.

2.2.2 Reynolds Averaged Navier–Stokes equations (RANS)

In general, turbulence models seek to modify the original unsteady Navier-Stokes equations by the introduction of time averaged and fluctuating quantities to produce the Reynolds Averaged Navier-Stokes (RANS) equations. These equations represent the mean flow quantities only, while modeling turbulence effects without a need for the resolution of the turbulent fluctuations. Turbulence models based on the RANS equations are known as Statistical Turbulence Models due to the statistical averaging procedure employed to obtain the equations.

The Reynolds averaged Navier–Stokes equations (or RANS equations) are time averaged equations of motion for fluid flow. The equations are Reynolds decomposition, whereby an instantaneous quantity is decomposed into its time averaged and fluctuating quantities. The RANS equations are used to describe turbulent flows. This equation can be used with approximations of the properties of flow turbulence to give approximate time averaged solutions to the Navier–Stokes equations.

The basic tool required for the derivation of the RANS equations from the instantaneous Navier–Stokes equations is the Reynolds decomposition. Reynolds decomposition refers to separation of the flow variable (velocity, U) into the mean (time averaged) component ($\overline{U}$) and the fluctuating component (u). The mean operator ($-$) is a Reynolds operator, it has a set of properties. One of these properties is that the mean of the fluctuating quantity being equal to zero($\bar{u}$=0) Thus, the equation is:

$$U(\boldsymbol{i}, t) = \overline{U}(\boldsymbol{i}) + u(\boldsymbol{i}, t) \tag{2.5}$$

Where, $\boldsymbol{i}$ is the position vector (i, j, k) .

u is Velocity fluctuating term.

U is Instantaneous velocity [m/s].

$\overline{U}$ is Mean velocity [m/s].

The properties of Reynolds operators are useful in the derivation of the RANS equations. By using these properties, the Navier–Stokes equations of motion, expressed in equation (2.4) with tensor notation, then next, each instantaneous quantity can be split into time averaged and fluctuating components, and the resulting equation with time-average are as following.

Continuity equation (2.1) becomes,

$$\frac{\partial \overline{U}_j}{\partial x_j} = 0 \tag{2.6}$$

Momentum equation (2.4) becomes,

$$\rho\frac{\partial \bar{U}_i}{\partial t} + \rho\bar{U}_j\frac{\partial \bar{U}_i}{\partial x_j} + \rho\bar{u}_j\frac{\partial \bar{u}_i}{\partial x_j} = -\frac{\partial \bar{P}_i}{\partial x_i} + \mu\frac{\partial^2 \bar{U}_i}{\partial x_j \partial x_j} + S_M \tag{2.7}$$

$$\rho\frac{\partial \bar{U}_i}{\partial t} + \rho\bar{U}_j\frac{\partial \bar{U}_i}{\partial x_j} = -\frac{\partial \bar{P}_i}{\partial x_i} + \mu\frac{\partial^2 \bar{U}_i}{\partial x_j \partial x_j} - \rho\frac{\partial \overline{u_i u_j}}{\partial x_j} + S_M \tag{2.8}$$

Finally, the resulting equation (2.8) consists an integration in time term, and thus equation (2.8) is **URANS** (Unsteady Reynolds Averaged Navier-Stokes equations).

At **URANS**, the variables are defined as: $\bar{U} = \hat{U}\,(t) + U'(t)$

Where, $\hat{U}\,(t)$ is the velocity in unsteady flow phenomena of large timescale.

$U'(t)$ is the velocity in the turbulent.

The time derivative must be eliminated from equation (2.8) to get **RANS** equation. By removing the time dependence of the resultant terms, the **RANS** equation is in equation (2.9).

$$\rho\bar{U}_j\frac{\partial \bar{U}_i}{\partial x_j} = -\frac{\partial \bar{P}_i}{\partial x_i} + \frac{\partial}{\partial x_j}\left[2\mu\bar{S}_{ij} - \rho\overline{u_i u_j}\right] + S_M \tag{2.9}$$

Where, $\bar{S}_{ij} = \frac{1}{2}\left(\frac{\partial \bar{U}_i}{\partial x_j} + \frac{\partial \bar{U}_j}{\partial x_i}\right)$ is the mean rate of strain tensor.

$-\rho\overline{u_i u_j}$ is Reynolds stresses tensor.

S_M is the sum of body forces.

2.3 Turbulence Model in ANSYS-CFX

There are different methods for the treatment of turbulent flows. The need for a model results from the inability of CFX-CFD simulations to fully resolve all time and length scales of a turbulent motion. In classical CFX-CFD methods, the Navier-Stokes equations are usually time or ensemble-averaged, reducing the resolution requirements by many orders of magnitude. The resulting equations are the RANS equations.

Simulation of the RANS equations greatly reduces the computational effort compared to a *Direct Numerical Simulation* and is generally adopted for practical engineering calculations. However, the averaging procedure introduces additional unknown terms containing products of the fluctuating quantities, which act like ***additional stresses*** in the fluid. These terms, called ***'turbulent'*** or ***'Reynolds stresses'***, are difficult to determine directly and so become further unknowns.

The Reynolds (turbulent) stresses in right side of equation (2.8) or (2.9) need to be modeled by additional equations of known quantities in order to achieve "closure." Closure implies that there is a sufficient number of equations for all the unknowns, including the

Reynolds-Stress tensor resulting from the averaging procedure. The equations used to close the system define the type of turbulence model. In what follows, I describe several approaches (***Two equation turbulence models***) for solving the RANS equations.

2.3.1 Two Equation Turbulence Models

Two-equation turbulence models are very widely used, as they offer a good compromise between numerical effort and computational accuracy. Both the velocity and length scale of turbulent are solved using separate transport equations (hence the term ‘two-equation’).

The ***k-ε*** and ***k- ω***, two-equation models use the gradient diffusion hypothesis to relate the Reynolds stresses to the mean velocity gradients and the turbulent viscosity. The turbulent viscosity is modeled as the product of a turbulent velocity and turbulent length scale.

In two-equation models, the turbulence velocity scale is computed from the turbulent kinetic energy, which is provided from the solution of its transport equation. The turbulent length scale is estimated from two properties of the turbulence field, usually the turbulent kinetic energy and its dissipation rate. The dissipation rate of the turbulent kinetic energy is provided from the solution of its transport equation.

2.3.1.1 The *k-ε* Model in ANSYS CFX

k is the turbulence kinetic energy and is defined as the variance of the fluctuations in velocity.ε is the turbulence eddy dissipation (the rate at which the velocity fluctuations dissipate).

The k-ε model introduces two new variables into the system of equations. By using equations (2.3), (2.4). the momentum equation becomes,

$$\rho\frac{\partial U_i}{\partial t}+\rho\frac{\partial}{\partial x_j}\left(U_jU_i\right)=-\frac{\partial P'}{\partial x_i}+\frac{\partial}{\partial x_j}\left[\mu_{eff}\left\{\frac{\partial U_i}{\partial x_j}+\frac{\partial U_j}{\partial x_i}\right\}\right]+S_M \tag{2.10}$$

Where,

$\mu_{eff}=\mu+\mu_t$ is the effective viscosity accounting for turbulence.

$P'=P+\frac{2}{3}\rho k+\frac{2}{3}\mu_{eff}\frac{\partial U_k}{\partial x_k}$ is the modified pressure. The last term involves the divergence of velocity. It is neglected in ANSYS CFX, although this assumption is strictly correct only for incompressible fluids.

S_M is the sum of body forces.

The values of k and ε come directly from the differential transport equations for the turbulence kinetic energy and turbulence dissipation rate.

Turbulence kinetic energy, k model expression is in equation (2.11).

$$\frac{\partial(\rho k)}{\partial t}+\frac{\partial}{\partial x_j}\left(\rho U_j k\right)=\frac{\partial}{\partial x_j}\left[\left(\mu+\frac{\mu_t}{\sigma_k}\right)\frac{\partial k}{\partial x_j}\right]+P_k-\rho\varepsilon+P_{kb} \tag{2.11}$$

Turbulence dissipation rate, ε model expression is in equation (2.12).

$$\frac{\partial(\rho\varepsilon)}{\partial t}+\frac{\partial}{\partial x_j}(\rho U_j\varepsilon)=\frac{\partial}{\partial x_j}\left[\left(\mu+\frac{\mu_t}{\sigma_s}\right)\frac{\partial\varepsilon}{\partial x_j}\right]+\frac{\varepsilon}{k}(C_{\varepsilon 1}P_k-C_{\varepsilon 2}\rho\varepsilon+C_{\varepsilon 1}P_{\varepsilon b}) \tag{2.12}$$

Where,

The turbulence viscosity is linked to the turbulence kinetic energy and dissipation with the relation $\mu_t = C_\mu\, \rho \frac{k^2}{\varepsilon}$.

$C_\mu, C_{\varepsilon 1}, C_{\varepsilon 2}, and\ \sigma_\varepsilon$ is *k-ε* turbulence model constant and σ_k is *k* turbulence model constant in the equation (2.11) and (2.12). The values are usually in the following.

$C_\mu = 0.09,\ C_{\varepsilon 1} = 1.44,\ C_{\varepsilon 2} = 1.92, \sigma_k = 1.0$ and $\sigma_\varepsilon = 1.3$

P_{kb} and $P_{\varepsilon b}$ represent the influence of the buoyancy forces. P_k is the turbulence production due to viscous forces.

$$P_k=\mu_t\left(\frac{\partial U_i}{\partial x_j}+\frac{\partial U_j}{\partial x_i}\right)\frac{\partial U_i}{\partial x_j}-\frac{2}{3}\frac{\partial U_k}{\partial x_k}\left(3\mu_t\frac{\partial U_k}{\partial x_k}+\rho k\right) \tag{2.13}$$

For incompressible flow, $\frac{\partial U_k}{\partial x_k}$ is small and the second term on the right side of equation does not contribute significantly to the production.

2.3.1.2 The *k-ω* Model in ANSYS-CFX

One of the advantages of the *k-ω* formulation model is the near wall treatment for low-Reynolds number computations. The model does not involve the complex nonlinear damping functions required for the model and is therefore more accurate and more robust. A low-Reynolds *k-ε* model would typically require a near wall resolution of $y^+ < 0.2$, while a low-Reynolds number *k-ω* model would require at least $y^+ < 2$. In industrial flows, even $y^+ < 2$ cannot be guaranteed in most applications and for this reason, a new near wall treatment was developed for the *k-ω* models. It allows for smooth shift from a low-Reynolds number form to a wall function formulation.

The *k-ω* model developed by **Wilcox** solves two transport equations, one for the turbulent kinetic energy, and one for the turbulent frequency. The stress tensor $-\rho\overline{u_i u_j}$ in equation (2.9) is computed from the eddy-viscosity concept.

Turbulent kinetic energy, *k*-equation:

$$\frac{\partial(\rho k)}{\partial t}+\frac{\partial}{\partial x_j}(\rho U_j k)=\frac{\partial}{\partial x_j}\left[\left(\mu+\frac{\mu_t}{\sigma_k}\right)\frac{\partial k}{\partial x_j}\right]+P_k-\beta'\rho k\omega+P_{kb} \tag{2.14}$$

Turbulent frequency, *ω*-equation:

$$\frac{\partial(\rho\omega)}{\partial t}+\frac{\partial}{\partial x_j}(\rho U_j\omega)=\frac{\partial}{\partial x_j}\left[\left(\mu+\frac{\mu_t}{\sigma_\omega}\right)\frac{\partial\omega}{\partial x_j}\right]+\alpha\frac{\omega}{k}P_k-\beta\rho\omega^2+P_{\omega b} \tag{2.15}$$

Where,

$\mu_t = \rho\frac{k}{\omega}$ is the turbulence viscosity.

β', α, β, σ_k and σ_ω are model constant. The values are as following.

$\beta' = 0.09, \alpha = 5/9, \beta = 0.075, \sigma_k = 2, \sigma_\omega=2$

The unknown Reynolds stress tensor, $-\rho\overline{u_i u_j}$, is calculated in the following.

$$-\rho\overline{u_i u_j} = \mu_t\left(\frac{\partial U_i}{\partial x_i} + \frac{\partial U_j}{\partial x_i}\right) - \frac{2}{3}\delta_{ij}\left(\rho k + \mu_t\frac{\partial U_k}{\partial x_k}\right) \tag{2.16}$$

2.3.1.3 The Baseline (BSL) k- ω Model

The main problem of the **Wilcox model** in equation (2.13) and (2.14) is its well known strong sensitivity to freestream conditions. Depending on the value specified for *ω* at the inlet, a significant variation in the results of the model can be obtained. This is undesirable and in order to solve the problem, a blending between the *k-ω* model near the surface and the *k- ε* model in the outer region was developed.

It consists of a transformation of the *k-ε* model to a *k -ω* formulation and a subsequent addition of the corresponding equations. The transform of *k-ε* model shown in equation (2.11) and (2.12) is written as following.

Transformed ***k-ε*** model:

$$\frac{\partial(\rho k)}{\partial t} + \frac{\partial}{\partial x_j}(\rho U_j k) = \frac{\partial}{\partial x_j}\left[\left(\mu + \frac{\mu_t}{\sigma_{k1}}\right)\frac{\partial k}{\partial x_j}\right] + P_k - \beta'\rho k\omega \tag{2.17}$$

$$\frac{\partial(\rho\omega)}{\partial t} + \frac{\partial}{\partial x_j}(\rho U_j\omega) = \frac{\partial}{\partial x_j}\left[\left(\mu + \frac{\mu_t}{\sigma_{\omega1}}\right)\frac{\partial\omega}{\partial x_j}\right] + 2\rho\frac{1}{\sigma_{\omega1}\omega}\frac{\partial k}{\partial x_j}\frac{\partial\omega}{\partial x_j} + \alpha_1\frac{\omega}{k}P_k - \beta_1\rho\omega^2 \tag{2.18}$$

Now, the equations of the Wilcox model in equation (2.13) is multiplied by function *F₁*, the transformed *k- ε* model in equation (2.16) by a function *1-F₁* and the corresponding *k-* and ω- equations are added to give the BSL model in equation (2.17) and (2.18)

$$\frac{\partial(\rho k)}{\partial t} + \frac{\partial}{\partial x_j}(\rho U_j k) = \frac{\partial}{\partial x_j}\left[\left(\mu + \frac{\mu_t}{\sigma_{k2}}\right)\frac{\partial k}{\partial x_j}\right] + P_k - \beta'\rho k\omega + P_{kb} \tag{2.19}$$

$$\frac{\partial(\rho\omega)}{\partial t} + \frac{\partial}{\partial x_j}(\rho U_j\omega) = \frac{\partial}{\partial x_j}\left[\left(\mu + \frac{\mu_t}{\sigma_{\omega2}}\right)\frac{\partial\omega}{\partial x_j}\right] + (1 - F_1)2\rho\frac{1}{\sigma_{\omega1}\omega}\frac{\partial k}{\partial x_j}\frac{\partial\omega}{\partial x_j}$$
$$+\alpha_2\frac{\omega}{k}P_k - \beta_2\rho\omega^2 + P_{\omega b} \tag{2.20}$$

Where, $\beta' = 0.09$, F_1=0, F_1 is equal to one near the surface and decreases to a value of zero outside the boundary layer (that is, a function of the wall distance).

$\alpha_1 = 0.44, \beta_1 = 0.0828$

$\sigma_{k1} = 2, \sigma_{k1} = 1$

σ_{ω}=2, $\sigma_{\omega 1}$=1/0.856

$\beta_2 = F_1\beta + (1 - F_1)\beta_1$

The coefficients of the new model, $\sigma_{k2,}\sigma_{\omega 2,}\beta_{2,}\alpha_2$are a linear combination of the corresponding coefficients of this model.

2.3.1.4. The Shear Stress Transport (SST)

The *k-ω* based SST model is shown in equation (2.21). This model gives highly accurate predictions of the onset and the amount of flow separation under adverse pressure gradients.

The shear stress transport (SST) model behavior can be obtained by substituting the formulation of the eddy-viscosity (μ_t) in equation (2.19) and equation (2.20).

The eddy-viscosity is

$$\nu_t = \frac{\alpha_1 k}{\max(\alpha_1\,\omega, SF_2)} \text{ and } \nu_t = \mu_t/\rho \tag{2.21}$$

Where,

F₂ is blending function.

S is an invariant measure of the strain rate.

Finally, the equation of the *k-ω* based SST model is the following.

$$\frac{\partial(\rho k)}{\partial t} + \frac{\partial}{\partial x_j}(\rho U_j k) = \frac{\partial}{\partial x_j}\left[\left(\mu + \frac{\rho\nu_t}{\sigma_{k2}}\right)\frac{\partial k}{\partial x_j}\right] + P_k - \beta'\rho k\omega + P_{kb} \tag{2.22}$$

$$\frac{\partial(\rho\omega)}{\partial t} + \frac{\partial}{\partial x_j}(\rho U_j\omega) = \frac{\partial}{\partial x_j}\left[\left(\mu + \frac{\rho\nu_t}{\sigma_{\omega 2}}\right)\frac{\partial\omega}{\partial x_j}\right] + (1 - F_1)2\rho\frac{1}{\sigma_{\omega 1}\omega}\frac{\partial k}{\partial x_j}\frac{\partial\omega}{\partial x_j}$$

$$+\alpha_2\frac{\omega}{k}P_k - \beta_2\rho\omega^2 + P_{\omega b} \tag{2.23}$$

2.4 Discretization of the Governing Equations

ANSYS CFX uses an element-based finite volume method, which first involves discretizing the spatial domain using a mesh. The mesh is used to construct finite volumes, which are used to conserve relevant quantities such as mass, momentum, and energy. The mesh is three dimensional, but for simplicity an illustrate this process is two dimensions.

Figure 2.1 shows a control volume with typical two-dimensional mesh. All solution variables and fluid properties are stored at the nodes (mesh vertices). A control volume (the shaded area) is constructed around each mesh node using the median dual (defined by lines joining the centers of the edges and element centers surrounding the node).

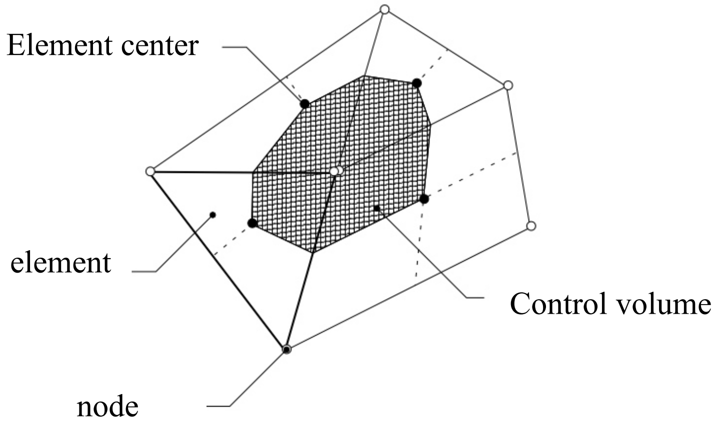

Fig. 2.1 A typical two-dimensional mesh (Ref. ANSYS 14.5 help)

To illustrate the finite volume methodology, consider the conservation equations for mass, and momentum expressed in equation (2.1), (2.2) and (2.3). These equations are integrated over each control volume, and Gauss' Divergence Theorem applied to convert volume integrals involving divergence and gradient operators to surface integrals. If control volumes do not deform in time, then the time derivatives can be moved outside of the volume integrals and the integrated equations become:

$$\frac{d}{dt}\int_V \rho dV + \int_S \rho U_j \, dn_j = 0 \tag{2.24}$$

$$\frac{d}{dt}\int_V \rho U_i dV + \int_S \rho U_i \, U_j dn_j = -\int_S P dn_j + \int_S \mu_{eff}\left(\frac{\partial U_i}{\partial x_j} + \frac{\partial U_j}{\partial x_i}\right) dn_j + \int_V S_{U_i} \, dV \tag{2.25}$$

Where, *V* and *S* are volume and surface regions of integration, and *dn*$_j$ are the differential cartesian components of the outward normal surface vector. The volume integrals represent source or accumulation terms, and the surface integrals represent the summation of the fluxes.

The next step in the numerical algorithm is to discretize the volume and surface integrals. To illustrate this step, consider a single element shown in Fig. 2.2.

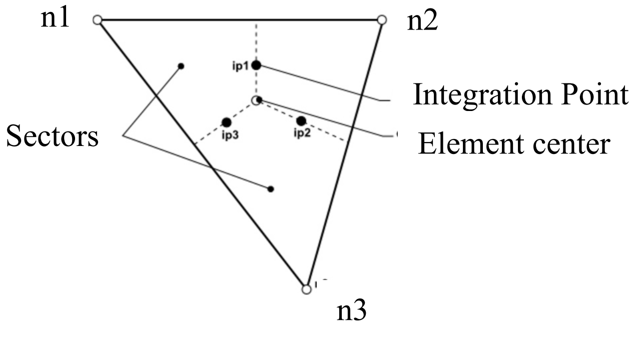

Fig. 2.2 Mesh Element (Ref. ANSYS 14.5 help)

Volume integrals are discretized within each element sector and accumulated to the control volume to which the sector belongs. Surface integrals are discretized at the integration points (*ipn*) located at the centre of each surface segment within an element and then distributed to the adjacent control volumes. Because the surface integrals are equal and opposite for control volumes adjacent to the integration points, the surface integrals are guaranteed to be locally conservative.

After discretizing the volume and surface integrals, the integral equations (2.24) and (2.25) become into equation (2.26) and (2.27). The following equations are discretization of the governing equations. These equations are assumed for the *First Order Backward Euler scheme in solver control.*

$$V\left(\frac{\rho-\rho^0}{\Delta t}\right)+\sum_{ip}\dot{m}_{ip}=0 \tag{2.26}$$

$$V\left(\frac{\rho U_i-\rho^0U_i^0}{\Delta t}\right)+\sum_{ip}\dot{m}_{ip}\,(U_i)_{ip}=\sum_{ip}(P\Delta n_i)_{ip}+$$

$$\sum_{ip}\left[\mu_{eff}\left(\frac{\partial U_i}{\partial x_j}+\frac{\partial U_j}{\partial x_i}\right)\Delta n_j\right]_{ip}+\overline{S_{U_i}V} \tag{2.27}$$

Where, $\dot{m}_{ip}=\left(\rho U_j\Delta n_j\right)_{ip}$, V is the control volume, Δt is the time step, Δn_j is the discrete outward surface vector, the subscript ip denotes evaluation at an integration point, summations are over all the integration points of the control volume, and the superscript ^{0} refers to the old-time level.

2.5 Transient Scheme in CFX-Pre

The transient scheme defines the discretization algorithm for the transient term which is First Order Backward Euler and Second Order Backward Euler. In CFX-Pre, the transient term was set for solver control. In this calculation, First Order Backward Euler was set for steady state calculation and Second Order Backward Euler was set for unsteady state calculation in implicit above method.

2.5.1 First Order Backward Euler

The First Order Backward Euler scheme is an implicit time-stepping scheme that is first-order accurate. With the First Order, Backward Euler scheme, the start and end of time step values are respectively approximated using the old and current time level solution values. The general discrete approximation of the transient term for the nth timestep is as following.

$$\frac{d}{dt}\int_V \rho\varphi dV \approx V\,\frac{(\rho\varphi)^{n+\frac{1}{2}}-(\rho\varphi)^{n-\frac{1}{2}}}{\Delta t} \tag{2.28}$$

Where values at the start and end of the timestep are assigned the superscripts n+½ and n-½, respectively.

The volume integration term in the left side of the equation (2.24) becomes the equation (2.29) by using the equation (2.28). The resulting discretization is in the following equation (2.27). Here, the superscript ^{0} indicates the previous iterates.

$$\frac{d}{dt}\int_V \rho\varphi dV = V\left(\frac{\rho\varphi - \rho^0\varphi^0}{\Delta t}\right) \tag{2.29}$$

2.5.2 Second Order Backward Euler

The Second Order Backward Euler scheme is also an implicit time-stepping scheme, but is second-order accurate, and is the default in ANSYS-CFX. It is applicable for constant and variable timestep sizes. When running the Second Order Backward Euler scheme, the transient scheme for turbulence equations will remain First Order, and the transient scheme for volume fraction equations set to a bounded second-order scheme. This scheme is generally used for most transient RANS.

With the Second Order Backward Euler scheme, the start and end of time step values are respectively approximated as:

$$(\rho\varphi)^{n-\frac{1}{2}} = (\rho\varphi)^0 + \frac{1}{2}((\rho\varphi)^0 - (\rho\varphi)^{00}) \tag{2.30}$$

$$(\rho\varphi)^{n+\frac{1}{2}} = (\rho\varphi) + \frac{1}{2}\left((\rho\varphi) - (\rho\varphi)^0\right) \tag{2.31}$$

When these values are substituted into the general discreet approximation, equation (2.28), the resulting discretization is:

$$\frac{d}{dt}\int_V \rho\varphi dV \approx V\,\frac{1}{\Delta t}\left(\frac{3}{2}(\rho\varphi) - 2(\rho\varphi)^0 + \frac{1}{2}\,(\rho\varphi)^{00}\right) \tag{2.32}$$

2.6 Setup Procedure for Simulations

In this simulation, ANSYS-CFX 14.5 used an element based finite volume method, which first involves discretizing the spatial domain using a mesh. The mesh is used to construct finite volumes, which are used to conserve relevant quantities such as mass, momentum, and energy.

In this research, the CFD-CFX simulation process performed in four components:

1. Creating the Geometry and Mesh
2. Defining the Physics of the Model
3. Solving the CFD Problem
4. Visualizing the Results in the Post-processor

1. Creating the Geometry and Mesh in Workbench

This interactive process is the first pre-processing stage. The objective is to produce a mesh for input to the physics pre-processor. Before a mesh can be produced, the geometry of centrifugal fan was created in ANSYS-CFX 14.5 workbench. The mesh was created in the Meshing application. The basic steps involve:

a. Defining the geometry of centrifugal fan.

b. Creating domains of fluid flow, solid domains and surface boundary names.

c. Setting properties for the mesh.

In case of meshing, it is a step of installation of the calculation lattice points and create a mesh to create a computational grid points according to the shape of centrifugal fan created by Geometry. The volume and surface was analyzed in detail for generating fine mesh. The mesh calculation time was changed depending on the element size.

2. Defining the Physics of the Model in CFX-Pre

This interactive process is the second pre-processing stage and is used to create input required by the Solver. The mesh files are loaded into the physics pre-processor. The physical model in case of centrifugal fan that are to be included in the simulation are selected. Fluid properties and boundary conditions are specified in the domain. Flow analysis types were selected in this stage.

3. Solving the CFD Problem by CFX Solver Manger

The component that solves the CFD problem is called the Solver. It produces the required results in a non-interactive/batch process. A CFD problem is solved as follows:

a. The partial differential equations are integrated over all the control volumes in the region of interest. This is equivalent to applying a basic conservation law (for example, for mass or momentum) to each control volume.

b. These integral equations are converted to a system of algebraic equations by generating a set of approximations for the terms in the integral equations.

c. The algebraic equations are solved iteratively. An iterative approach is required because of the nonlinear nature of the equations, and as the solution approaches the exact solution, it is said to converge. For each iteration, the errors, or residuals, are reported as a measure of the overall conservation of the flow properties.

How close the final solution is to the exact solution depends on a number of factors, including the size and shape of the control volumes and the size of the final residuals. Complex physical processes, such as combustion and turbulence, are often modeled using empirical relationships. The solution process requires no user interaction and is, therefore, usually carried out as a batch process. The solver produces a results file that is then passed to the post-processor.

4. Visualizing the Results in the Post-processor

The post-processor is the component used to analyze, visualize and present the results interactively. Post-processing includes anything from obtaining point values to complex animated sequences.

Examples of some important features of post-processors are:

a. Visualization of the geometry and control volumes

b. Vector plots showing the direction and magnitude of the flow

c. Visualization of the variation of scalar variables (variables that have only magnitude, not direction, such as temperature, pressure and speed) through the domain

2.7 Calculations of Centrifugal Fans with difference Casings

2.7.1 Geometry of the backward Impeller and casings

The geometry of the computational models used in the numerical simulation analysis show in Fig. 2.3 (a) and (b). The computational model with rectangular casing (RC) shows in Fig. 2.3 (a). The computational model with scroll casing (SC) shows in Fig. 2.3 (b). The computational model was created in CFX-Geometry. The casings were set to be the same dimensions as that used in the experiments. In experiment, the flow comes from the auxiliary fan and its perpendicularly enter the impeller inlet and then it was discharged passing through the casing to the atmosphere. In the numerical simulation, the computational domains were created to calculate the fluid flow analysis. It is not possible to completely reproduce the actual same flow. Therefore, the inlet part of the impeller geometry was assumed hemispherical shaped and the flow perpendicularly entered the impeller. In casing geometry, the extended length of casing outlet was assumed twice of casing length. It was possible that the fluid flow was to be closer in the actual flow and to become stabilized flow by the extended region.

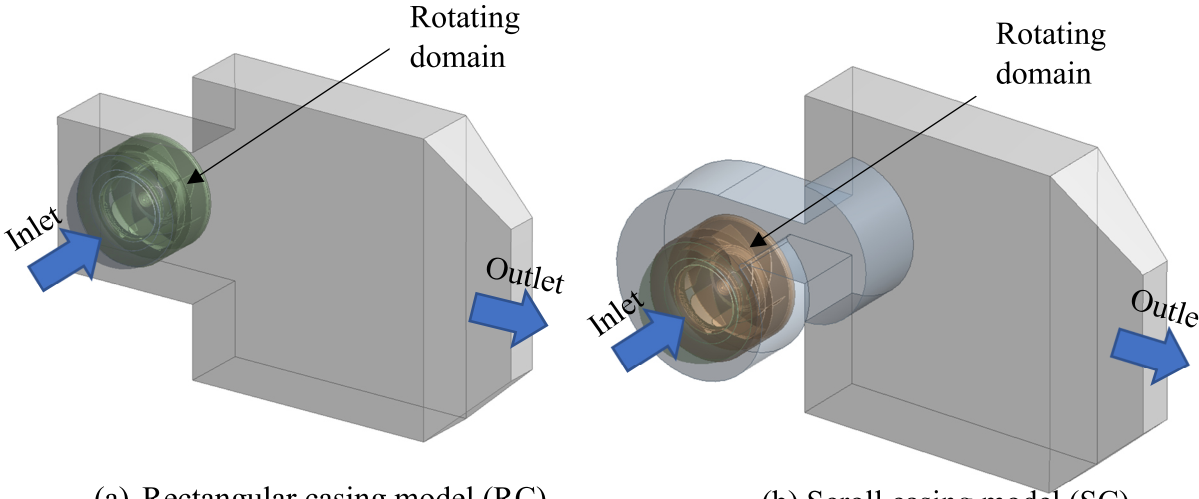

(a) Rectangular casing model (RC) (b) Scroll casing model (SC)

Fig. 2.3 Computational model

There were three computational domains in this model. They were the inlet, rotating domain and the outlet domains. The inlet domain was hemispherical shaped. The inlet domain consisted an interface in which the fluid was passing through in inlet domain to the rotating domain. The rotating domain consisted the impeller geometry and two interfaces in which one was for entering the fluid from the inlet domain to the rotating domain. Another was for outflow of fluid from the rotating domain to the casing. The outlet domain consisted the casing geometry and an interface. The interface was for entering the fluid form the rotating domain to the casing located in the outlet domain.

The impeller model geometry was separately created in CFX-Geometry. The backward impeller showed in Fig. 2.3 (c). It was imported in the computational model by the cut material. The rotating domain created by slice material which divided computational domain into the inlet domain, rotating domain and outlet domain. The geometries of the reference impeller are listed in Table 2.1.

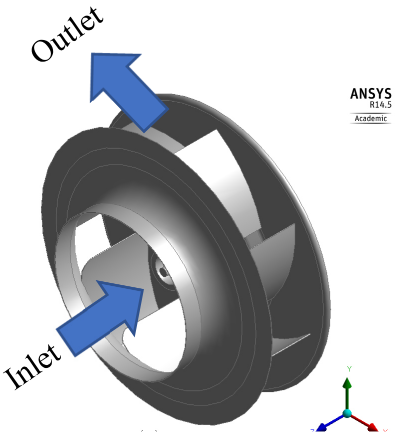

Fig. 2.3 (c) Impeller geometry

Table 2.1 Geometry of reference impeller

Lists		Dimensions
Inlet diameter	D_1	142 mm
Outlet diameter	D_2	230 mm
Exit blade height	H	60.5 mm
Number of blades	B	7
Blade thickness	t	1 mm
Inlet angle	β_{1d}	15°
Outlet angle	β_{2d}	35°
Rotational speed		1100 rpm

The half side views of RC and SC casings are shown in Fig. 2.4. Each casing dimensions show in Fig. 2.4 (a) and (b).

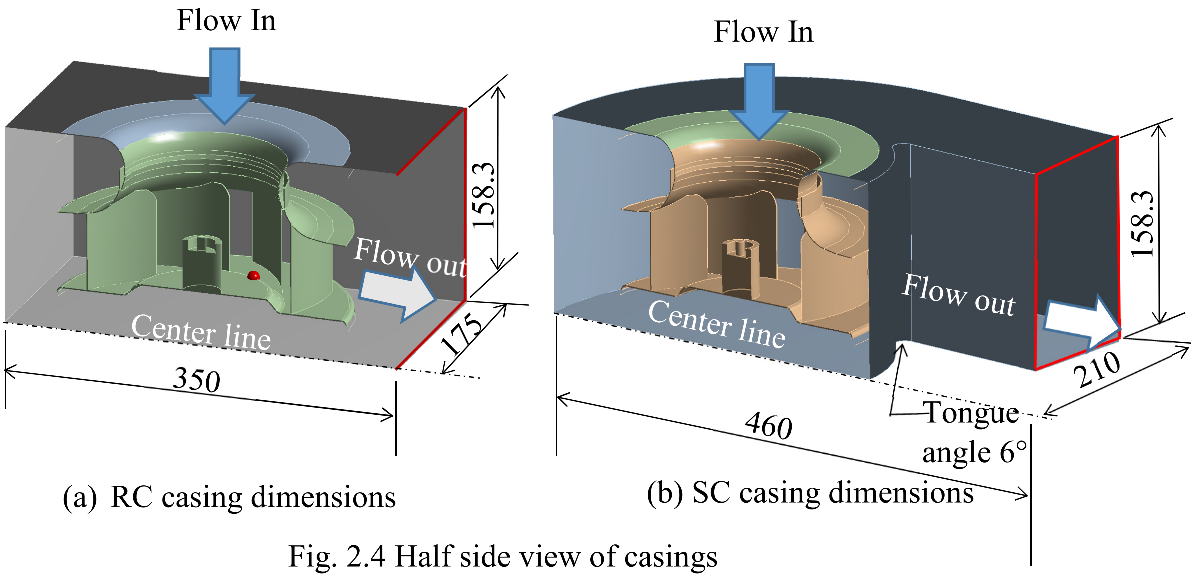

(a) RC casing dimensions

(b) SC casing dimensions

Fig. 2.4 Half side view of casings

2.7.2 Mesh creations

The mesh in computational domain is shown in Fig. 2.5 (a) and (b). The mesh in computational RC casing model show in Fig. 2.5 (a) and SC casing model shows in Fig. 2.5 (b).

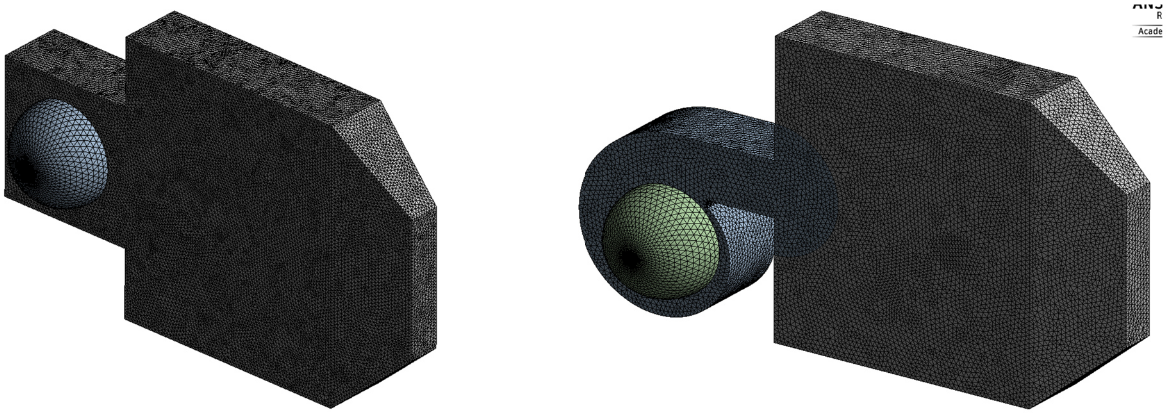
(a) RC casing model

(b) SC casing model

Fig. 2.5 Mesh in computational models

The elements and nodes of each computational domain list in Table 2.2. Elements and node numbers in each domain is listed in this table.

Table 2.2 Elements and nodes of each computational domain

Mesh	Names on casings					
	RC casing domains			SC casing domains		
	Inlet	Rotating	Outlet	Inlet	Rotating	Outlet
Elements	48407	2258272	1588486	48441	3005545	845414
Nodes	9330	567415	281500	9344	717470	153707

In real fluid, in case of the air, the viscous force is very smaller in high Reynolds number than the inertia force, since no slip condition on the blade surface and the velocity on the surface region is zero. The viscous of airflow reduces the local velocities on a surface and is responsible for wall friction. The layer of air over the blade surface named boundary layer that is slowed down or stopped by viscosity at the leading edge of blade.

The thickness of the velocity boundary layer is normally defined as the distance from the solid body at which the viscous flow velocity is 99% of the freestream velocity. The no-slip condition requires the flow velocity at the surface of a solid object be zero and the fluid temperature be equal to the temperature of the surface. The flow velocity will then increase rapidly within the boundary layer.

In CFX, one of the most essential issues for the optimal performance of turbulence models is the proper resolution of the boundary layer. In this section, two criteria for judging the quality of a mesh are minimum spacing between nodes in the boundary layer and minimum number of nodes in the boundary layer. These are simple guidelines for the generation of meshes which satisfy the minimal requirements for accurate boundary layer computations. The goal is to determine the required near wall mesh spacing, Δy, in terms of Reynolds number, running length (in case of blade chord length), and Δy^+ target value.

The estimation of Reynolds number is:

$$Re = \frac{\rho U L}{\mu} \tag{2.33}$$

Reynold number (*Re*) is considered for the blade which is calculated by the equation (2.31). The chord length of blade is 0.08643 m, the tangential velocity at the impeller exit is 15.38 m/s (calculated from the formula $U = R \times \omega$), the air density (ρ) and dynamic viscosity (μ) at temperature 25.9°C is 1.177 kg/m^3 and $1.846\ \times 10^{-5}$kg/ms, the value of *Re* is $8.47\times\ 10^{-7}$ by equation (2.34).

For the determination of the near wall spacing (minimum grid width on the blade), the approximation formulas of wall (skin) friction coefficient for turbulent boundary layer, C_f is defined by Hermann Schlichting. For $\mathrm{Re} < 10^9$, C_f is calculated with equation (2.34).

$$\mathrm{C}_f = (2.0 log_{10} Re - 0.65)^{-2.3} \tag{2.34}$$

The value of C_f is 0.0061, then the wall shear stress acting on the blade surface, τ_ω[Pa] is calculated with equation (2.35).

$$\tau_\omega = C_f \frac{\rho U^2}{2} \tag{2.35}$$

Then, the value of $\tau_\omega$is 0.848m/s by using C_f=0.0061. Friction velocity, u_τ can calculate with equation (2.36).

$$u_\tau = \sqrt{\frac{\tau_\omega}{\rho}} \tag{2.36}$$

The value of friction velocity, u_τ is 0.846 m/s. The initial thickness of boundary layer on the blade (minimum grid width on the blade or wall mesh spacing), Δy[m] can calculate with equation (2.37).

$$\Delta y = \frac{\Delta y^+ \nu}{u_\tau} \tag{2.37}$$

In which, kinematic viscosity, $\nu = 1.568 \times 10^{-5} [m^2/s]$, Δy^+ is non-dimensional quantity of Δy, set Δy^+=5, finally the value Δy is 0.93×10^{-4}[m]. Thus, in CFX, for the mesh inflection, the minimum layer thickness set 0.1 mm and number of layers set 10 layers. The mesh in the rotating domain shows in Fig. 2.6. The mesh of blades is inflection as shown in Fig. 2.6 (a). The total number of mesh for all domains is about 5 million with tetra mesh. The minimum edge length of tetra mesh is 0.8 mm. The mesh in rotating impeller domain is shown in Fig. 2.6 (b).

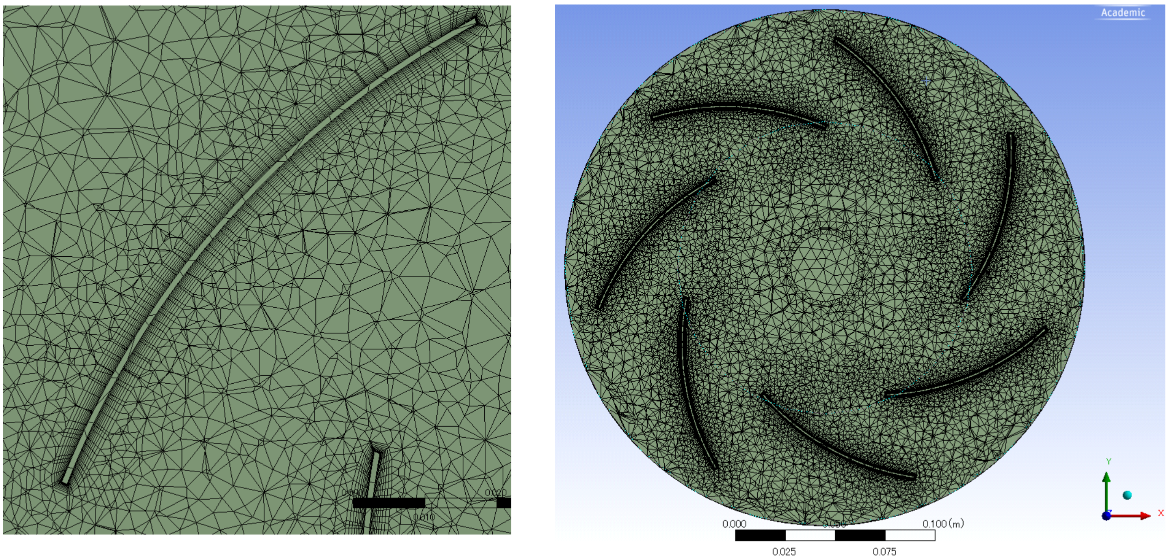

(a) Detail around blade mesh (Inflection) (b) Impeller domain

Fig 2.6 Mesh in rotating domain

2.7.3 Setup boundary conditions

The flow field of the centrifugal fan with casing was simulated with the commercial code ANSYS CFX 14.5. In CFX-Pre, the boundary conditions set for steady state calculations of the centrifugal fan with difference casings. The steady flow was simulated with RANS to analyse the flow characteristics of fan. The computational models are shear stress transport (SST) turbulence model with automatic wall function. The computational domains set up the inlet, the rotating and the outlet. All the domains set the fluid domains and the working fluid was an ideal gas (air at 25°C). The reference pressure set the same with the atmospheric pressure, 1 atm. The inlet and outlet domain set stationary. The rotor domain set the rotating domain which was rotated with 1100 rpm clockwise direction. The static pressure set 0 Pa at the inlet domain and the mass flow rate set in the outlet domain. The boundary plane between the impeller and casing regions is imposed by Frozen-Rotor interface. The solid surfaces in the computational domain are no-slip wall and smooth wall conditions.

In this study, the steady state calculations were done with the five mass flow rates. They are the flow coefficients of $\phi = 0.014, \phi = 0.121, \phi = 0.187, \phi = 0.237,$ and $\phi = 0.26$. Where, $\phi = 0.187$ was design flow coefficient. In the steady state calculation, the flow characteristics do not change with time and thus timescale control set Auto Timescale. Auto Timescale is the default timescale control setting. However, it is aware that the Auto Timescale calculated by the solver is often conservative. This is usually robust, but faster convergence is often possible using a more aggressive setting. The maximum iterations set 600 to reach convergent. The CFX-Solver terminated the run after this number of iterations.

2.8 Calculations of Centrifugal fans with difference Blade Outlet Angles

2.8.1 Geometry of Impellers with difference design blade outlet angles

The geometries of the impellers were created in CFX-Geometry. In this study, the casing shape was RC geometry (non-uniform casing) which was attached with difference impellers. The geometries of the impellers show in Fig. 2.7 (a), (b) and (c). Two type impellers were used that the outlet angle of blade is different and the other dimensions are same. The outlet angles 25° and 35°, are called impeller 'A' and impeller 'B' respectively. The comparison of blade outlet angles is shown in Fig. 2.7 (a). The inlet and outlet diameters of the impellers are 142 and 230 mm. The exit blade height is 60.5 mm. Inlet angle is 15°. Its main dimensions are shown in Table 2.3. The impeller is attached to rectangular shaped casing and its size is 350 mm × 350 mm × 158.3 mm.

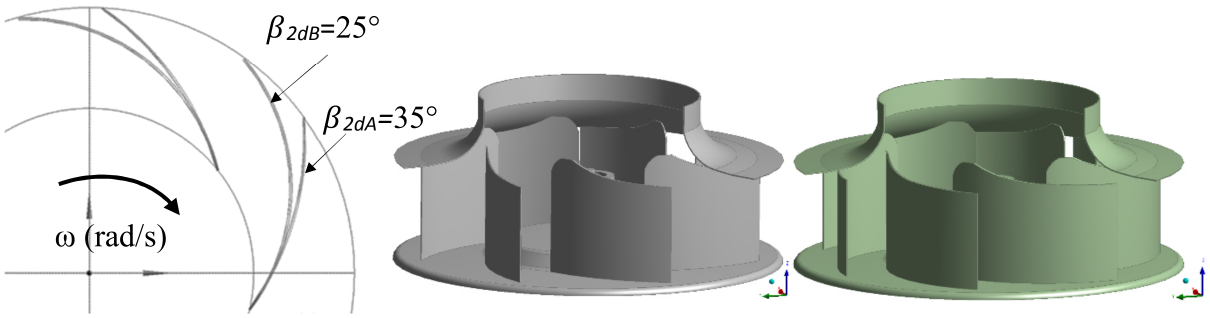

(a) Comparison of blade outlet angles

(b) Impeller 'A' with β_{2dA}=35°

(c) Impeller 'B' with β_{2dB}=25°

Fig. 2.7 Geometries of Impellers

Table 2.3 Main dimensions of impeller

Specifications		Impeller 'A'	Impeller 'B'
Inlet diameter	D_1	142 mm	
Outlet diameter	D_2	230 mm	
Number of blades	B	7	
Exit blade height	H	60.5 mm	
Blade thickness	t	1 mm	
Inlet angle	β_1	15°	
Outlet angle	β_{2d}	35°	25°

There are three computational domains in this model. They are the inlet, rotating domain and the outlet domains. In casing geometry with impeller 'B', the extended length of casing outlet was assumed about twice of casing length and its extended width was about 9 times of casing width as mentioned section 2.7.1.

2.8.2 Mesh creations

The creation of mesh in computational domain is shown in Fig. 2.8 (a) and (b). The mesh in computational RC casing model with impeller 'A' shows in Fig. 2.8 (a) (same Fig. 2.5 (a)). The other RC casing model with impeller 'B' shows in Fig. 2.8 (b). In this section, the blade mesh inflection set in the rotating domain by equation (2.31) to (2.35). The creation of mesh on the blade is inflection, the minimum layer thickness set 0.1 mm and number of layers set 10 layers. The elements and nodes of each computational domain list in Table 2.4.

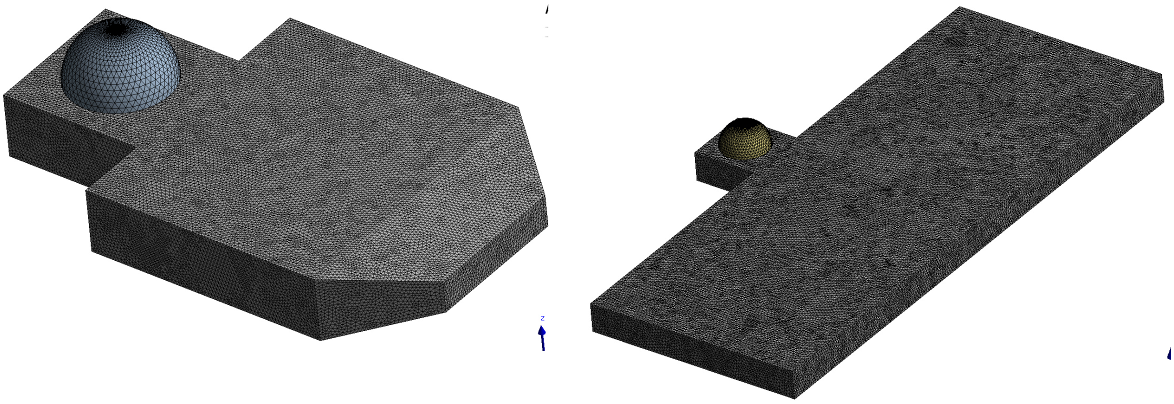

(a) RC casing model with impeller 'A' (b) RC casing model with impeller 'B'

Fig. 2.8 Mesh in computational domain

Table 2.4 Elements and nodes of each computational domain

Mesh	Names on Impellers (Domains)					
	Impeller 'A' with RC casing			Impeller 'B' with RC casing		
	Inlet	Rotating	Outlet	Inlet	Rotating	Outlet
Elements	48407	2258272	1588486	99324	2486547	1530874
Nodes	9330	567415	281500	19046	667850	276903

2.8.3 Setup boundary conditions for steady and unsteady calculations

The flow field of the centrifugal fan with impeller 'A' and 'B' was simulated with the commercial code ANSYS CFX 14.5. In CFX-Pre, the boundary conditions set for steady state calculations of the centrifugal fan with difference impellers. The steady simulation was calculated with RANS and unsteady simulation was calculated with URANS to analyse the flow characteristics of fan. For both calculations, the models are the shear stress transport (SST) turbulence model with automatic wall function. The computational domains set the inlet, the rotating and the outlet. All the domains set the fluid domains and the working fluid was an ideal gas (air at 25°C). The reference pressure set the same with the atmospheric pressure, 1 atm. The inlet and outlet domain set stationary. The rotor domain set the rotating domain which was rotated with 1100 rpm clockwise direction. The static pressure set 0 Pa at the inlet domain and the mass flow rate set in the outlet domain. The solid surfaces in the computational domain are no-slip wall and smooth wall conditions. The interaction plane between the impeller and casing regions is imposed by Frozen-Rotor interface in the steady calculation and Transient Rotor-Stator interface in the unsteady calculation, because the flow characteristics out of the impeller are varied in circumferential location.

In this study, the steady state (RANS) and unsteady (URANS) calculations were done with the four mass flow rates. They are the flow coefficients of $\phi = 0.014, \phi = 0.121, \phi = 0.187, \phi = 0.22$. Where, $\phi = 0.187$ was design flow coefficient.

In the steady state calculation, the flow characteristics do not change with time and thus timescale control set Auto Timescale. Auto Timescale is the default timescale control setting. However, be aware that the Auto Timescale calculated by the solver is often conservative. This is usually robust, but faster convergence is often possible using a more aggressive setting. The maximum iterations set 600 to reach convergent. The CFX-Solver terminated the run after this number of iterations.

In the unsteady state calculation, time dependent behavior for transient simulations in ANSYS CFX is specified through *Time duration* and *Timestep*. The *Timesteps* option provides a way for ANSYS-CFX to track the progress of real time during the simulation, whereas *Time Duration* is a user-specified limit on the length of real time the simulation is to run.

The CFX-Solver uses the *Timestep* and *Time duration* specifications to determine whether to continue the simulation using the next timestep. For example, if the following are set:

Timesteps is set to a *single value* of Δt .

Time Duration is set to *Total Time* option with a value of T.

Then the CFX-Solver will continue to compute solutions at each timestep iteration until $N \times \Delta t \geq T$, where N is the number of timesteps performed by the CFX-Solver. The Courant number is of fundamental importance for transient flows and it tells whether the simulation will converge or blowout. It was used in transient simulations for calculating timestep. The timestep for a one-dimensional grid, was determine by the following equation (2.36).

$$\mathrm{C} = \frac{u\,\Delta t}{\Delta x} < 1 \tag{2.36}$$

Where, u is the fluid speed, Δt is the timestep and Δx is the mesh size, C is Courant number (dimensionless number) which is less than 1. The Courant number calculated in ANSYS CFX is a multidimensional generalization of this expression where the velocity and length scale are based on the mass flow into the control volume and the dimension of the control volume. As an implicit code, ANSYS CFX does not require the Courant number to be small for stability. However, in this simulation, one may need the Courant number to be small to accurately resolve transient details.

In this calculation, the *Initial Time* for a transient simulation is the time before beginning the first timestep of transient simulation, it automatically reads from an initial values file getting by steady state simulation results. The determination of timestep was taken into considering by performing a frequency analysis during the pressure fluctuation. 2^n number of data is required to perform frequency analysis. As a result, 512 timesteps were required for one rotation of the impeller (360°). Thus, in CFX-Pre, the timestep was fixed to 1.06534×10^{-4} seconds, which is equivalent to the progress of the rotor by 1° per time step. The maximum numbers of time steps are 3072 for unsteady calculation which is corresponding to the impeller 6 revolutions. When the final timestep reached 3072 steps, the *Time duration* (*Total Time, T*) was 0.327274s by the equation $T = N\times\Delta t$. The time averaged values were estimated from iteration 1024 to stop iteration 3072 data to catch the average values of flow characteristics.

CHAPTER 3

EXPERIMENTAL APPRATUS AND MEASUREMENTS

In Chapter 3, there are two types of experimental apparatus and measurements. One is wind tunnel apparatus and performances measurements with prototype centrifugal fan. Another is wind duct (PVC) apparatus and performance measurements with model centrifugal fan (3D Printer model fan). The detail expressions are in the following articles.

3.1 Performance test of Centrifugal Fan (Prototype)

The flow characteristics, the static pressure and the flow rate were measured in the experiments. The wind tunnel apparatus, test impeller, casings used in this experiment and measuring system are expressed in the following.

3.1.1 Test impeller

The test impeller used in the experiment is shown in Fig. 3.1 and its main dimension is shown in Table 3.1 (same with Table 2.1). The impeller has seven backward curved blades that the thickness is 1 mm. The backward-curved centrifugal fan is obtained relatively high efficiency and low noise. The type is characterized by the path of the airflow through the fan. Centrifugal fans use a rotating impeller to increase the velocity of an airstream. As the air moves from the impeller hub to the blade tips, it gains kinetic energy. This kinetic energy is then converted to a static pressure increase as the air slows before entering the discharge. Centrifugal fans can generate relatively high pressures. The small size of this type of fan is used in the air conditioner and air cleaner. The rotating speed of the test impeller is fixed to 1100 rpm.

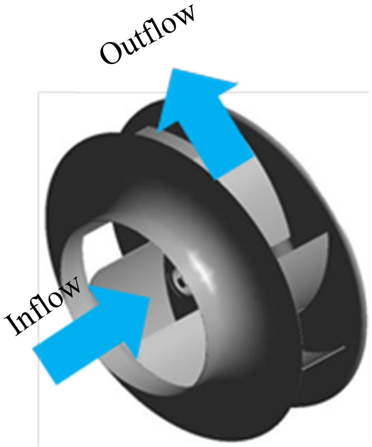

Fig. 3.1 Test impeller

Table 3.1 Main dimension of test impeller

Lists for test impeller		Dimensions
Inlet diameter	D_1	142 mm
Outlet diameter	D_2	230 mm
Exit blade height	H	60.5 mm
Number of blades	B	7
Blade thickness	t	1 mm
Inlet angle	β_{1d}	15°
Outlet angle	β_{2d}	35°
Rotational speed (Clockwise)		1100 rpm

3.1.2 Test casing

The test casing attached the test impeller shows in Fig. 3.2. The centrifugal fan with rectangular casing (RC casing) shows in Fig. 3.2 (a) and this fan with scroll casing (SC casing) shows in Fig. 3.2 (b). In the recent application, the fan is not used with the scroll casing but the rectangular casing, because of the compact size and flexible design. The impeller is attached to rectangular shaped casing (RC casing) and its size is 350 mm × 350 mm × 158.3 mm. The scroll casing (SC casing) created with volute angle 6° and 10 mm gap between the impeller and tongue. The height of the SC casing is the same with RC casing and its height is 158.3 mm. The size of the SC casing exit is 131.32 mm ×158.3 mm.

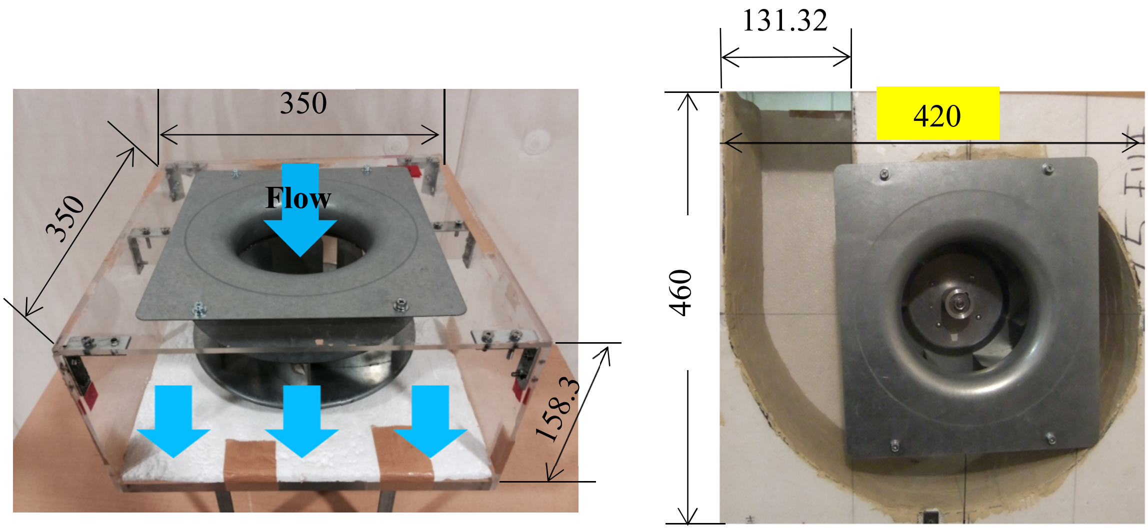

(a) Rectangular casing (RC casing) (b) Scroll casing (SC casing)

Fig. 3.2 Test casing

3.1.3 Wind tunnel experimental apparatus

In this study, the wind tunnel apparatus for performance test shows in Fig. 3.3. The wind tunnel device of 1800 × 1800 × 3000 mm was set up in accordance with JIS B 8330. The gap in the wind tunnel and ducts are filled with silicon so that there is no fluid leakage. Also, sound absorbing materials are attached to the walls shown in the Fig. 3.3. In experiment, the test impeller with corresponding casings was attached as shown in Fig. 3.3. The auxiliary fan (diagonal flow fan) installed at the upper right part of the inlet duct. The air discharged from the auxiliary fan through a honeycomb where the flow is rectifying in the cross section of the flow passage. An orifice plate was installed on the duct for measuring the flow rate. In the wind tunnel, the buffer board was installed to prevent directly flow discharged from the auxiliary fan to the test impeller. A wire netting and a honeycomb was installed for rectifying the flow in the flow passage cross section. In the wind tunnel, there are three holes on the upper wall, on side wall and on floor of the tunnel. The diameter of these holes is 4 mm and they situate 600 mm apart in front of the test fan. These holes provide to measure the static pressure in the wind tunnel mentioned after. The rotational speed of the test impeller is fixed to1100 [rpm] by the inverter. The flow rate is adjusted by the slidac which can change the rotation speed of the auxiliary fan. The rotation speed of the auxiliary fan is adjusted by changing the voltage using the slider. However, when the flow rate is "Q = 0" [m^3/s], the throttle valve is used so that fluid does not flow from the duct.

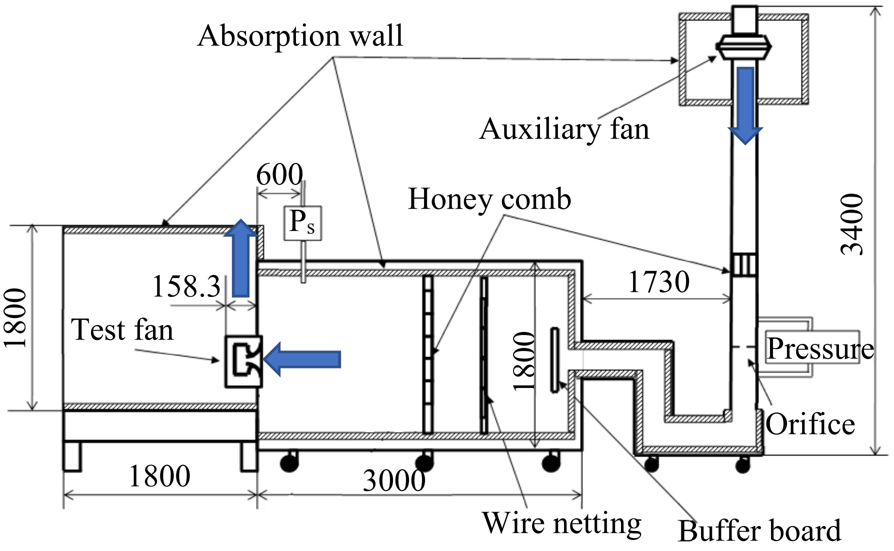

Fig. 3.3 Wind tunnel experimental apparatus

3.1.4 Measurement apparatus and measurement method

3.1.4.1 Measurement apparatus

In this experiment, the flow rate was measured by installing an orifice created in the duct according to JIS Z 8762. The orifice part is shown in Figure 3.4. Figure 3.4 (a) shows the shape of the orifice plate. It is made of an aluminum plate of 235 [mm] × 405 [mm], it is provided with a hole having a diameter d = 100 [mm]. The ratio of a hole diameter to the duct diameter set to 0.5 with respect to the duct diameter D = 200 mm. The shape of the hole is circular and it is concentric with respect to the duct axis.

A flange tap is used as a method of extracting pressure. Fig. 3.4 (b) shows the installation position of the flange tap, and Fig. 3.4 (c) shows the actual attachment part. The pressure outlet on the upstream side of orifice plate is installed in the position, $L_1 = 25.4$ [mm]. The pressure outlet on the downstream side of the orifice plate is installed in the position, $L_2 = 25.4$ [mm]. Four ports each of the upstream side and the downstream side provide four pressures. The upstream side pressures are averaged and this pressure is assigned P_1 [Pa] and the averaging downstream pressure is assigned P_2 [Pa]. By using the measured differential pressure, the volumetric flow rate Q can be obtained by the following equation.

$$Q=\frac{C\cdot\varepsilon\cdot F_r}{\sqrt{1\text{-}\beta^4}}\sqrt{\frac{2(P_1-P_2)}{\rho}} \tag{3.1}$$

Where, C is the outflow coefficient, ε is the expansion coefficient of the gas, F_r is the area of the throttle hole [m^2], β is the throttle diameter ratio, P_1 is the pressure on the upstream side [Pa], P_2 is the pressure on the downstream side [Pa], and ρ is the air density [kg/m^3].

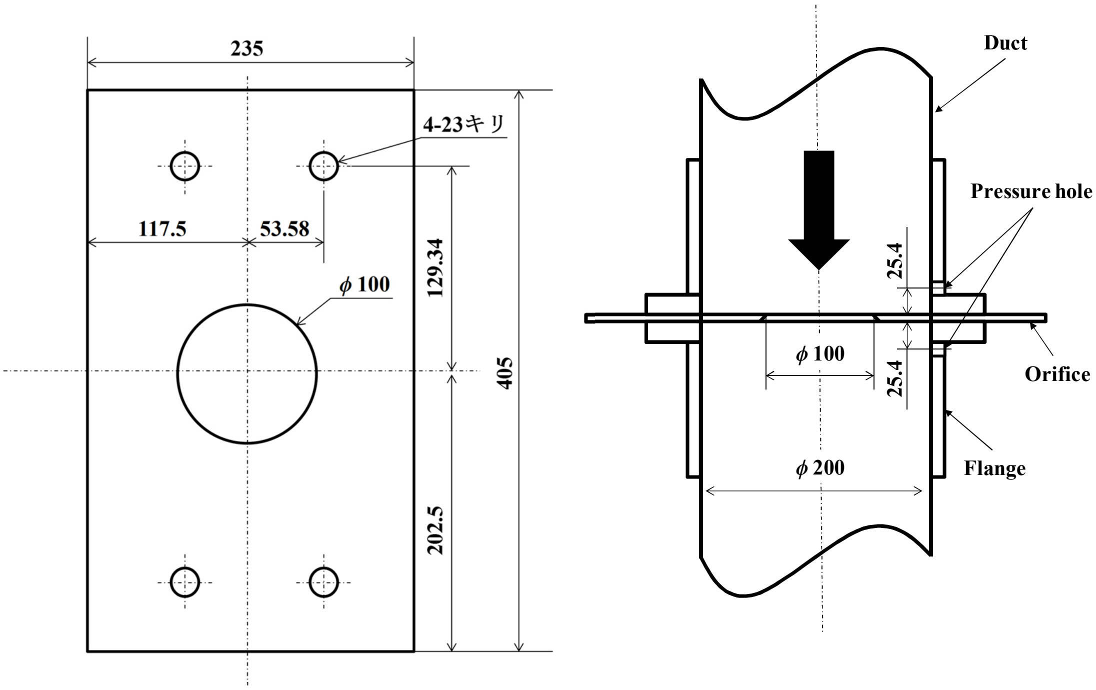

(a) Orifice plate (b) Pressure hole position

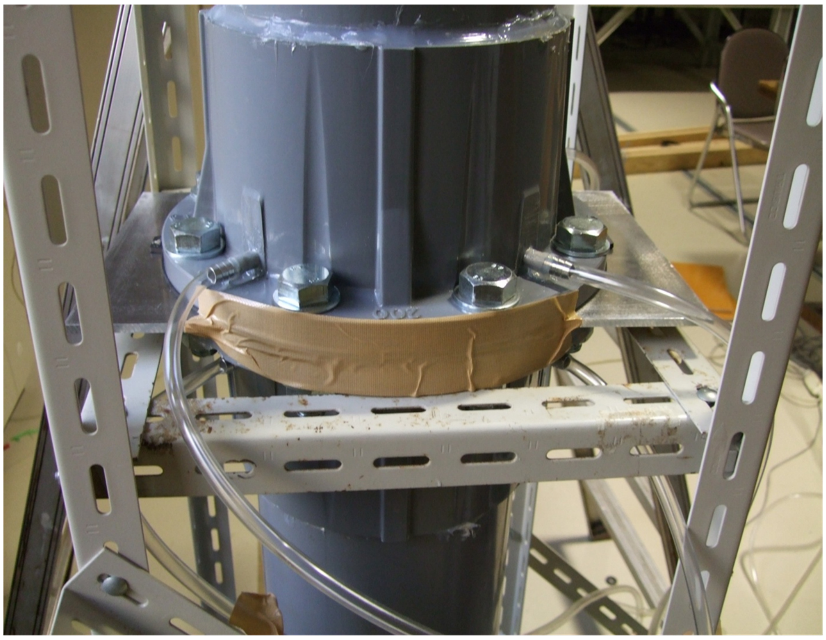

(c) Actual orifice part

Fig.3.4 Orifice

The outflow coefficient C and the expansion coefficient ε of the gas are obtained by the following expressions.

$$C = 0.5961 + 0.0261\beta^2 - 0.261\beta^8 + 0.00052 \left(\frac{10^6\beta}{Re_D}\right)^{0.7} + (0.0188 + 0.0063A^{0.8})\beta^{3.5}\left(\frac{10^6}{Re_D}\right)^{0.3}$$

$$+\left(0.043+0.080e^{-10L_1}-0.123e^{-7L_1}\right)\times(1-0.11A)\frac{\beta^4}{1-\beta^4}-0.031\left(M'_2-0.8M'^{1.1}_2\right)\beta^{1.3} \tag{3.2}$$

$$\varepsilon=1-\left(0.351+0.256\beta^4+0.93\beta^8\right)\left[1-\left(\frac{P_2}{P_1}\right)^{\frac{1}{\kappa}}\right] \tag{3.3}$$

The Reynolds number $Re_D = 3.335 \times 10^4$ in the duct, $L_3 = 0.127$ [mm] which is obtained by dividing the distance from the upstream face of the orifice plate to the upstream pressure outlet port center, and the specific heat ratio $k = 1.4$. M_2' and A, is expressed as the following.

$$M'_2=\frac{2L_1}{1-\beta} \tag{3.4}$$

$$A=\left(\frac{19000\beta}{Re_D}\right)^{0.8} \tag{3.5}$$

From the above equations, the outflow coefficient C = 0.6096, the expansion coefficient of the gas $\varepsilon = 0.9998$, the area of the throttle hole $F_r = 0.007854$ [m^2], and the following equation is obtained by substituting in equation (3.1).

$$Q = 4.937 \times 10^{-3}\sqrt{\frac{2(P_1 - P_2)}{\rho}} \tag{3.6}$$

3.1.4.2 Measurement of Centrifugal fan performance

In this study, the static pressure rise of fan is measured by the differential pressure of the wind tunnel and the atmospheric pressure. The pressure of this tunnel is measured with averaging the three points 600 mm apart from test fan. The pressure in the outlet of the tunnel is kept to the atmospheric pressure. Figure 3.5 shows the test fan attached to the wind tunnel. The number of revolutions of the test impeller used in this experiment is controlled by the inverter. This inverter is connected to a slidac having an input of 100 V and an output of 0 to 130 V to supply voltage. Normally, the inverter and slider are not used at the same time, but in this experiment, the input voltage of the inverter used this time was 120 V, it was impossible to operate the test impeller with the inverter alone in the laboratory environment. The inverter is easy to control the rotating speed, but the loud noise generates. The slidac is not so easy to control the rotating speed, but the low noise generates, thus the slidac is used to measure the noise of fan.

The various measuring equipment used in this study are shown in Fig. 3.6. Figure 3.6 (a) shows a differential pressure transducer (PDV-A manufactured by Kyowa Electric Co., Ltd.) used for measuring the differential pressure of the orifice section (refer Fig. 3.4) and the differential pressure between the wind tunnel and the atmosphere. The allowable capacity is 1 k Pa, and the rated output is 5 V. Features include high response, high accuracy, high sensitivity, noise immunity, ± 5 V voltage output (PDV type), small size and light weight. Measurement of each differential pressure is made by taking the average of differential pressure at 4 points in the orifice part and the pressure difference of 3 points between the tunnel and the atmosphere.

Figure 3.6 (b) shows a DC power supply (Kikusui Electronics Co., Ltd. 7315) used as a power source for the differential pressure transducer. It is a compact and lightweight power supply that can use the maximum output 1.0 A by continuously varying the voltage range of 1 to 15 V with a double type variable resistor with a series type direct current stabilized power supply using transistors.

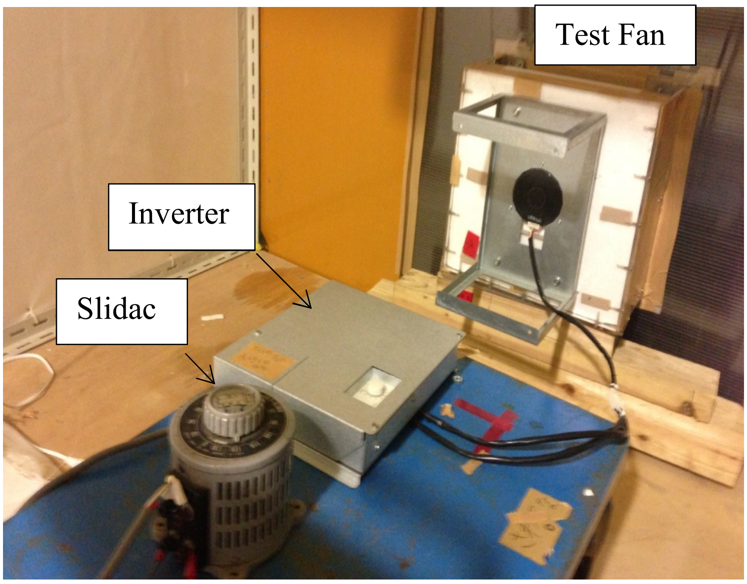

Fig.3.5 The state of the mounting of the test fan

Figure 3.5 (c) shows the data logger (NR-500 manufactured by KEYENCE) used to read the voltage output value of the differential pressure transducer. The read voltage is AD converted by the high-speed analog measuring unit (NR-HA 08 manufactured by KEYENCE), and each differential pressure is output to the personal computer. The data logger has eight input channels, with the highest sampling rate of 1 MHz, the highest resolution of 16 bits, the input signal has a voltage of ± 1000 V and a current of ± 20 mA. In this study, the warm-up time is 15 minutes, the sampling period is 500 ms, the sampling number is 60 pieces, and the differential pressure is collected. Then, the average value of the collected 60 pieces of data was applied as a measurement value to subsequent analysis.

Figure 3.5 (d) shows the digital handy tachometer (HT-4200 made by ONO SOKKI) used for measuring the rotation speed of the test impeller. It is possible to directly display the rotational speed up to 30 to 50,000 revolution / min with high accuracy. In this research, one reflection mark which is a mark of rotation is affixed to the test impeller, and the rotation speed of the test impeller is measured.

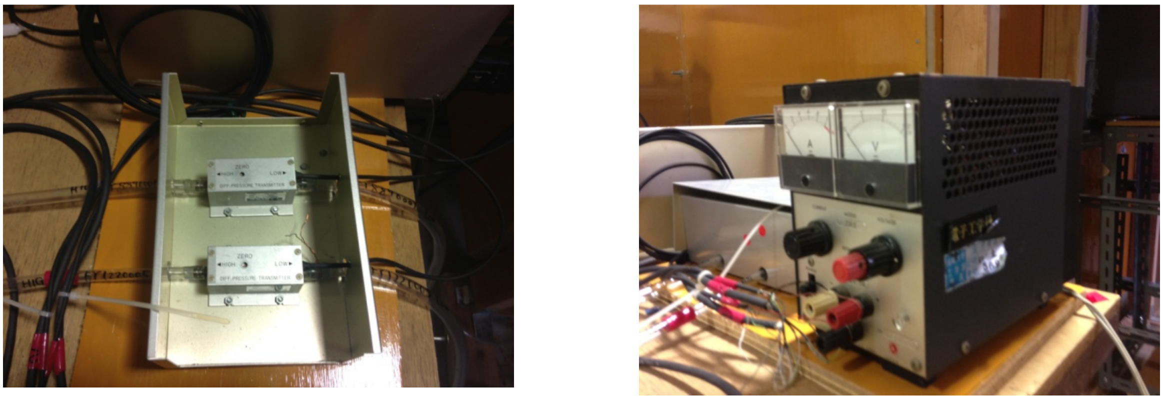

(a) Differential pressure transducer (b) Power

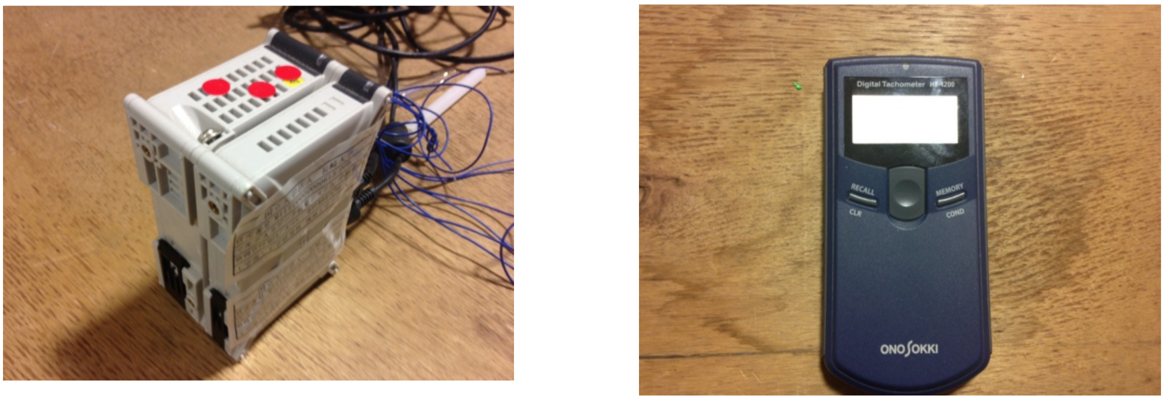

(c) Data logger (d) Digital tachometer

Fig. 3.5 Measuring device

3.2 Performance test of Centrifugal Fan (3D Printer Model fan)

The flow characteristics, the static pressure and the flow rate were measured from the experiments. The wind duct (PVC duct) apparatus, test impeller (3D Printer model), rectangular casing (non-uniform casing) used in this experiment and measuring system are expressed in the following.

3.2.1 Test impeller (3D Printer model impeller)

The test impeller model geometry (3D printer model) used in this experiment is shown in Fig. 3.6. The impeller has seven backward curved blades. The thickness and the blade outlet angle is 3 mm and 25° respectively. The rotating speed of the test model impeller is fixed to 1100 rpm.

The impeller (named impeller ‘B’) geometry was shown in Fig. 2.7 (c) and its dimension was in Table 2.3. The CFX calculation was done with this impeller ‘B’. The performance of the fan with the impeller ‘B’ (refer to the impeller ‘B’ in Fig. 2.7 (c)) can approve with the experimental result. Thus, for doing the performance test, the model impeller (refer to Fig. 3.6) is created with ANSYS-Geometry. In Fig. 3.6, the thickness of the impeller: the blades, the shroud, the hub thickness is created thrice in dimension with ANSYS-Geometry. But, the inlet and the outlet diameter of the impeller does not change. Then, the geometry (~.*agdb) is changed to (~.stp) file by AUTO Desk software. The impeller is created with 3D Printer 2nd generation (Cube). The maximum size of the working table of printer is 14 cm. Thus, for producing the impeller by using the 3D printer, the dimension of the impeller model is reduced to half scale. The model geometry is created the three parts: bell mouth, shroud part and other is hub part including impellers which has supports to attach the shroud. These parts are shown in Fig. 3.6 (a), (b) and (c) respectively. For mounting of bell-mouth in the inlet part of the fan, the gap set 1mm between the bell mouth and the shroud.

The product of 3D printer impeller model shows in Fig. 3.7. The set-up conditions for printing of the model impeller is as following. Units are ‘mm’, print mode is solid, and print material is PLA. The printing time for the bell mouth was 3 hours and 40 minutes, for the hub part was 7 hour and 42 minutes, for the shroud part was 5 hours and 9 minutes.

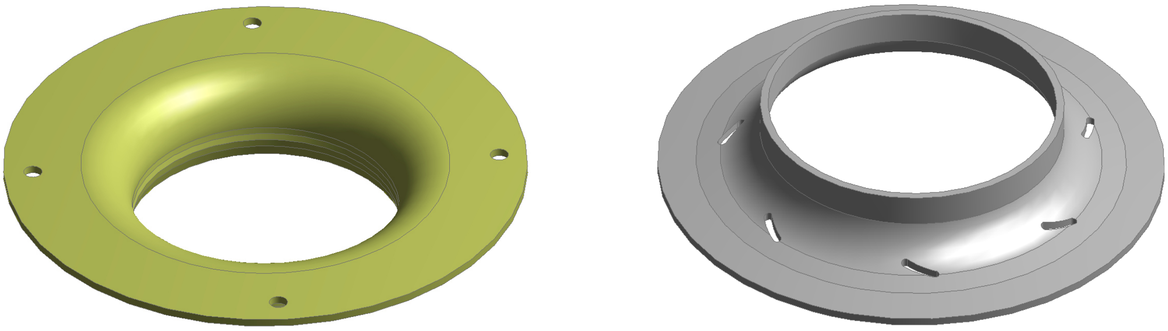

(a) Bell-mouth

(b) Shroud

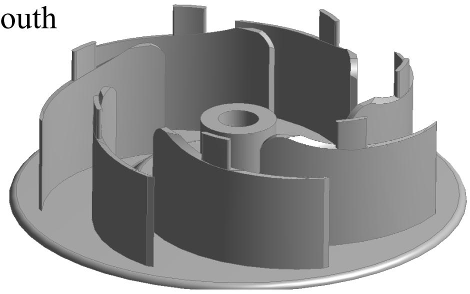

(c) Hub

Fig. 3.6 The test impeller model geometry (3D printer model)

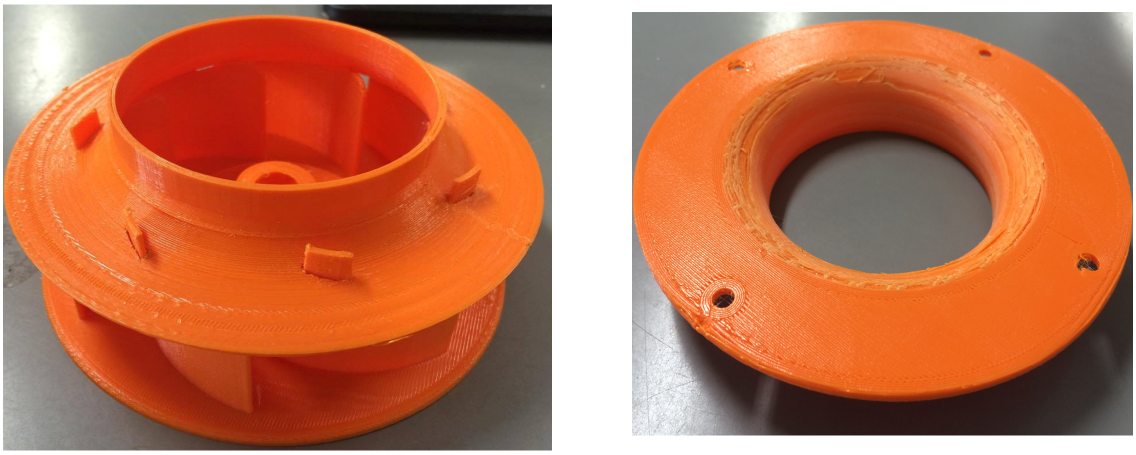

Fig. 3.7 3D printer impeller model

3.2.2 Test casing

The test casing attached the test model impeller shows in Fig. 3.8. The shape of the casing is rectangular (non-uniform casing). The casing dimension is 175 mm × 175 mm × 79 mm. The casing material is Acrylic sheet and its thickness is 4 mm.

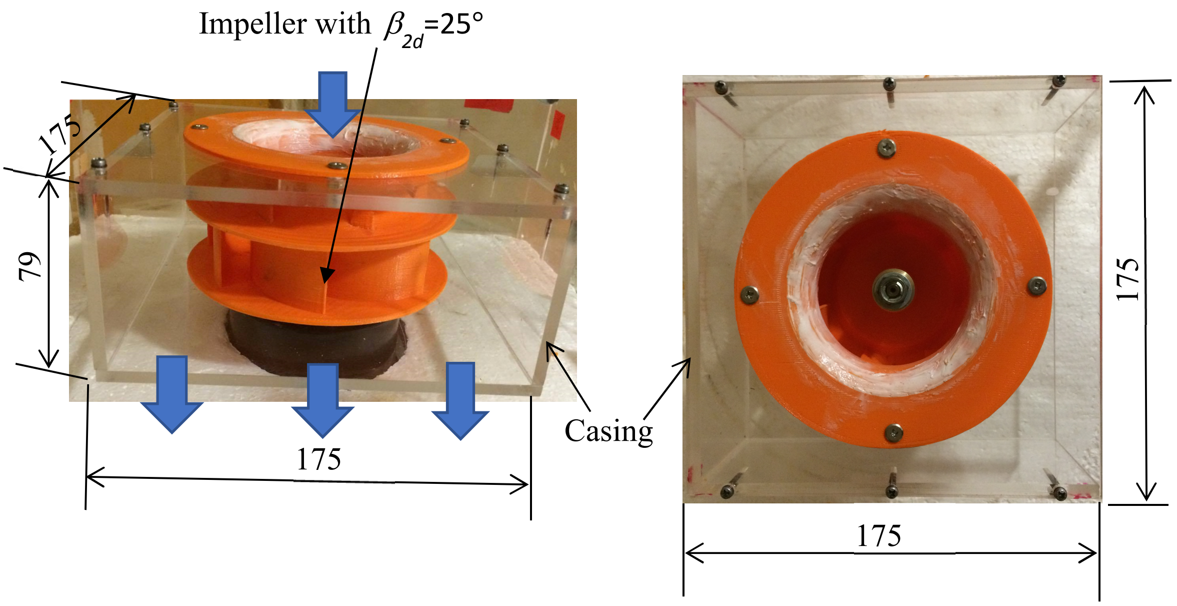

Fig. 3.8 Test casing

3.2.3 Wind duct experimental apparatus (PVC duct)

In this study, the wind duct (PVC duct) apparatus for performance test show in Fig. 3.9. The inside diameter of wind duct is 90 mm and the thickness of duct is 5 mm. The total duct length is 870 mm. The pitot tube is mounted 270 mm apart from the inlet section which is set horizontally inside the duct, there is one hole which has 1mm diameter for measuring total pressure and the hole is set opposite to the flow direction. A needle is vertically set 270 mm on the duct from the inlet section. The static pressure inside the duct is detected from this needle. The dimension of square box is 330 mm × 330 mm, which is connected to the test casing. A needle is vertically set on this box then the static pressure of test fan was measured with it.

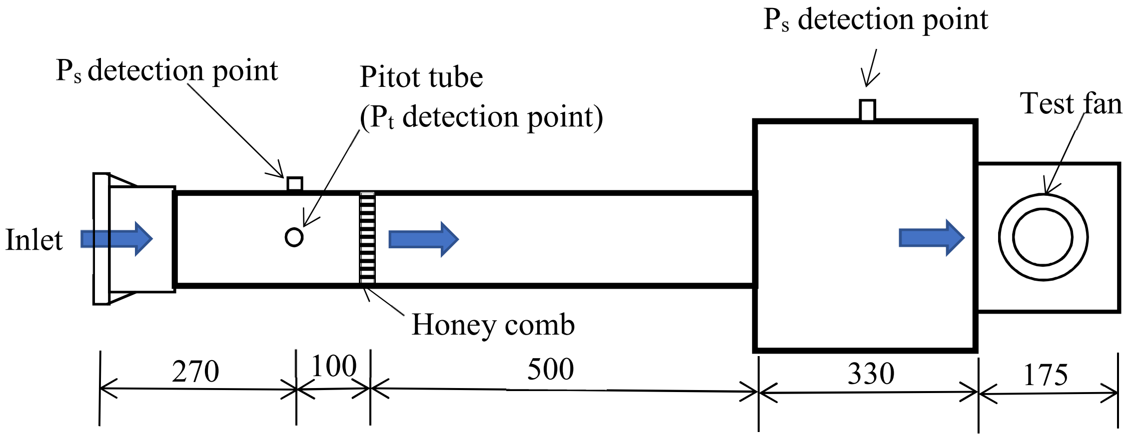

Fig 3.9 Wind duct (PVC duct)

A honeycomb as installed for rectifying the flow in the flow passage cross section. The rotational speed of the test impeller is fixed to1100 [rpm] by the inverter. The flow rate is adjusted by the manual which can change the inlet air velocity. However, when the flow rate is "Q = 0" [m^3/s], the inlet section is fully closed that fluid does not flow inside the duct.

3.2.4 Measurement apparatus and measurement method

3.2.4.1 Measurement apparatus for wind duct

In this experiment, the flow rate was measured by installing the pitot tube horizontally inside the duct and a needle is vertically on the duct. The differential pressure of the air inside the duct was obtained by difference between the total pressure measured with the pitot tube and the static pressure measured with the needle. The static pressure (mm H_2O) was measured with digital micro manometer (DP-50A, OKANO Works. Ltd.,) and the total pressure (mm H_2O) was measured with digital micro manometer (DP-200A, OKANO Works. Ltd.,). The model fan performance measurement apparatus shows in Fig. 3.10.

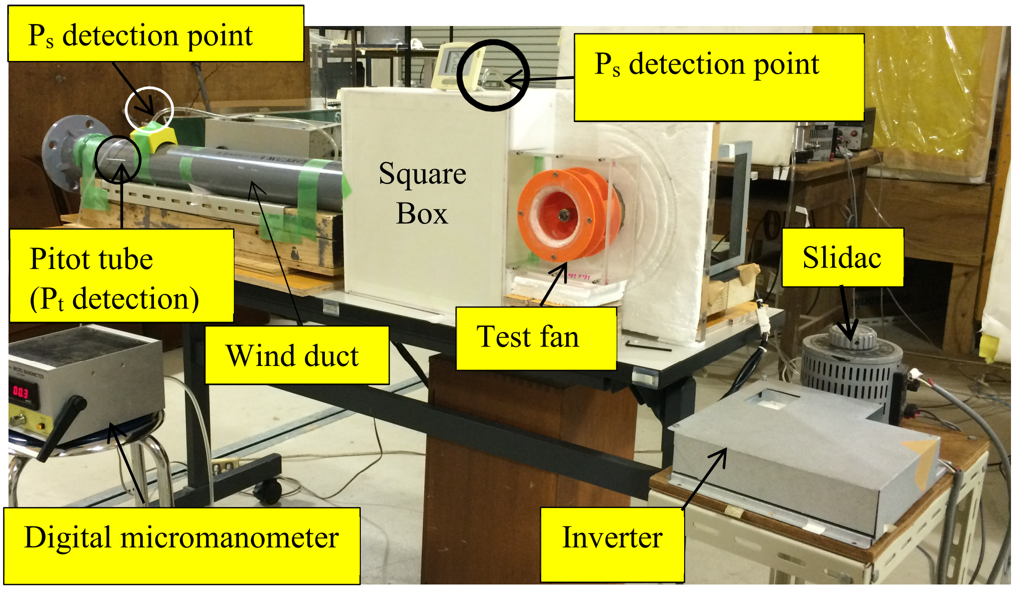

Fig. 3.10 The model fan performance measurement

3.2.4.2 Measurement method

The static and total pressure was measured 270 mm apart from the inlet section of wind duct shown in Fig. 3.11. The static pressure is measured with the needle which has 1 mm diameter and it is vertically located on the duct surface. The measuring method of differential pressure in the wind duct is shown in Fig. 3.12. Figure 3.12 (a) shows the cross-sectional side view of wind duct for the total pressure calibration and Fig. 3.12 (b) is front view of wind duct for differential pressure calculation. The total pressure was calibrated with a hole on the pitot tube. The diameter of a hole is 1 mm. For the total pressure calibrations, the pitot tube was horizontally moved across the wind duct and a hole was set in opposed to the flow direction. The calibration points are located 5 mm, 15 mm, 25 mm, 35 mm and 45 mm apart from the center of wind duct. The hole positions for these calibrations are shown in Table 3.1. The static pressure of test fan was measured with the needle which has 1 mm diameter and it was vertically located on the box surface.

The air entering in the inlet duct was controlled by manually. When the inlet section was fully closed with the enclosure, there was no flow condition, flow rate ‘Q=0’, In this condition, firstly, the hole position was set in the center of duct. Then, the pitot tube was moved to right (refer to Fig. 3.12 (a)), and then, a hole also was moved 5 mm from the center position according to the pitot tube and the total pressure inside the duct was measured with the help of this hole. In the same way, the total pressure was calibrated by the hole position listed in Table 3.1 and also Fig. 3.12 8 (a).

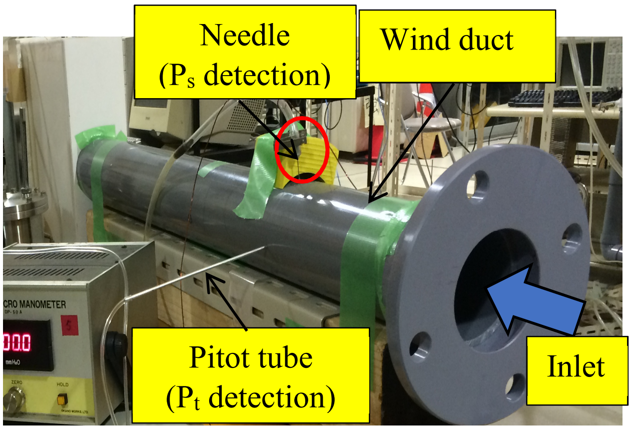

Fig. 3.11 Inlet section of wind duct

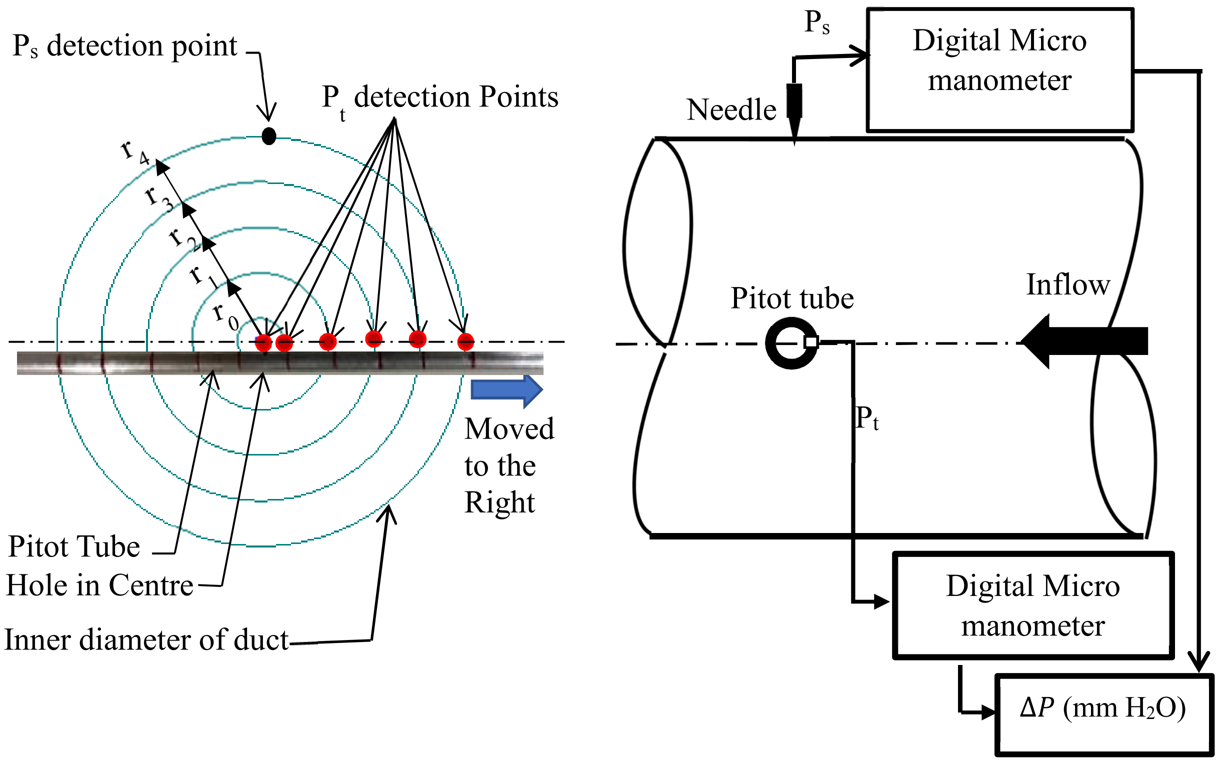

(a) Cross-sectional Side view

(b) Front view

Fig. 3.12 Measuring method of differential pressure inside the wind duct

Table 3.1 Hole positions for total pressure calibrations

Calibration points	Dimensions (mm)
r_0	5
r_1	15
r_2	25
r_3	35
r_4	45

The differential pressure, ΔP (mm H_2O) can be calculated from the equation 3.7, the velocity of air at each calibration point can be calculated with the equation 3.8 and finally the air flow rate, Q can be obtained by the equation 3.9.

$$\Delta P = P_t - P_s \tag{3.7}$$

$$V = \sqrt{\frac{2\,\Delta P\,\rho_w g}{\rho_{air}}} \tag{3.8}$$

Where, V is velocity of air (m/s),

ΔP is the differential pressure or dynamic pressure (mm H_2O),

ρ_w is the density of water ($\rho_w = 1000$ kg/m^3),

ρ_{air} is the density of air at $T = 25.4$°C, ($\rho_{air} = 1.1829$ kg/m^3),

g is gravitational force ($g = 9.8$ m/s^2).

$$\mathrm{Q} = \mathrm{V}_0\pi r_0^2 + V_1\pi(r_1^2 - r_0^2) + \mathrm{V}_2\pi(r_2^2 - r_1^2) + V_3\pi(r_3^2 - r_2^2) + V_4\pi(r_4^2 - r_3^2) \tag{3.9}$$

Where, Q is flow rate of air (m^3/s),

V is the velocity of air at each calibration point (m/s),

r is the hole position for calibrations shown in Table 3.1 (m).

The static pressure of the air P_s, at the outflow region of casing can calculate with the equation (3.9).

$$P_s = \rho g h_s \tag{3.10}$$

Where, h_s is static pressure head (mm H_2O)

CHAPTER 4

Investigation on Aerodynamic Performance of Centrifugal Fan under the influenced of Casing Geometries (Rectangular Casing and Scroll Casing)

The analysis of casing flow is performed by comparing the rectangular casing (RC casing) to scroll casing (SC casing) based on the flow pattern, the performance characteristics and energy loss. In this case, the impeller geometry does not change but the casing geometry (rectangular shape or scroll shape) is changed. This chapter describes 'how does the casing shape influence on the flow pattern, the performance and the energy loss of the centrifugal fan?' This shows the casing shape is important for improving the fan performance and generating high efficiency.

The objectives of this chapter are to make clear the influence of casing shapes, i.e., rectangular and scroll casing, on flow characteristics and the energy loss in the impeller, the casings and the fan. The flow characteristics and energy loss in the casing at each circumferential location will discuss in the following article.

4.1 Flow characteristics

4.1.1 Flow pattern

The flow pattern of the centrifugal fan basically analyzed in the locations: the mid span of the fan, the circumferential plane of the impeller outflow to the casing flow. The flow pattern of simulation fan is discussed for all flow coefficients, i.e., the low flow coefficient, $\phi = 0.014$ to the high flow coefficient, $\phi = 0.26$. The mid span of the centrifugal fan is 30.25 mm.

Figure 4.1 to Fig. 4.5 show the steady state simulation results of the relative velocity of the centrifugal fan for each flow rate. The figures show the velocity for different casing shapes, i.e., rectangular casing (RC casing) and scroll casing (SC casing). These figures are taken in mid-span of the impeller. In $\phi = 0.014$, the low flow rate, the flow pattern of the RC casing fan and SC casing fan shows in Fig. 4.1 (a) and (b). In Fig.4.1 (a) and (b), the separation occurs in the suction side of the all blades. The flow separation occurs in the internal flow of the impeller of RC and SC casing that the very low relative velocities are emerged. The flow deposits in the circumferential direction of the impeller outflow to the casing, thus the outflow velocity is high in the circumference: it is clear in the blade section between B_5 and B_6 in the RC casing fan and from B_2 to B_4 in the SC casing fan. The flow circulates in the circumferential of the casing shown in Fig 4.1 (a) and (b), it does not go to the fan exit. In Fig. 4.1 (a), the wake occurs in the corner of the RC casing and fan exit. In Fig. 4.1 (b), the flow occurs in the narrow scrolling region of the SC casing. the wake occurs in the wide scrolling region and the duct region of SC casing.

Figure 4.2 (a) and (b) shows the flow pattern of the RC casing fan and SC casing fan for the flow coefficient of $\phi = 0.121$. In Fig. 4.2 (a), the separation occurs in the blade suctions, and it is dominant between the blades B_1 to B_4. This may cause the large wake region. In the weak region, the relative velocity is small, so that the absolute velocity of circumferential component become large. The flow with large velocity goes into the back corner of the RC casing to be a jet flow. In Fig. 4.2 (b), the separation occurs in the blade suctions B_1, B_2, B_4, B_5, B_6 and B_7 and near the tongue region, thus there is no flow near the tongue region. The SC casing flow velocity is high in the scrolling region but it is decrease in the duct.

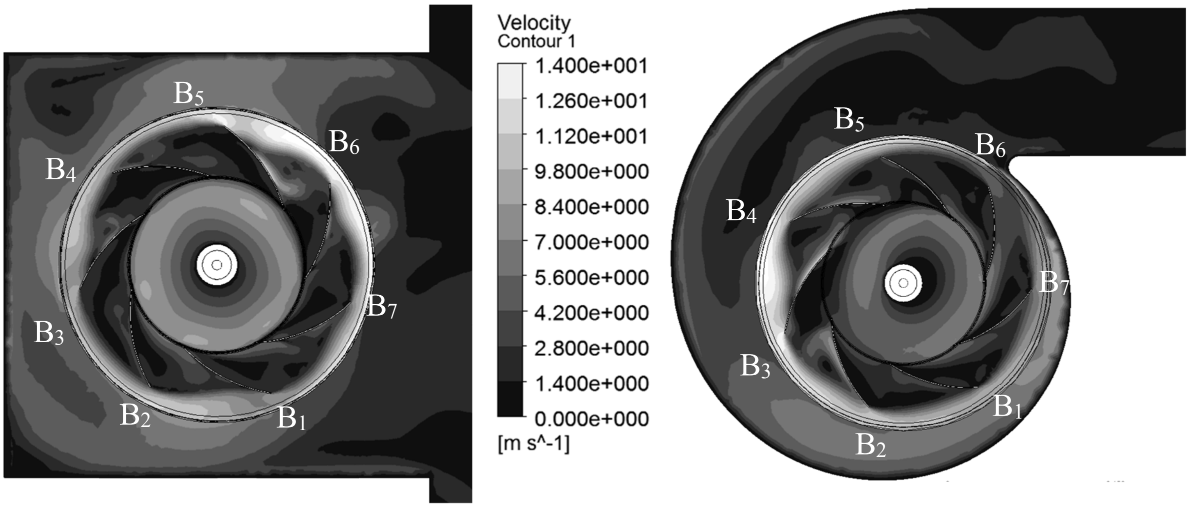

(a) RC casing fan

(b) SC casing fan

Fig. 4.1 Flow pattern ($\phi = 0.014$)

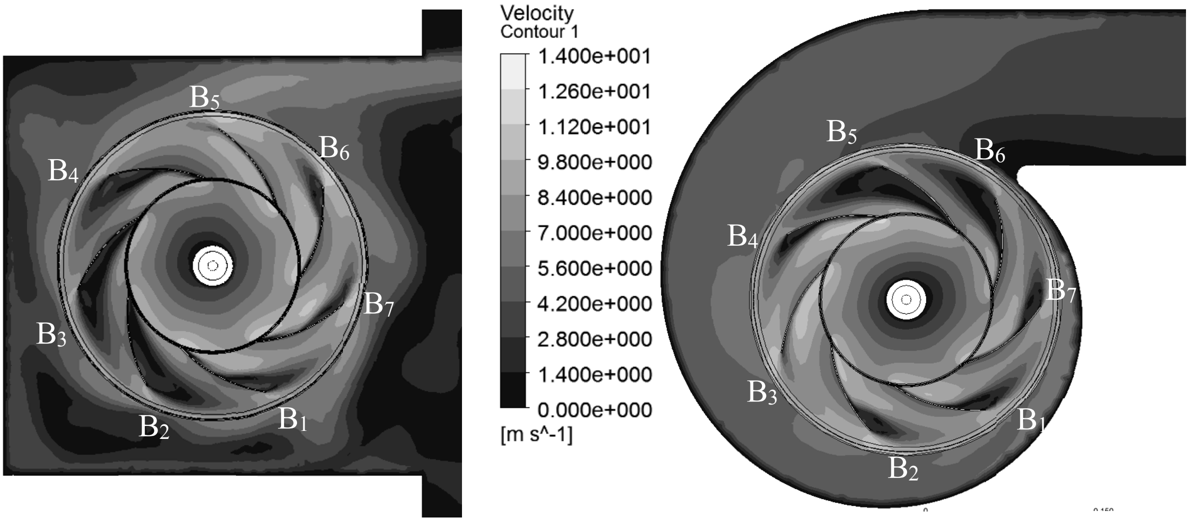

(a) RC casing fan

(b) SC casing fan

Fig. 4.2 Flow pattern ($\phi = 0.121$)

Figure 4.3 (a) and (b) shows the flow pattern of the RC casing and SC casing fan for the design flow coefficient of $\phi = 0.187$. In Fig. 4.3 (a), the separation on the blade suction B_2, B_3, B_4 causes the wake region in the circumferential of RC casing. The wake deposits as a jet near back wall region and the upper corner. In Fig. 4.3 (b), the flow separation is on the blade suction of B_1, B_2, B_3, B_7 and it may cause the relatively large wake near the tongue region. The casing flow pattern is uniform in circumferential of the SC casing but non-uniform in circumferential of the RC casing.

Figure 4.4 (a) and (b) shows the flow pattern of the RC casing and SC casing for the flow coefficient of $\phi = 0.237$. In Fig. 4.4 (a), the flow separation on the blade B_2 and B_3 causes the wake region in the circumferential of the RC casing, it strikes the casing back wall. In Fig. 4.4 (b), the flow separation on the blade B_7 causes the low flow region in the duct near the tongue. The flow velocity is high in the blade suction B_5 and B_6, it causes the high flow velocity in the duct.

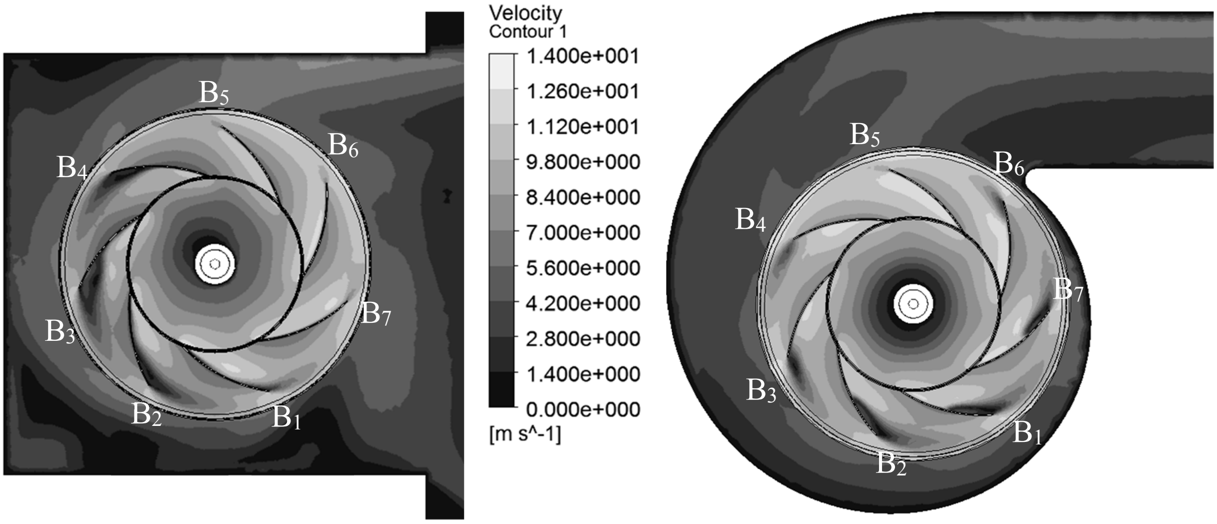

(a) RC casing fan (b) SC casing fan

Fig. 4.3 Flow pattern ($\phi = 0.187$)

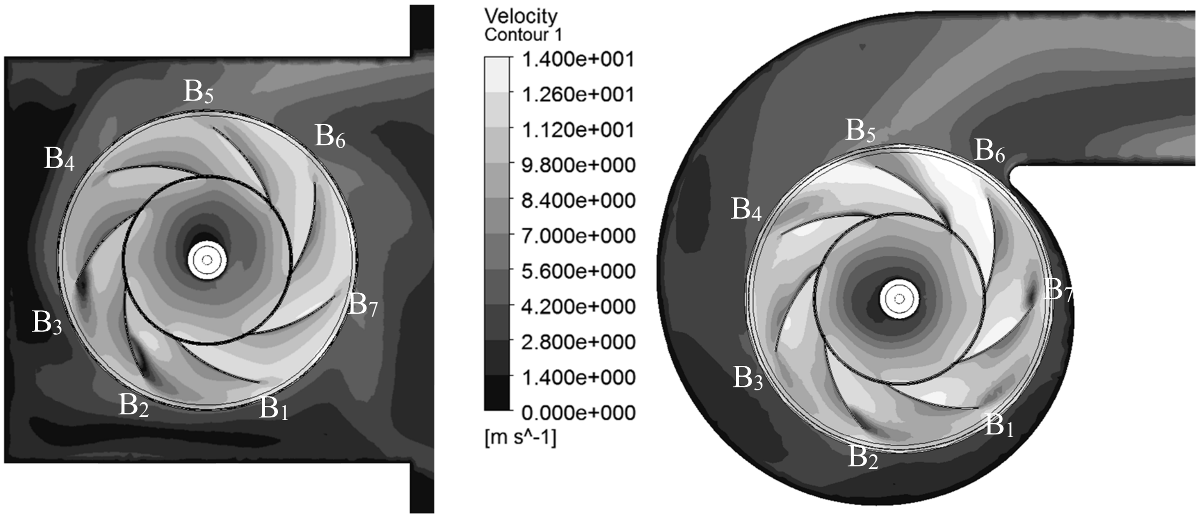

(a) RC casing fan (b) SC casing fan

Fig. 4.4 Flow pattern ($\phi = 0.237$)

Figure 4.5 (a) and (b) shows the flow pattern of the RC casing and SC casing for the flow coefficient of $\phi = 0.26$. In Fig. 4.5 (a), the flow separation occurs only on blade suction B_2 and the wake occurs in the rear corner of RC casing. In the SC casing fan shown in Fig. 4.5 (b), the flow separation appears in the leading edge of the blades B_3, B_4 and B_5, it is located on the pressure side of these blades then the low velocity regions are generated. The high velocity region occurs in the blade suctions of B_1, B_2 and B_3.

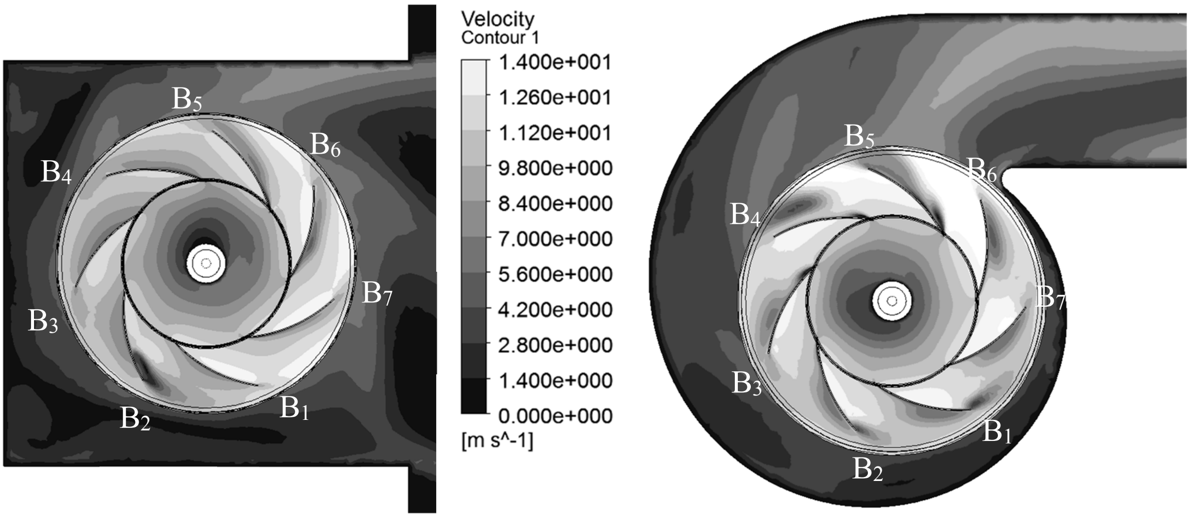

(a) RC casing fan

(b) SC casing fan

Fig. 4.5 Flow pattern ($\phi = 0.26$)

The contour of the relative velocity outflow of impeller of RC casing fan shown in Fig. 4.6 (a) to Fig. 4.10 (a) and SC casing fan shown in Fig. 4.6 (b) to Fig. 4.10 (b). These figures show that the location to analysis the circumferential flow pattern of the impeller outflow. The following figures 4.6 (c), (d) to 4.10 (c), (d) shows that analysis of the flow pattern in the circumferential of the impeller outflow to the casing flow.

In Fig. 4.6 (c) and (d), the non-uniform flow pattern occurs in the circumferential of RC casing fan and SC casing fan in the low flow coefficient. The detail of these figures with each blade section of circumferential outflow is shown with Fig. 4.6 (c-1) to (c-4) for RC casing and Fig. 4.6 (d-1) to (d-4) for SC casing. The high flow velocity occurs in the outflow section B_5 to B_7 in RC casing fan and between B_3 and B_4 in SC casing fan. As the flow separation occurs in all blade sections, the low velocity flow pattern is influence in circumference of the impeller outflow to the casing.

Figure 4.7 (c) and (d) shows that the non-uniform flow pattern occurs in the circumferential of the impeller outflow for RC and SC casing fan. In RC casing fan shown in Fig. 4.7 (c), the circumferential distribution of flow velocity in the impeller outflow region; between B_1, B_2, B_3 and B_4, is low and this flow causes to become the wake jet flow region (large velocity region) in the circumferential of back of the RC casing. The non-uniform flow

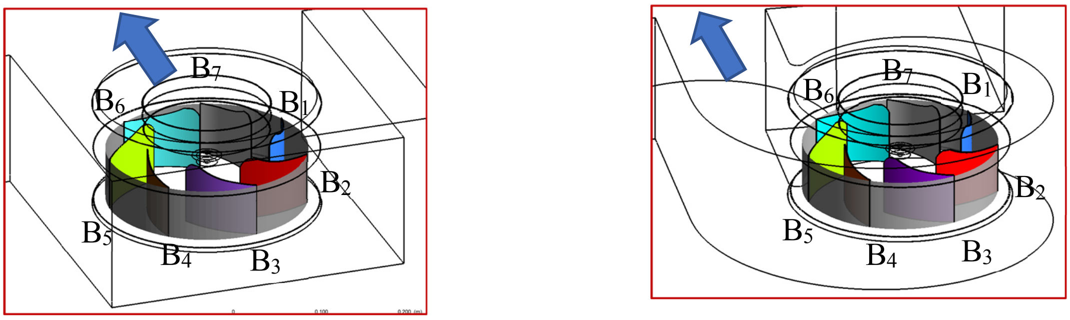

(a) Circumferential outflow location (RC casing fan)

(b) Circumferential outflow location (SC casing fan)

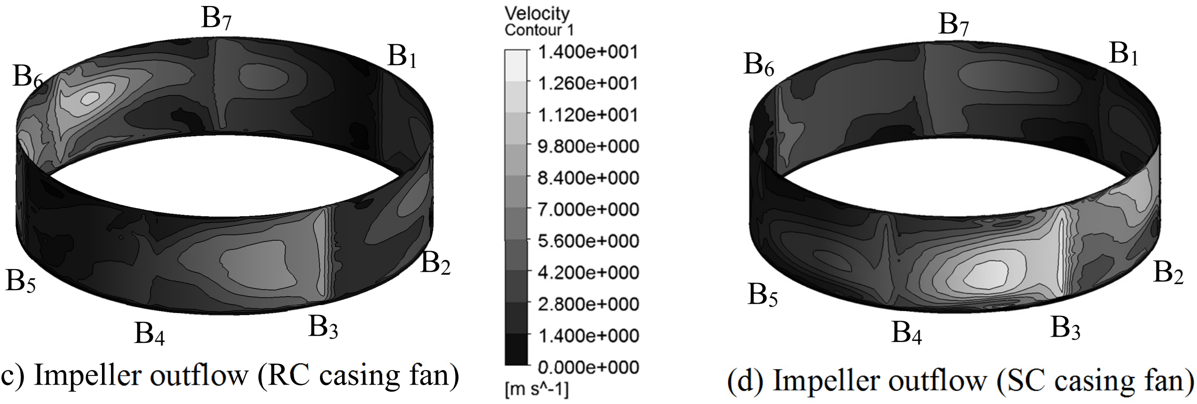

(c) Impeller outflow (RC casing fan)

(d) Impeller outflow (SC casing fan)

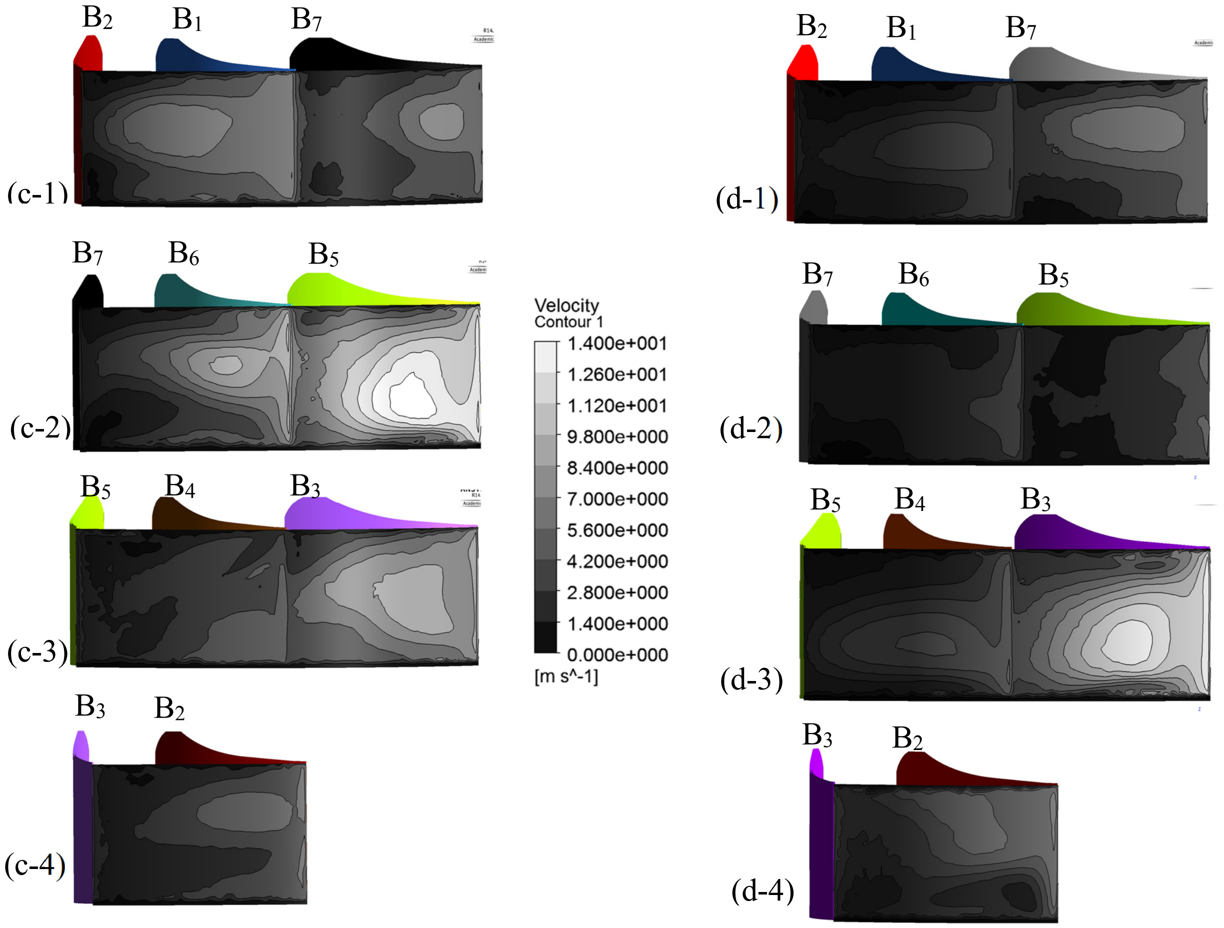

Fig. 4.6 Circumferential outflow pattern (ϕ = 0.014)

(a) Circumferential outflow location (RC casing fan)

(b) Circumferential outflow location (SC casing fan)

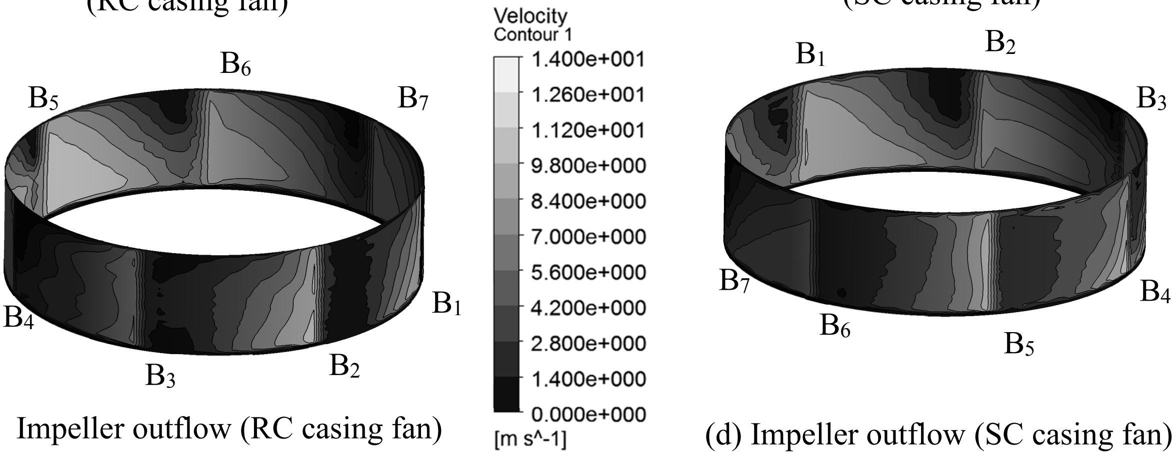

(c) Impeller outflow (RC casing fan)

(d) Impeller outflow (SC casing fan)

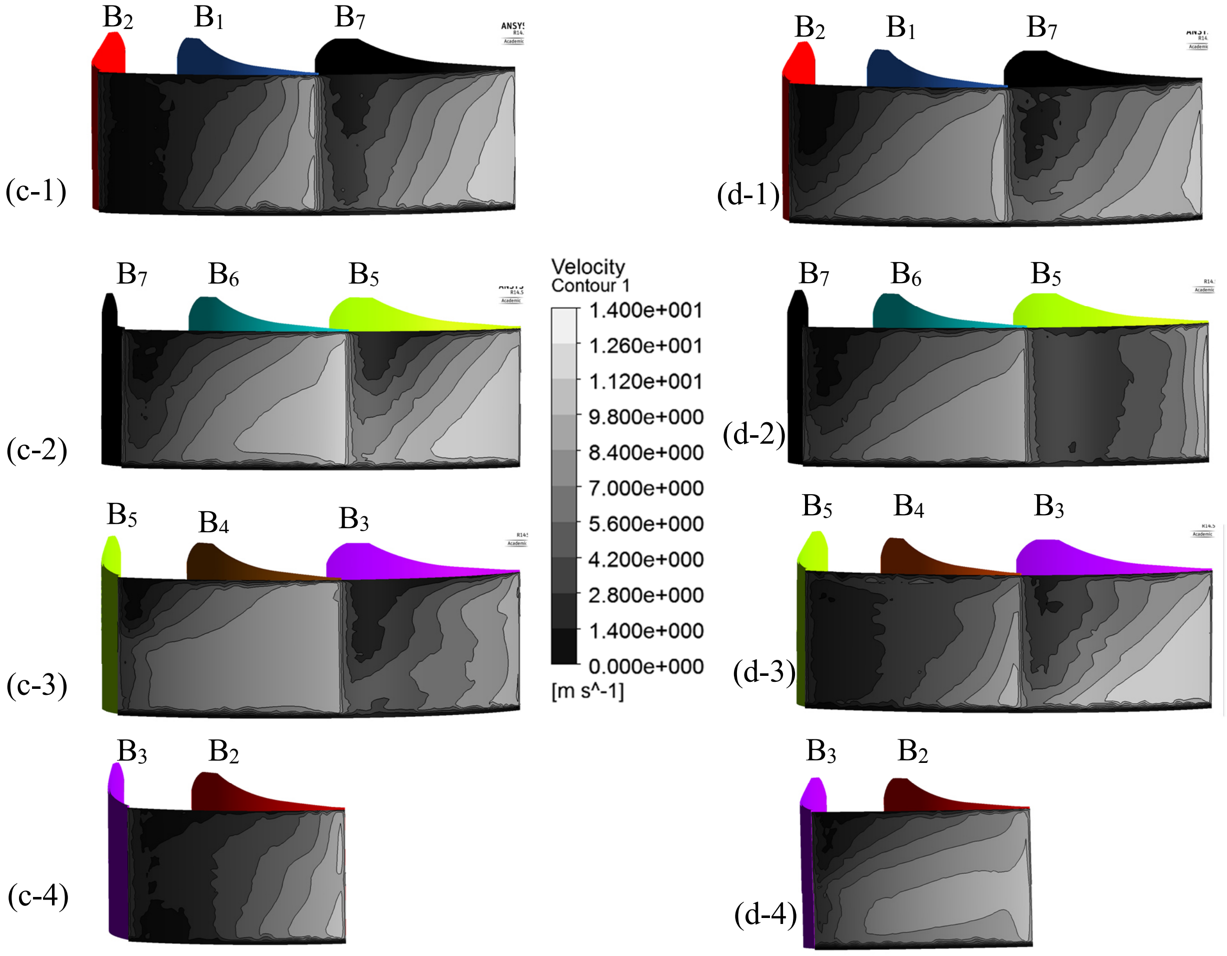

Fig. 4.7 Circumferential outflow pattern (ϕ = 0.121)

(a) Circumferential outflow location (RC casing fan)

(b) Circumferential outflow location (SC casing fan)

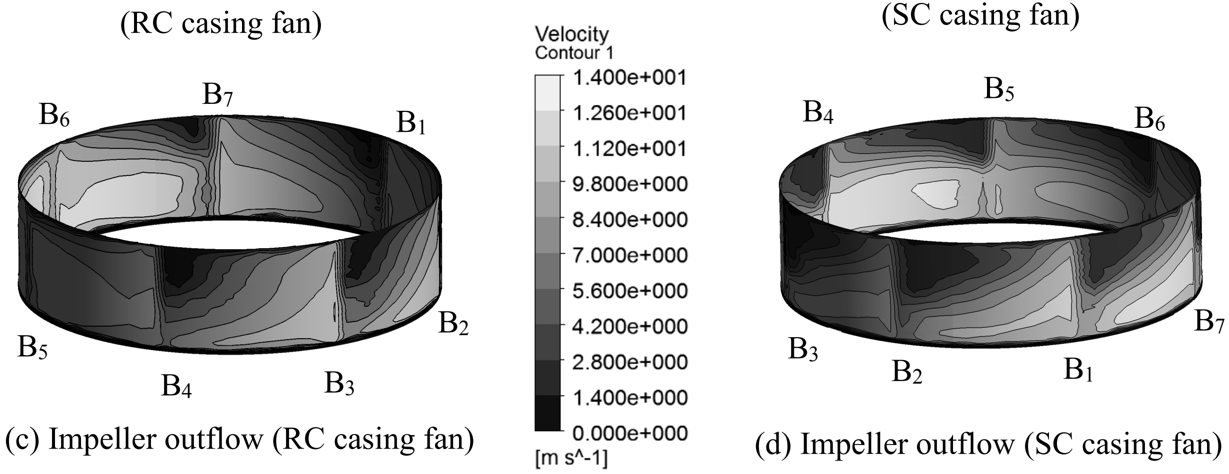

(c) Impeller outflow (RC casing fan)

(d) Impeller outflow (SC casing fan)

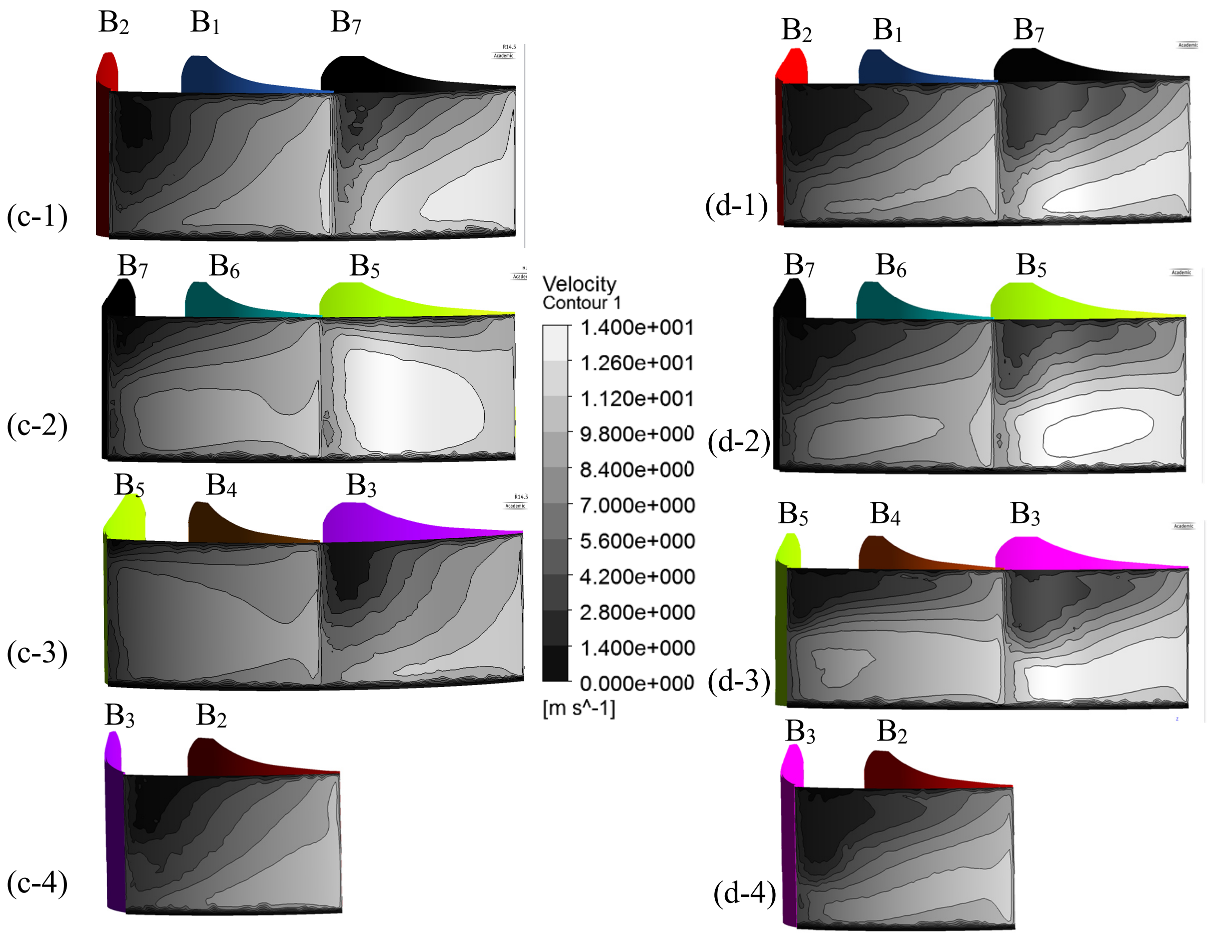

Fig. 4.8 Circumferential outflow pattern ($\phi = 0.187$)

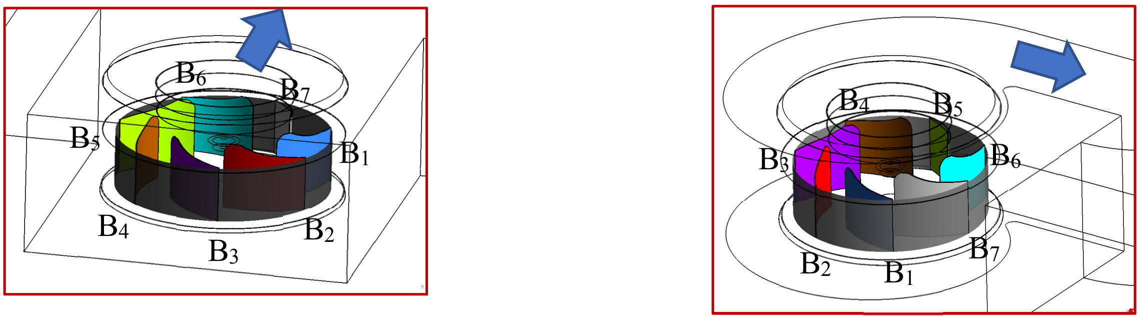

(a) Circumferential outflow location (RC casing fan)

(b) Circumferential outflow location (SC casing fan)

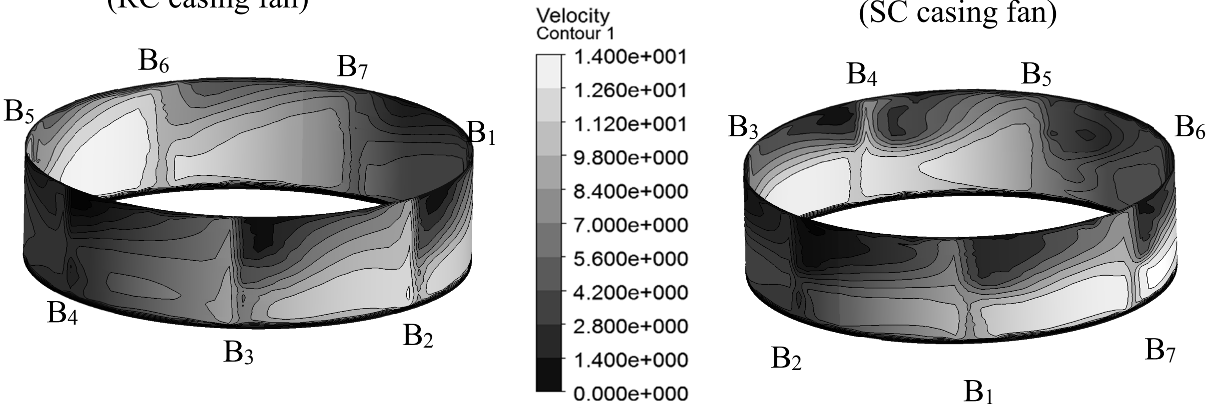

(c) Impeller outflow (RC casing fan)

(d) Impeller outflow (SC casing fan)

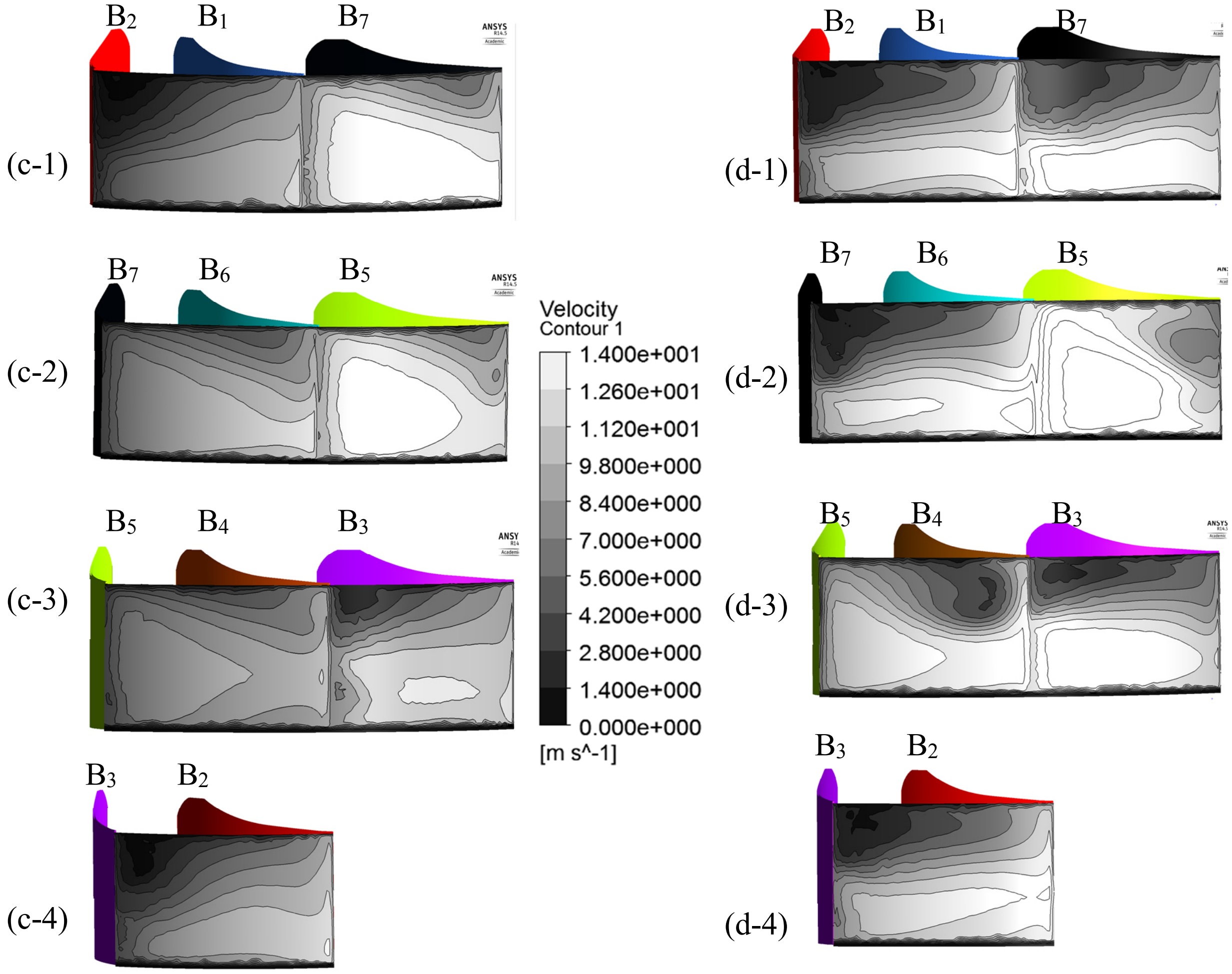

Fig. 4.9 Circumferential outflow pattern ($\phi = 0.237$)

(a) Circumferential outflow location (RC casing fan)

(b) Circumferential outflow location (SC casing fan)

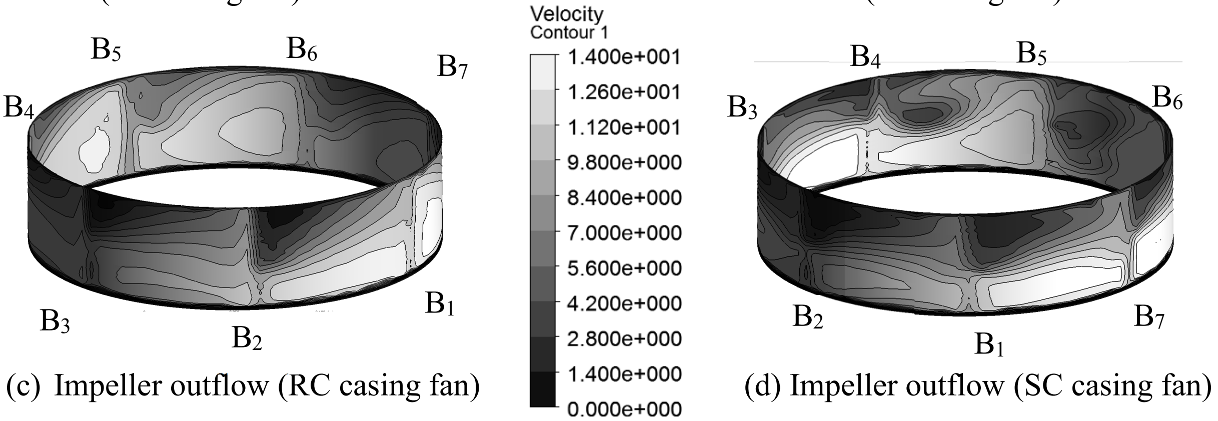

(c) Impeller outflow (RC casing fan)

(d) Impeller outflow (SC casing fan)

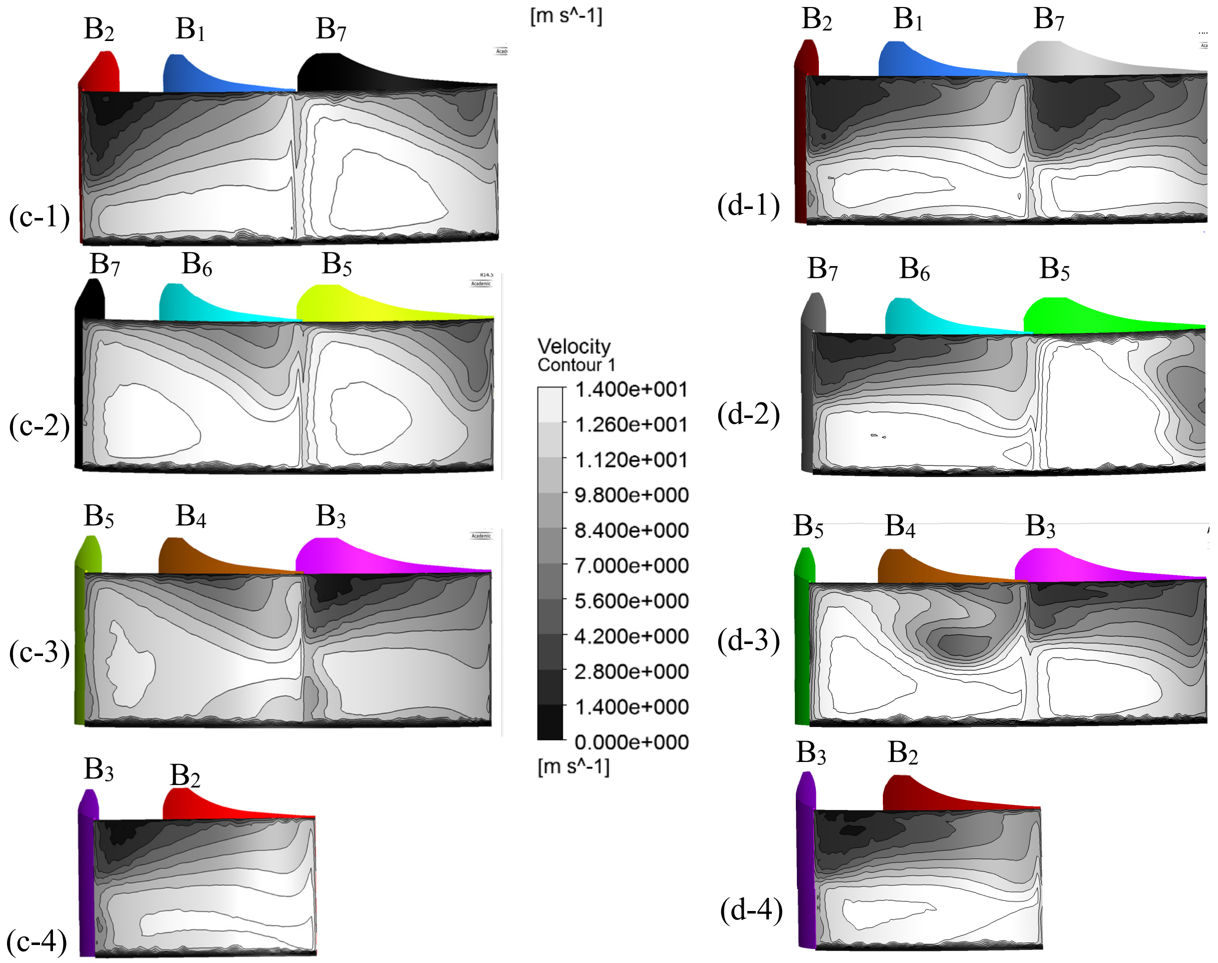

Fig. 4.10 Circumferential outflow pattern ($\phi = 0.26$)

patterns are dominant in the blade sections: B_1-B_2 shown in Fig. 4.7 (c-1), B_4-B_5 shown in Fig. 4.7 (c-3) and B_2-B_3 shown in Fig. 4.7 (c-4). In Fig. 4.7 (d), in SC casing, the flow pattern is non-uniform in velocity contour in the circumferential of the impeller outflow region B_4 to B_6 near the tongue. The dominant non-uniform sections are B_5-B_6 shown in Fig. 4.7 (d-2) and B_4-B_5 shown in Fig. 4.7 (d-3).

In the design flow rate ($\phi = 0.187$), the flow pattern in the circumferential location of the impeller occurs in non-uniform flow shown in Fig. 4.8 (c). The flow velocity in circumferential of impeller outflow B_2 to B_4 which has low flow region caused by separation on blades. This flow leads to become the wake jet flow region in the back of the circumferential location of RC casing and thus casing flow pattern is non-uniform. The flow velocity is high in the circumferential outflow region B_6, B_7 and B_1, and the flow in this region goes out to the fan. The non-uniform flow pattern dominant in the circumferential of the impeller blade sections: B_5-B_7 shown in Fig. 4.8 (c-2) and B_4-B_5 shown in Fig. 4.8 (c-3). In the SC casing fan shown in Fig. 4.8 (d), the circumferential flow pattern is uniform from the impeller outflow to the casing. The detail of circumferential uniform flow pattern shows in each blade section shown in Fig. 4.8 (d-1) to (d-4), it generates to the casing of SC casing fan.

In Fig. 4.9 (c), the non-uniform flow pattern occurs in the circumferential location of the impeller out flow to the casing. The flow in region B_1, B_2 to B_3 leads to become the wake in the circumference of the casing's back. The outflow region B_5, B_6, B_7 and B_1 is fully developed to come out the flow to fan exit. The non-uniform flow pattern generates in each blade section shown in Fig. 4.9 (c-1) to (c-4). In Fig. 4.9 (d), the non-uniform flow pattern occurs in the circumferential of the impeller outlet to the casing of the SC casing fan. The high velocity distributes in the circumferential of the impeller blade sections B_3-B_4 shown in Fig 4.9 (d-3) and B_5-B_6 shown in Fig. 4.9 (d-2).

In Fig. 4.10 (c), the non-uniform flow pattern generates in the circumference of the impeller outflow to the casing of RC casing fan. In the flow region B_1-B_2 and B_2-B_3, the outflow velocity is low. In the circumferential region B_3-B_4, B_4-B_5, B_5 - B_6 and B_6-B_7, the outflow velocity is well developed to the fan exit. The non-uniform flow generates in the circumferential of the impeller in each blades section; shown in Fig. 4.10 (c-1) to (c-4), to the casing of RC casing fan. In Fig. 4.10 (d), the non-uniform flow pattern distributes in the circumferential of the impeller outflow to the casing of SC casing fan. The low flow velocity generates near the shroud region. The circumferential non- uniform flow pattern shows in Fig. 4.10 (d-1) to (d-2).

4.1.2 Static pressure distribution

The static pressure distribution analyses in the mid span of the impeller and the circumferential of the impeller outflow to the casing. Figure 4.11 to Fig. 4.15 shows the mid span location of the impeller for analysing the static pressure distribution of the RC casing fan with the SC casing fan in each flow rate.

Figure 4.11 shows the static pressure distribution of the RC and SC fan in the low flow rate ($\phi = 0.014$). Figure 4.11 (a) shows the contour line of the static pressure of the RC casing fan. High static pressure generates in the circumference of the RC casing fan. The highest static pressure occurs in the corner of the casing back and the exit of the fan where there is no flow.

Figure 4.11 (b) is the static pressure distribution of the SC casing fan. The high pressure distributes in large scrolling region of SC casing, the tongue, and the outlet duct. With low flow coefficient, high static pressure is generated around the circumference of the fan.

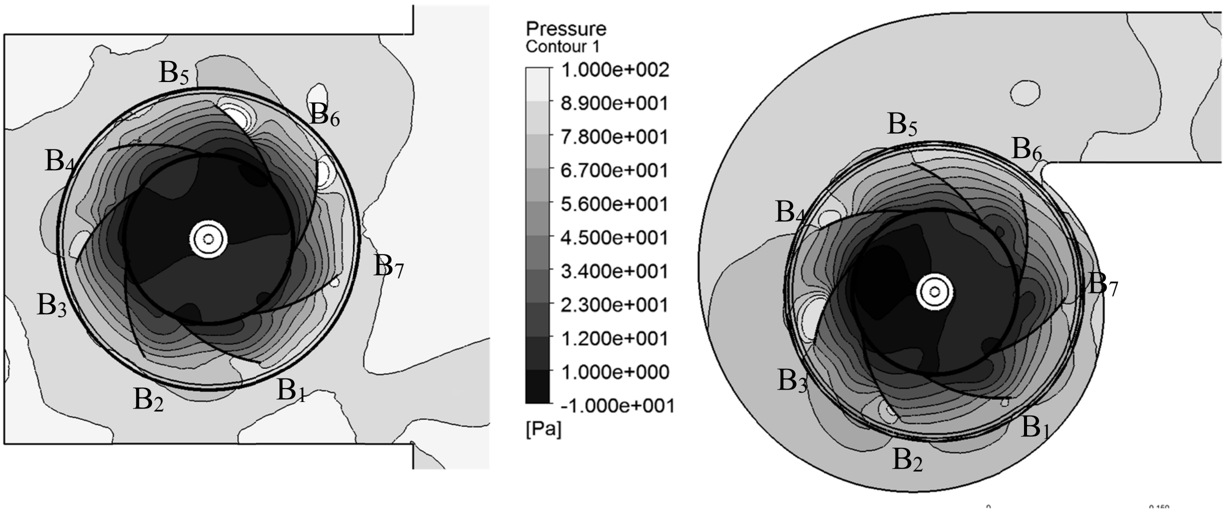

(a) RC casing fan

(b) SC casing fan

Fig. 4.11 Static pressure distributions ($\phi = 0.014$)

Figure 4.12 shows the static pressure distribution of the RC and SC fan in the flow rate ($\phi = 0.121$). Figure 4.12 (a) shows the contour line of the static pressure of the RC casing fan. The static pressure is high in the blade region B_3, B_4 and B_5 of the impeller outlet. This high static pressure generates in the circumference of the impeller outflow to the circumference of the casing back for the RC casing fan. There is wake region in the casing back. Figure 4.12 (b) shows the contour line of the static pressure of the SC casing fan. The high static pressure generates in the impeller outflow region to the casing scrolling region. The high static pressure dominants to blade region, B_5, B_6 and B_7, then these pressures distribute to the tongue region and finally to the duct.

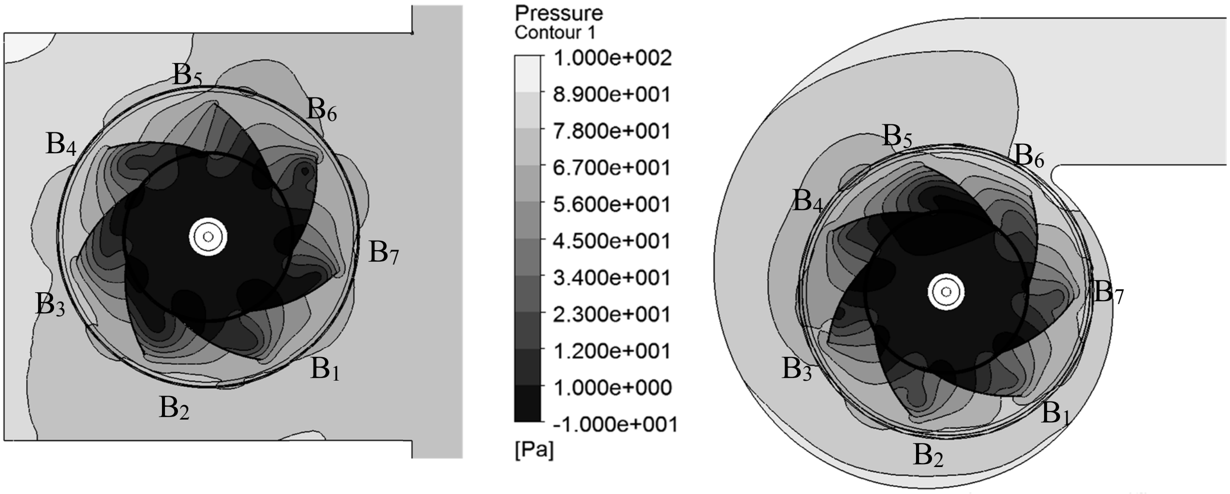

(a) RC casing fan

(b) SC casing fan

Fig. 4.12 Static pressure distributions ($\phi = 0.121$)

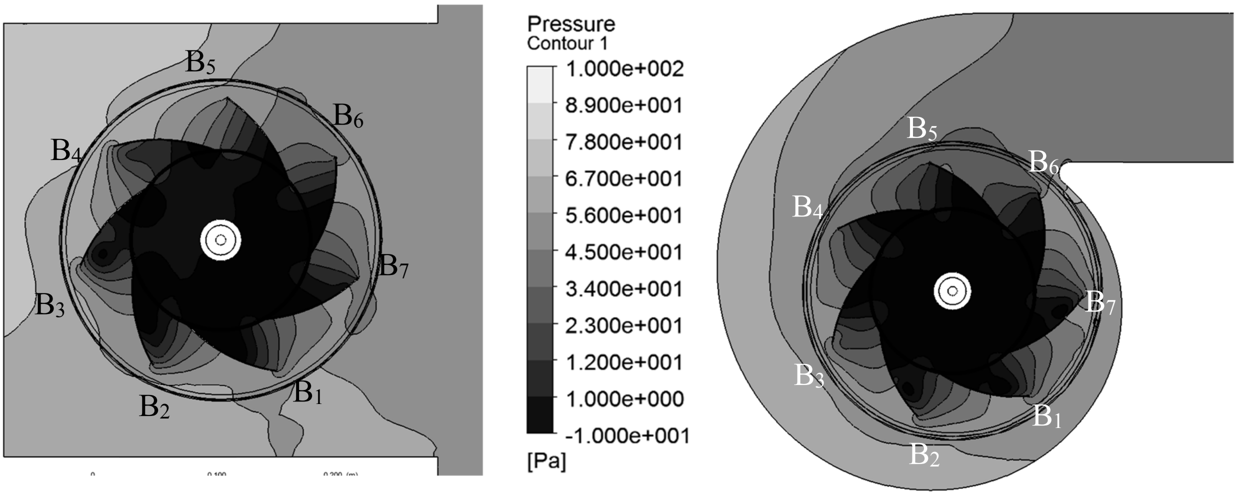

(a) RC casing fan

(b) SC casing fan

Fig. 4.13 Static pressure distributions ($\phi = 0.187$)

Figure 4.13 shows the static pressure distribution of the RC and SC fan in the design flow rate ($\phi = 0.187$). Figure 4.13 (a) shows the contour line of the static pressure of the RC casing fan. The static pressure is high in impeller outflow of the blade region B_3, B_4 and B_5, then these pressures generates to the circumferential direction of the casing. The highest static pressure occurs in the upper corner of the casing back and these pressure is decreasing to the exit of the fan. Figure 4.13 (b) shows the contour line of the static pressure of the SC casing fan. The low static pressure generates in the impeller outflow of the blade region B_4, B_5, and B_6. The high static pressure generates in the scroll region of the SC casing near the wall and tongue region.

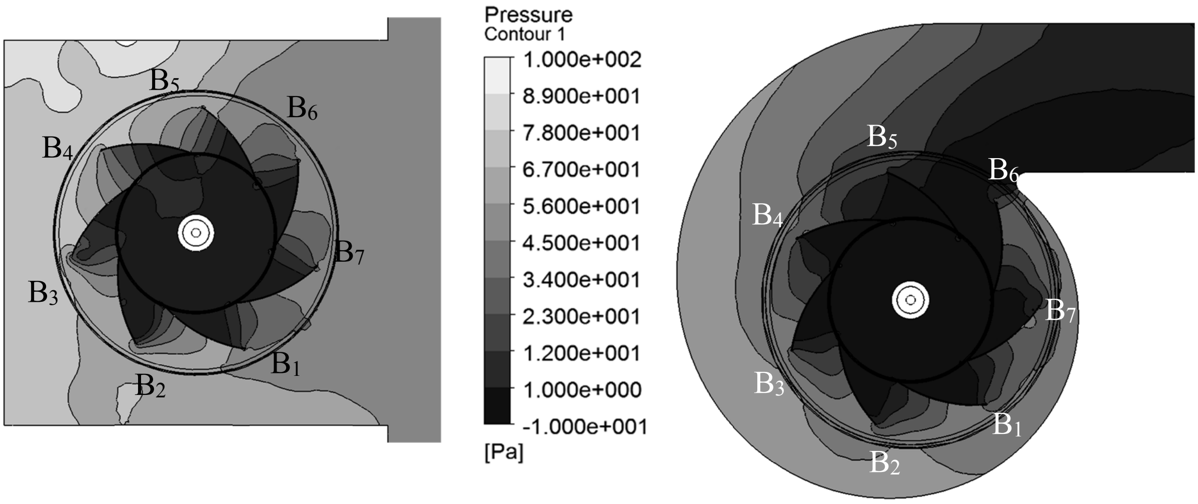

(a) RC casing fan

(b) SC casing fan

Fig. 4.14 Static pressure distributions ($\phi = 0.237$)

The static pressure distribution of the RC and SC fan for the flow rate ($\phi = 0.237$) is shown in Fig. 4.14 (a) and (b). The high static pressure generates in blade region B_3 and B_4, then this distributes to the circumference of the casing back and finally to the upper corner of the casing in which it is the highest. The high static pressure region becomes low flow velocity. The low static pressure generates form the blade regions B_5, B_6, B_7 and B_1 to the fan exit. Thus, the flow velocity generates to the fan exit. Figure 4.14 (b) shows the contour line of the static pressure of the SC casing fan. The high static pressure occurs in the circumference of the casing near the wall. The low static pressure occurs in the duct region.

Figure 4.15 (a) and (b) shows the static pressure distribution of the RC and SC casing fan in the large flow rate ($\phi = 0.26$). Figure 4.15 (a), the high static pressure generates in the impeller outlet of the blade regions B_3, B_4 and B_5. This pressure distributes to the casing back, but the low static pressure distributes to the fan exit. Figure 4.15 (b) shows that the static pressure distribution from the impeller outflow to the casing for the SC casing fan. The high static pressure generates near the scrolling casing wall and the low static pressure occurs in the duct region.

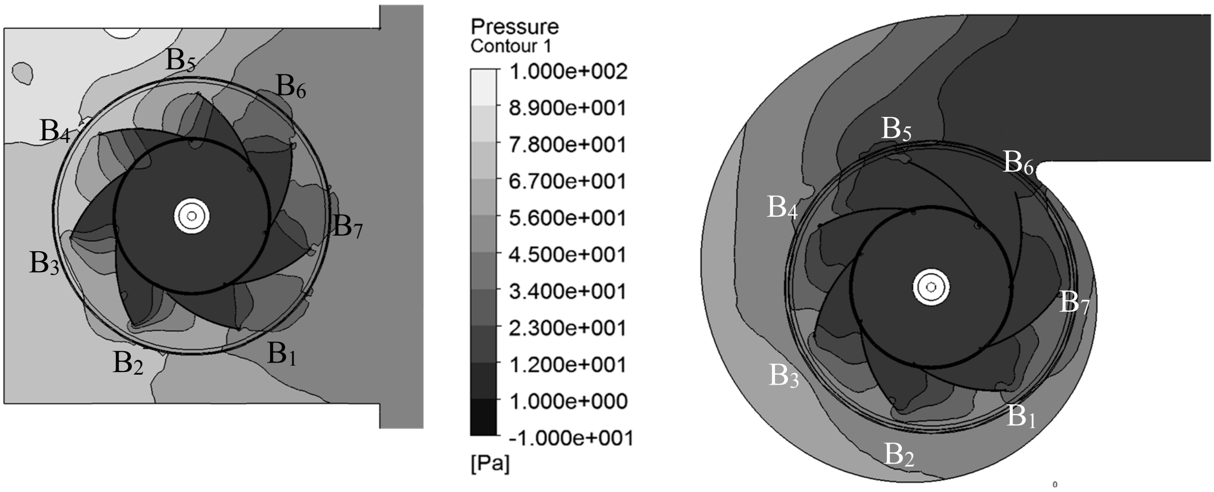

(a) RC casing fan

(b) SC casing fan

Fig. 4.15 Static pressure distributions ($\phi = 0.26$)

Figure 4.16 shows the static pressure distributions in the circumference of the impeller at the low flow coefficients ($\phi = 0.014$). Figure 4.16 (a) shows the static pressure distributions of the impeller for the RC casing. Figure 4.16 (b) shows the static pressure distributions of the impeller for the SC casing. In both cases, the non-uniform static pressure distributes in the circumferential of the impeller. The detail of the static pressure distributions of the impeller for RC casing fan show in Fig. 4.16 (a-1) to (a-4) and for SC casing fan shows in Fig. 4.16 (b-1) to (b-4). For the RC casing fan, the static pressure is high in the blade circumferences, B_5-B_6, B_6-B_7 shown in Fig. 4.16 (a-2) and B_1-B_7 shown in Fig. 4.16 (a-1), in which there is not flow out to the fan exit. For the SC casing fan, the static pressure is high in circumferential of impeller, B_3-B_4, B_4-B_5 shown in Fig. 4.16 (b-3) and B_4-B_5 shown in Fig.4.16 (b-2).

Figure 4.17 shows the static pressure distributions in the circumference of the impeller at the flow coefficients (ϕ = 0.121). Fig. 4.17 (a), (a-1) to (a-4) shows the static pressure

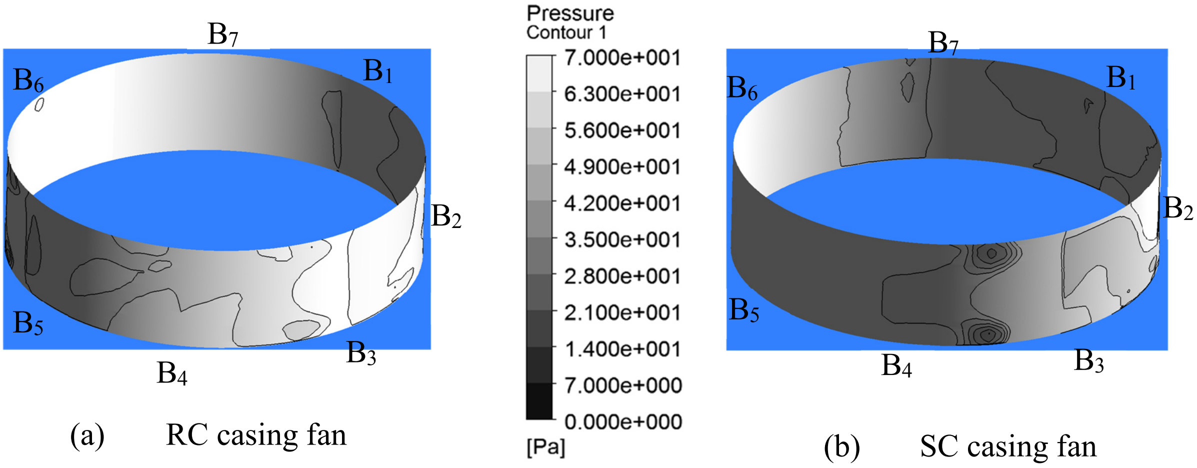

(a) RC casing fan

(b) SC casing fan

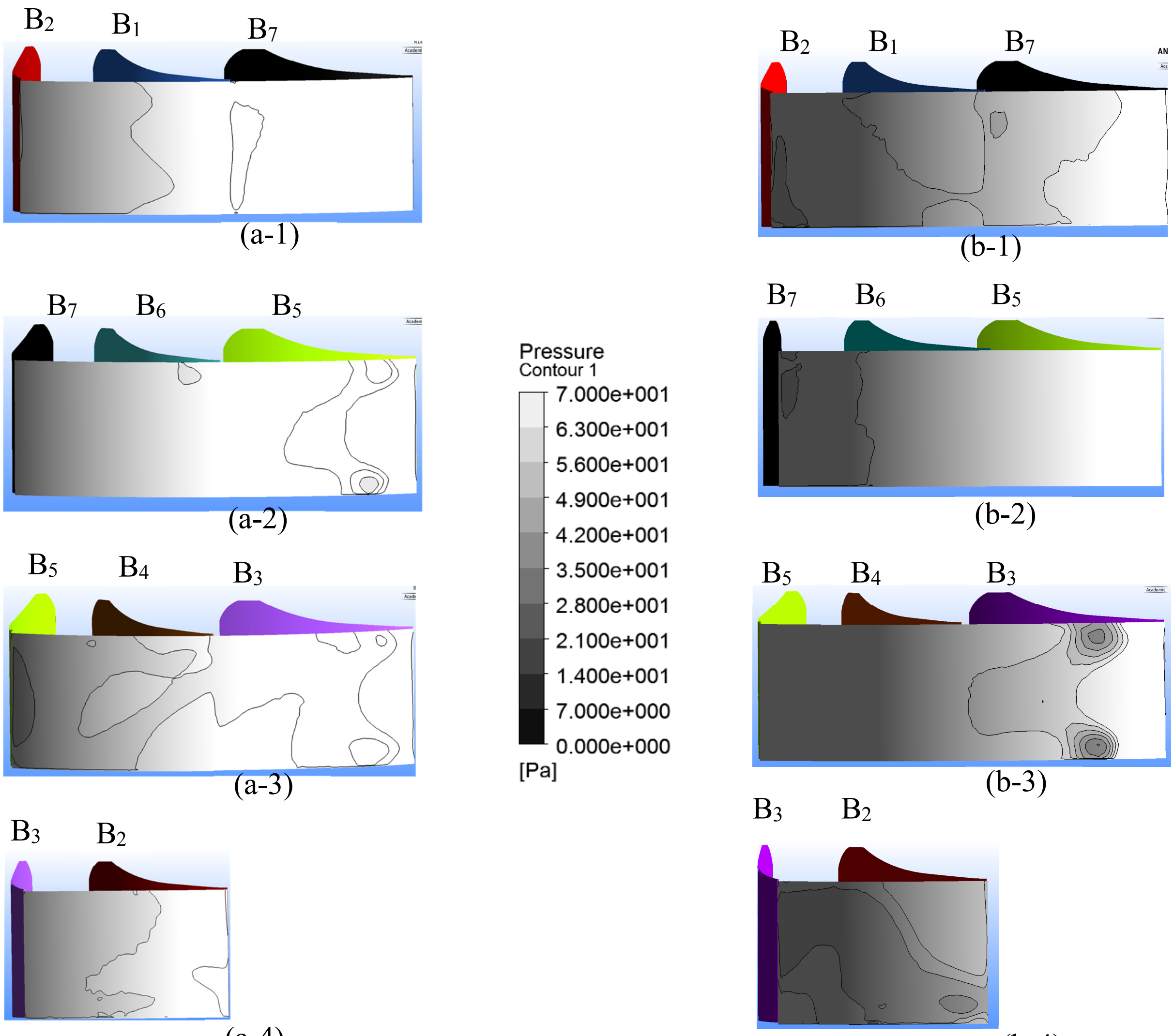

(a-1) (b-1)

(a-2) (b-2)

(a-3) (b-3)

(a-4) (b-4)

Fig. 4.16 Static pressure distributions (ϕ = 0.014)

distributions for the outflow of impeller for the RC casing fan. Fig. 4.17 (b), (b-1) to (b-4) shows the static pressure distributions for the outflow of impeller for the SC casing fan. Non-uniform pressure distribution occurs in both cases. For the RC casing fan, the high static pressure distributes in the circumference of the impeller in B_3-B_4 and B_4-B_5 shown in Fig. 4.17 (a-3) to the casing backward. For the SC casing fan, the high static pressure distributes in the circumference of the impeller, B_5-B_6 and B_6-B_7 shown in Fig. 4.17 (b-2), to the tongue region.

Figure 4.18 shows the static pressure distributions in the circumference of the impeller at the flow coefficients ($\phi = 0.187$). Fig. 4.18 (a), (a-1) to (a-4) shows the static pressure distributions for the outflow of impeller for the RC casing fan. Fig. 4.18 (b), (b-1) to (b-4) shows the static pressure distributions for the outflow of impeller for the SC casing fan. Non-uniform pressure distribution occurs in RC casing fan. For the RC casing fan, the high static pressure distributes in the circumference of the impeller in B_3-B_4 and B_4-B_5 shown in Fig. 4.18 (a-3) to the casing backward. For the SC casing fan, the uniform static pressure distributes in the circumference of the impeller to the casing except B_6-B_7. The high static pressure distributes in the circumference of the impeller, B_6-B_7 shown in Fig. 4.18 (b-2), to the tongue region.

Figure 4.19 shows the static pressure distributions in the circumference of the impeller at the flow coefficients ($\phi = 0.237$). Fig. 4.19 (a), (a-1) to (a-4) shows the static pressure distributions for the outflow of impeller for the RC casing fan. Fig. 4.19 (b), (b-1) to (b-4) shows the static pressure distributions for the outflow of impeller for the SC casing fan. Non-uniform pressure distribution occurs in the circumference of the impeller for both fans. For the RC casing fan, the high static pressure distributes in the circumference of the impeller in B_3-B_4 and B_4-B_5 shown in Fig. 4.19 (a-3) to the casing backward. For the SC casing fan, the non-uniform static pressure distributes in the circumference of the impeller to the casing. The lowest static pressure distributes in the circumference of the impeller, B_5-B_6 shown in Fig. 4.19 (b-2), to the tongue region in the duct.

Figure 4.20 shows the static pressure distributions in the circumference of the impeller at the flow coefficients ($\phi = 0.26$). Fig. 4.20 (a), (a-1) to (a-4) shows the static pressure distributions for the outflow of impeller for the RC casing fan. Fig. 4.19 (b), (b-1) to (b-4) shows the static pressure distributions for the outflow of impeller for the SC casing fan. Non-uniform pressure distribution occurs in the circumference of the impeller for both fans. For the RC casing fan, the high static pressure distributes in the circumference of the impeller in B_3-B_4 and B_4-B_5 shown in Fig. 4.20 (a-3) to the casing backward. For the SC casing fan, the non-uniform static pressure distributes in the circumference of the impeller to the casing. The lowest static pressure distributes in the circumference of the impeller; B_5-B_6, B_6-B_7 shown in Fig. 4.20 (b-2) and B_4-B_5 shown in Fig. 4.20 (b-3), to the tongue region in the duct.

The comparison of RC casing fan and SC casing fan (refer to Fig. 4.11 and 4.15) analyses with respect to static pressure rise from the impeller outflow to the fan exit. The value of static pressure rise of SC casing fan is high in the low flow rate ($\phi = 0.014$) and ($\phi = 0.121$), but it's value is low in the design flow rate ($\phi = 0.187$) and the high flow rate ($\phi = 0.237$) and ($\phi = 0.26$).

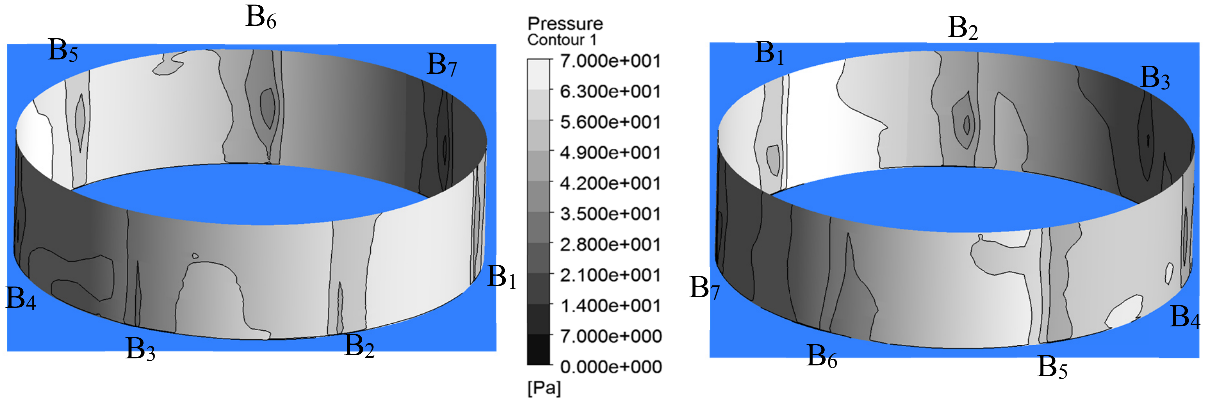

(a) RC casing fan (b) SC casing fan

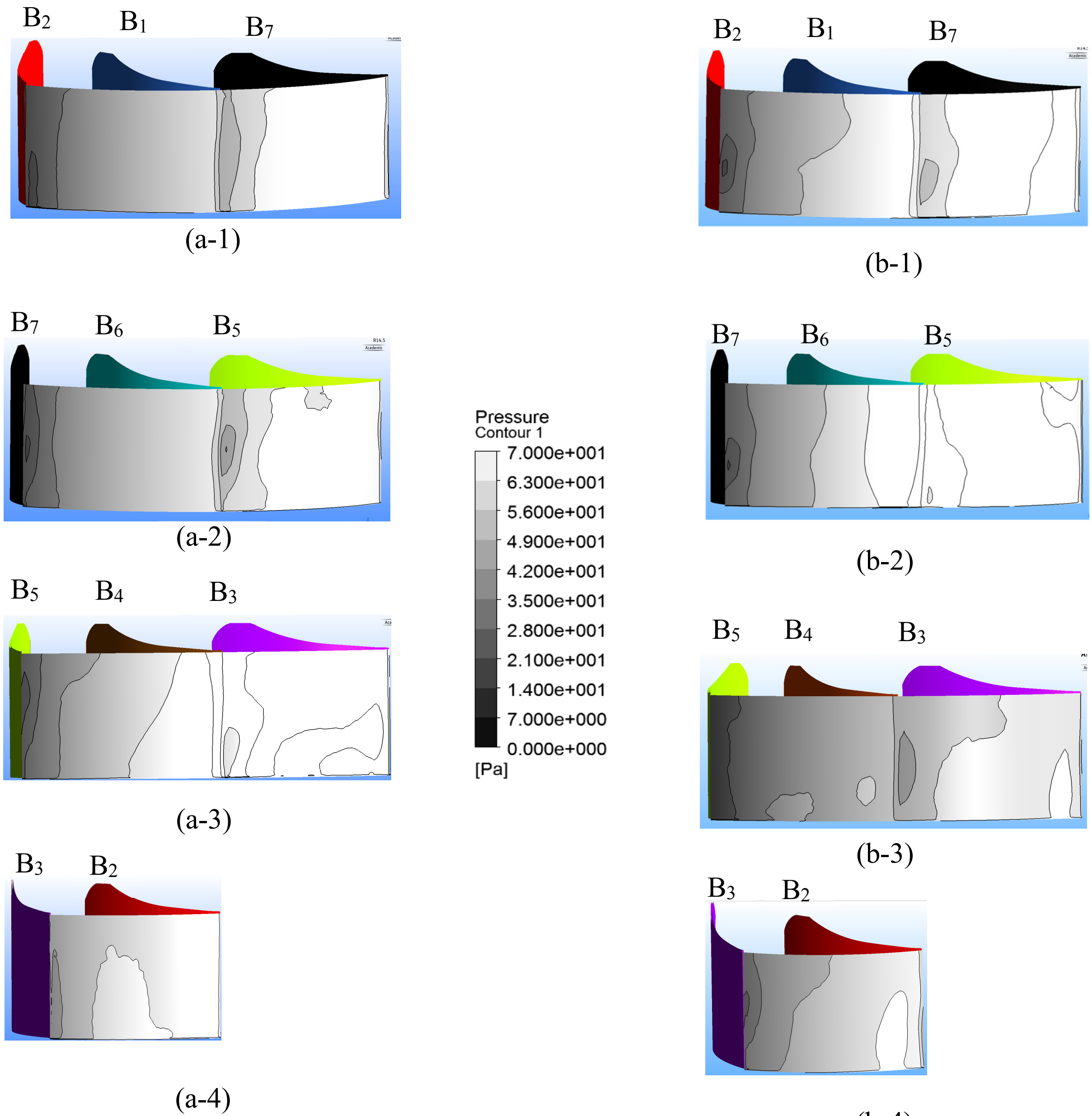

(a-1) (b-1)

(a-2) (b-2)

(a-3) (b-3)

(a-4) (b-4)

Fig. 4.17 Static pressure distributions ($\phi = 0.121$)

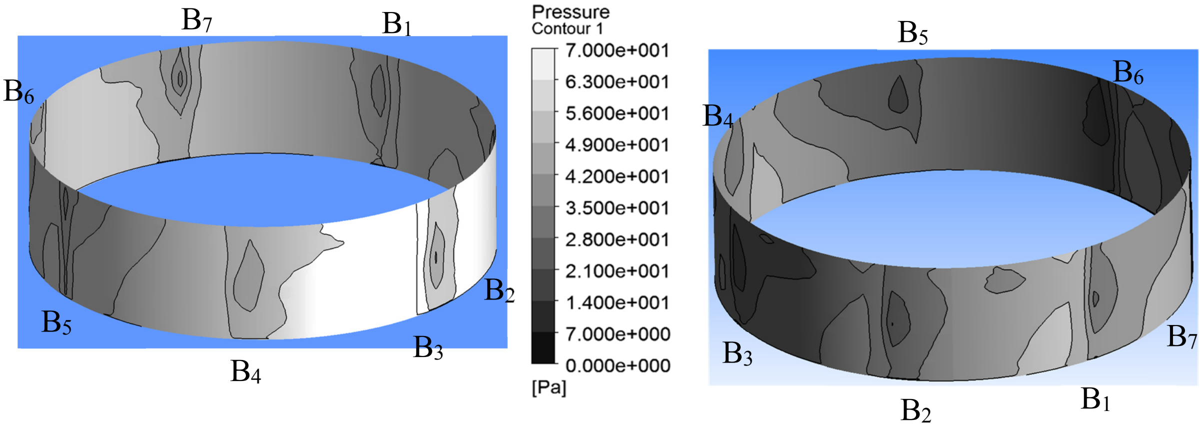

(a) RC casing fan

(b) SC casing fan

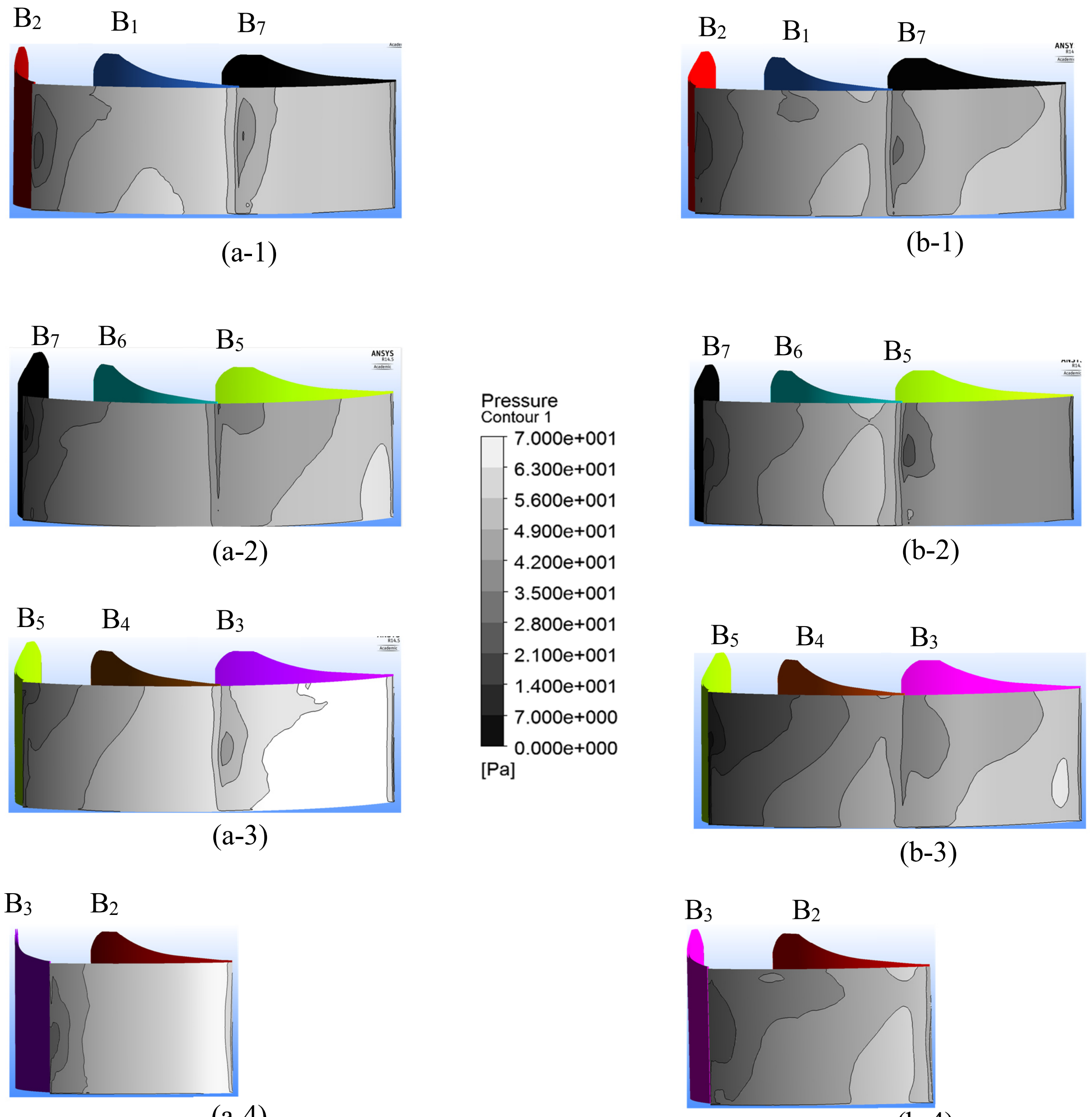

(a-1) (b-1)

(a-2) (b-2)

(a-3) (b-3)

(a-4) (b-4)

Fig. 4.18 Static pressure distributions ($\phi = 0.187$)

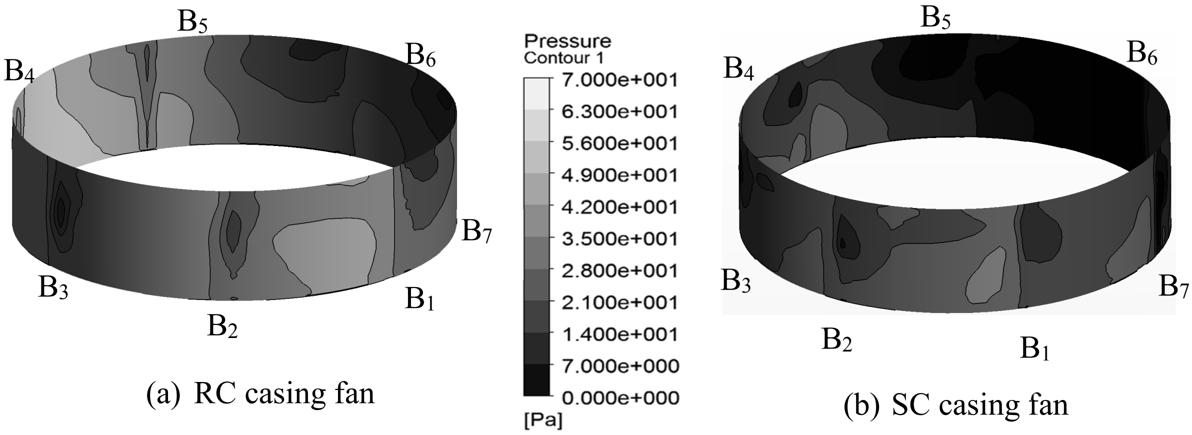

(a) RC casing fan

(b) SC casing fan

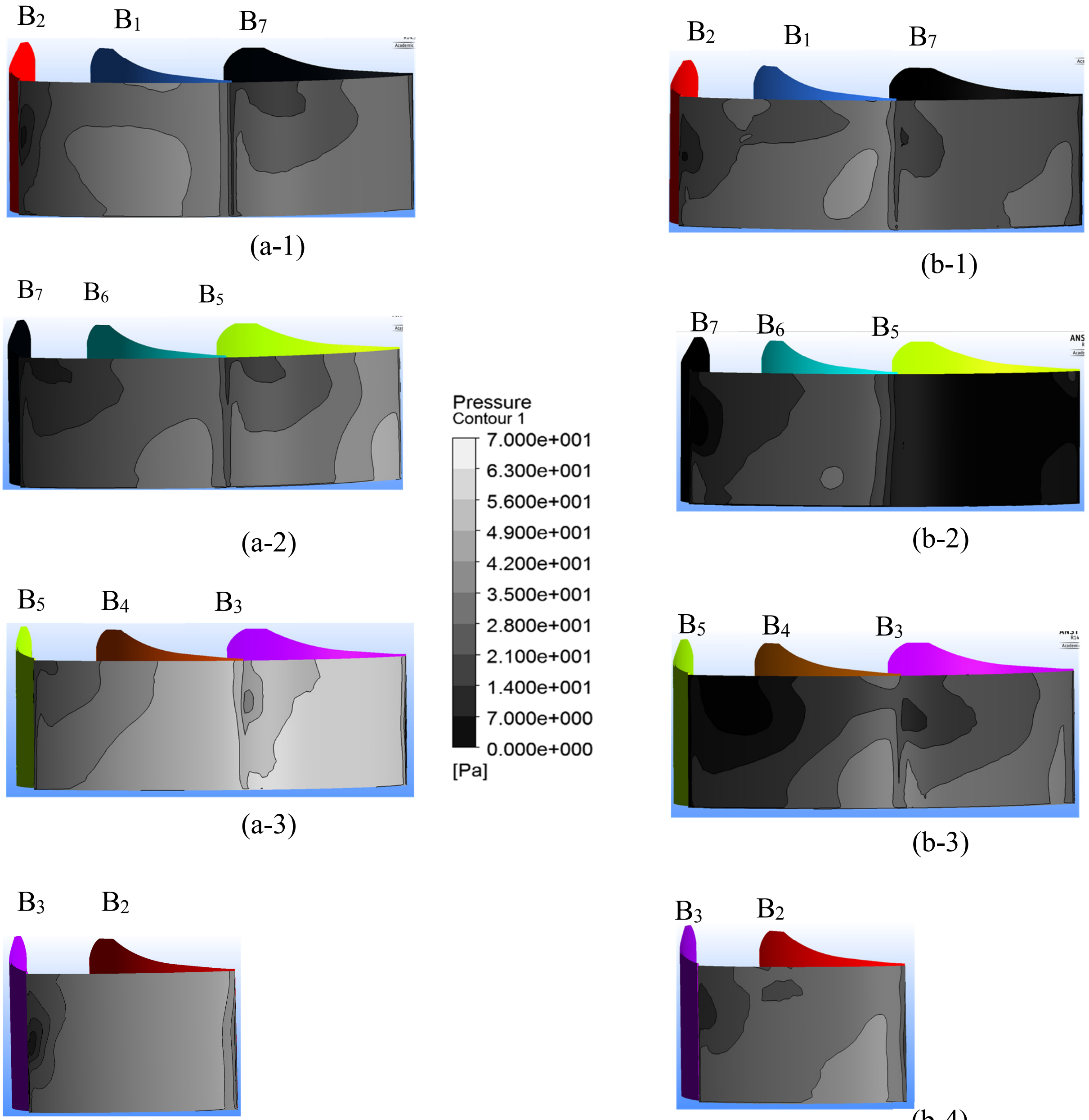

(a-1)

(b-1)

(a-2)

(b-2)

(a-3)

(b-3)

(a-4)

(b-4)

Fig. 4.19 Static pressure distributions (ϕ = 0.237)

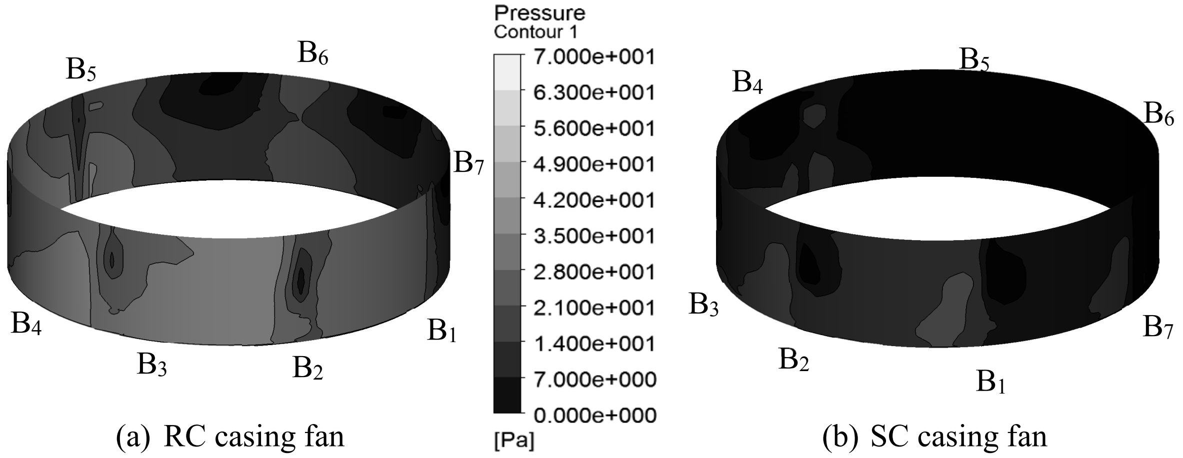

(a) RC casing fan (b) SC casing fan

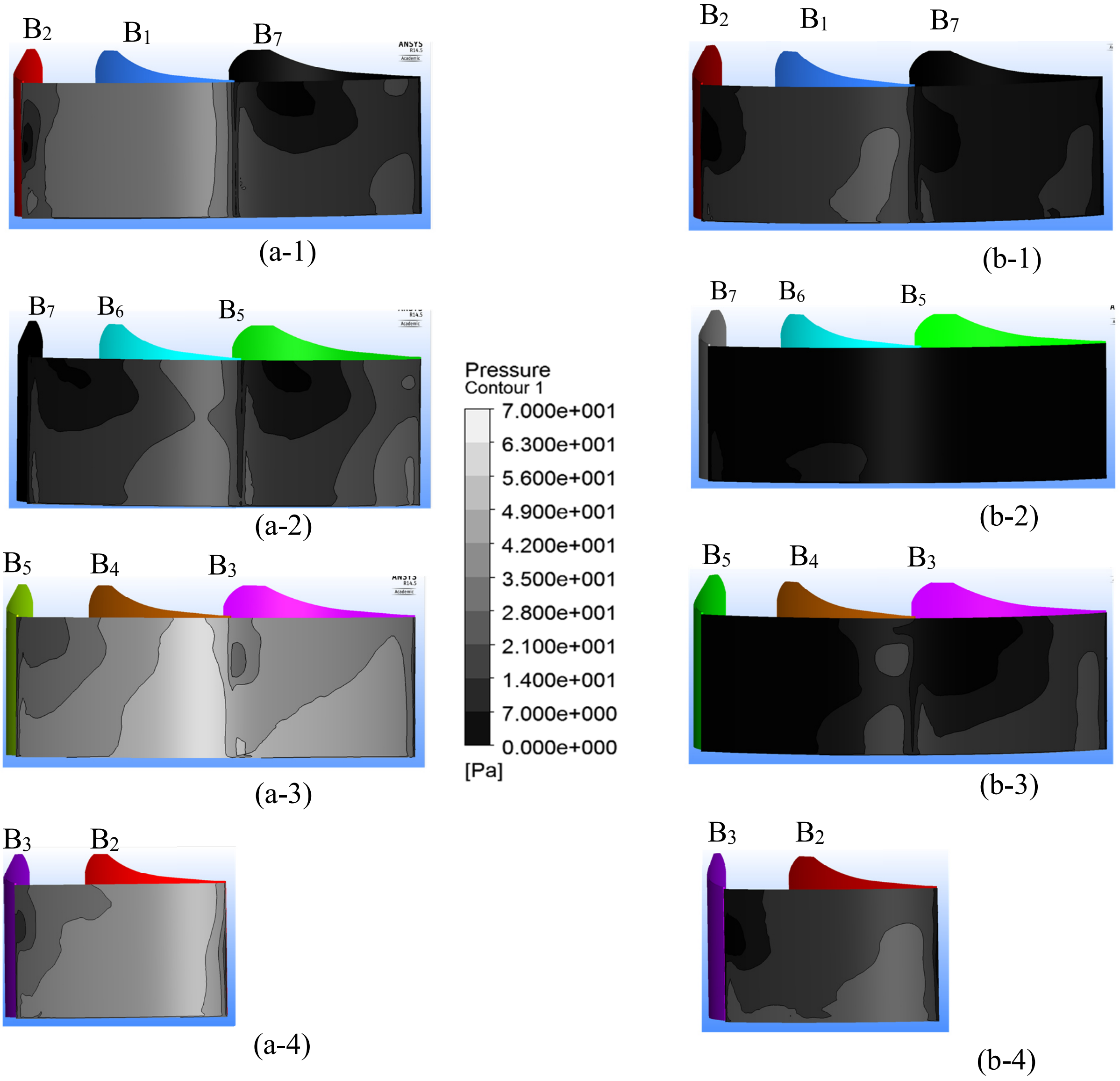

(a-1) (b-1) (a-2) (b-2) (a-3) (b-3) (a-4) (b-4)

Fig. 4.20 Static pressure distributions ($\phi = 0.26$)

4.2 Performance of the centrifugal fan

Fan performance is typically defined by the pressure and power requirement over a range of fan-generated airflow. Understanding this relationship is essential to designing and operating a fan system.

The centrifugal fan uses the centrifugal force generated from the rotation of impellers to increase the pressure. The air near the impeller is thrown-off from the impeller due to the centrifugal force and then moves into the casing. Then, the pressure increases at the impeller outflow, with the casing and fan exit. The fan performance is graphically depicted the basic fan characteristics data of flow coefficients (ϕ), the static pressure coefficients $\left(\psi_s\right)$ and the efficiency (η).

In this result, the performance curves show by comparing the performance characteristics, i.e., the variation of the pressure rise and the flow rate, of both fan types having difference casing (RC and SC casing). The CFX calculation result of fan performance is valid with the experimental one.

4.2.1 Performance curves

The flow rate coefficient (ϕ), static pressure coefficient $\left(\psi_s\right)$, total pressure coefficient $\left(\psi_t\right)$, the efficiency (η_s) and (η_t) in the figures are defined with the following equations.

The flow rate coefficient (ϕ):

$$\phi = \frac{60Q}{\pi^2 D^2 H N} \tag{4.1}$$

The static pressure coefficient $\left(\psi_s\right)$:

$$\psi_s = \frac{2P}{\rho \pi^2 D^2 (N/60)^2} \tag{4.2}$$

The efficiency (η):

$$\eta = \frac{PQ}{T\omega} \tag{4.3}$$

Where, D is the outlet diameter of the impeller [m].

H is exit blade height [m].

N is the rotational speed [rpm].

P is the static or total pressure rise [Pa].

Q is the air flow rate [m^3/s].

T is the impeller torque [N.m].

ρ_{air} is the density of air at $T = 25.4°C$, ($\rho_{air} = 1.1829$ kg/m^3).

ω is angular velocity of the impeller [rad/s].

Figure 4.21 shows performance curves of both (RC and SC casing) fans. Figure 4.21 (a) shows the comparison of performance curves of CFX calculation results with the experimental result. The RC casing fan performance is compared to SC casing fan performance based on the flow coefficients of $\phi = 0.014, \phi = 0.121, \phi = 0.187, \phi = 0.23$ and $\phi = 0.26$, in which $\phi = 0.187$ is design flow coefficient. In Fig. 4.21, the static pressure coefficient, (ψ_s) of SC

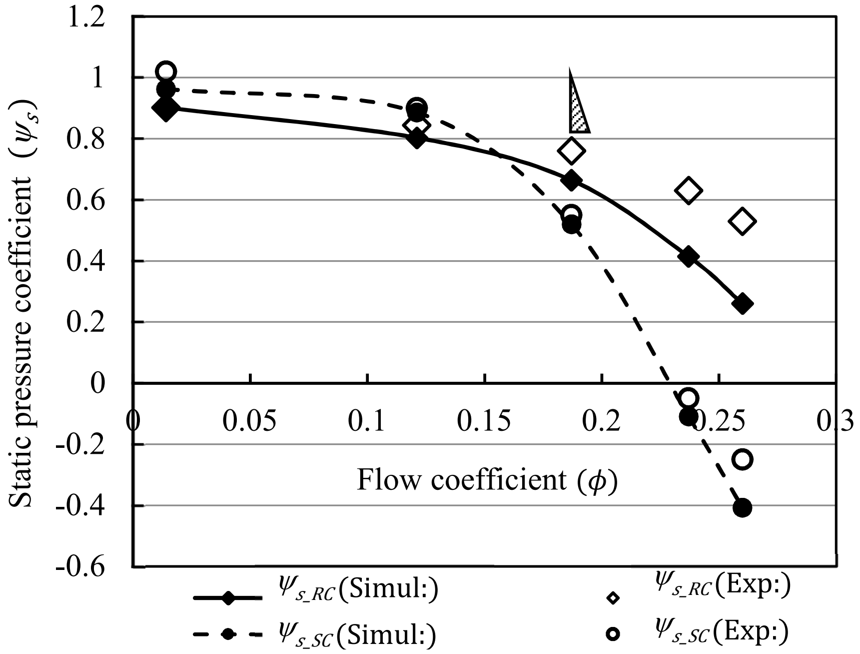

(a) Compared results of Experiment and Simulation

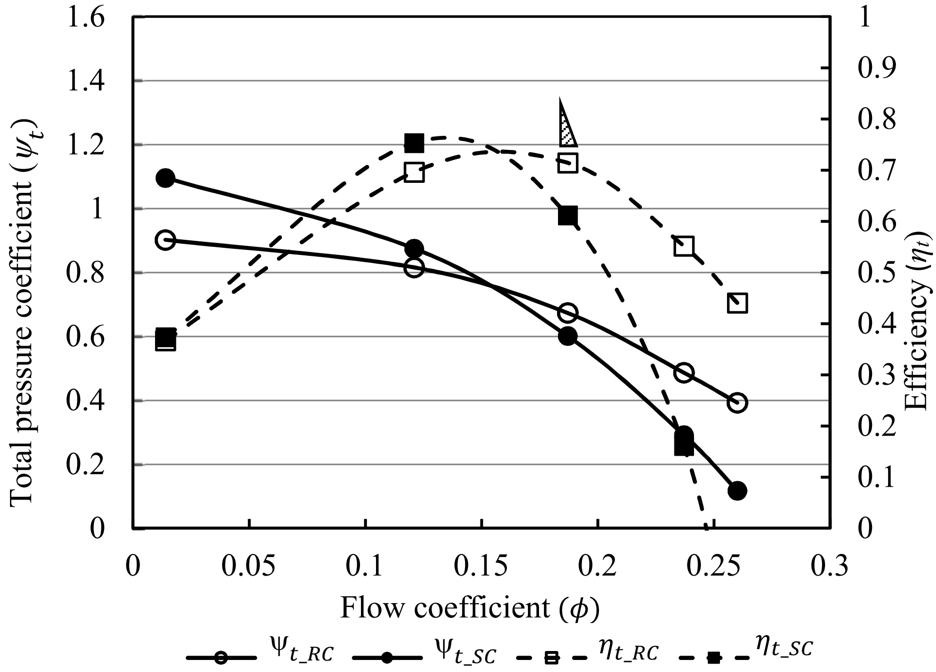

(b) Total pressure and Efficiency

Fig. 4.21 Fan performance

casing fan is higher than RC casing fan at the low flow coefficient, $\phi = 0.014$ and it becomes low with increasing flow rate. The static pressure coefficient, (ψ_s) of SC casing fan is higher than that of RC casing fan at the low flow coefficients $0.014 \leq \phi \leq 0.121$ and then these are gradually decreased before design flow coefficient. At design flow coefficient, $\phi = 0.187$and over it, pressure coefficients, (ψ_s) of RC casing fan are higher than that of SC casing fan. The simulation results are relatively agreeing with the experimental one.

Figure 4.21 (b) shows the total pressure coefficient, (ψ_t) and efficiency. The total pressure of SC casing fan is higher than that of RC casing fan at the low flow coefficients, $0.014 \leq \phi \leq 0.121$ and then these are gradually decrease until the design flow coefficient. At design flow coefficient, $\phi = 0.187$ and over it, pressure coefficients, (ψ_t) of RC casing fan are higher than that of SC casing fan.

The efficiency, (η_t) of SC casing fan are higher than that of RC casing fan at the low flow coefficients (0.014 ≤ϕ ≤ 0.121) and then these are slightly decrease of until the design flow rate. At the design flow coefficient, $\phi = 0.187$, the values of η_t are about 0.7 in RC casing fan and 0.61 at in SC casing fan. As mentioned in the chapter 1, the fan is necessary for the compactness and portable size, the high efficiency and good performance. The SC casing fan is not suitable for the large flow rate, this fan performance is decrease in large flow rate. On the other hand, in RC casing fan, maximum efficiency is obtained at large flow rate. RC casing fan can be operated in the wide range of flow rate.

Figure 4.22 shows the impeller performance. The pressure rise is averaged in circumference of the impeller outflow. The low flow coefficient, between $\phi = 0.014$ and $\phi = 0.121$, the pressure coefficients, (ψ_s) and (ψ_t) of the impeller with SC casing is slightly higher than that of the impeller with RC casing. At the design flow coefficient, ϕ=0.187 and over design point these pressure coefficients of the impeller with SC casing is significantly decreasing. But the variations of the pressure coefficient are slightly decreased with large flow coefficients.

The efficiencies (η_s) and (η_t) of the impeller with SC casing is almost the same that with RC casing in the low flow coefficient between (0.014 ≤ ϕ ≤ 0.121). They are significantly decreased in the impeller with SC casing at design flow coefficient ϕ = 0.187 and over it. If the impeller is used with the SC casing, the efficiency of the impeller is significantly varied at the large flow coefficient. But, the variation does not occur in the impeller with RC casing.

Thus, the maximum efficiency of static pressure, (η_s) of impeller with RC casing is about 0.55 at ϕ = 0.187. The maximum value, (η_s) of impeller with SC casing is about 0.54 at ϕ = 0.121. At design point, the higher efficiency (η_s) occurs in the impeller with RC casing. The maximum value of (η_t) is about 0.85 in both casings. But, the maximum values of $(\eta_t = 0.85)$ only occurs in the impeller with RC casing in the design flow rate. The efficiency of total pressure(η_t) is very large compared to the efficiency of static pressure (η_s).

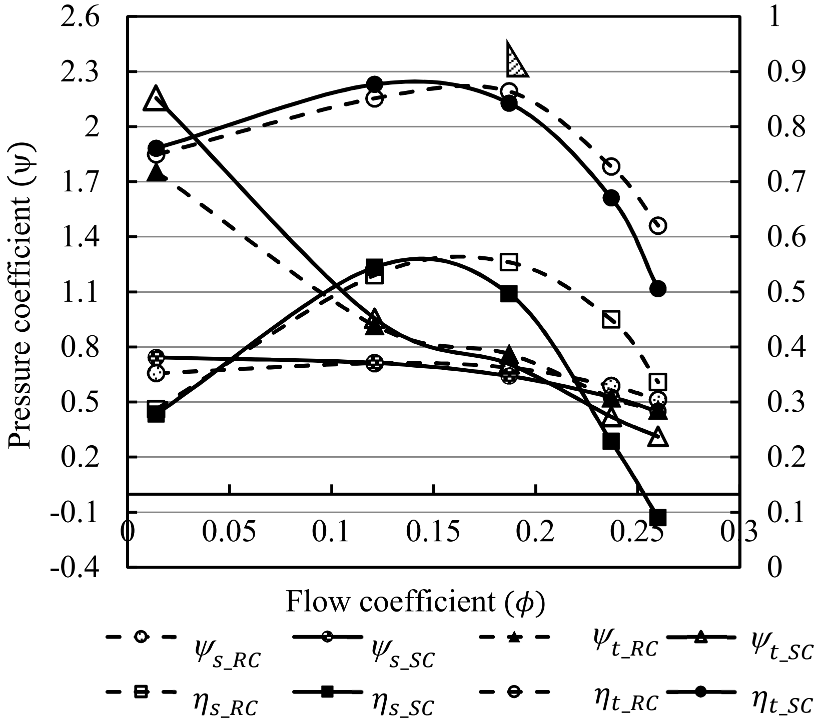

Fig. 4.22 Impeller performance

Figure 4.23 shows the performance of casings. The efficiency of casing (η_C) is defined by the following equation (4.4). In equation (4.4), (ΔP_{t_c}) is the pressure loss in the casing and (ΔP_{t_im}) is the pressure rise in the impeller.

$$\eta_c = 1 + \frac{\Delta P_{t\_c}}{\Delta P_{t\_im}} \tag{4.4}$$

The static pressure recovery ratio is the ratio of the static pressure rise to the dynamic pressure on the upstream side. The static pressure recovery rate is determined by equation (4.5). In equation (4.5), pressure recovery is the ratio of the differential pressure between the impeller outflow and the fan exit to the dynamic pressure.

$$\mathrm{C_p} = \frac{\Delta P_s}{\frac{1}{2}\rho v^2} \tag{4.5}$$

Figure 4.23 (b) shows the pressure recovery performance of the casing (RC casing and SC casing). High static pressure recovery occurs in the SC casing (scroll casing) with a low flow coefficient. At the low flow coefficient, the pressure recovery value is 0.6 in the SC casing (scroll casing) and 0.29 in the RC casing (rectangular casing). The pressure recovery in the SC casing is lower than that of a RC casing over the design flow coefficient. The pressure recovery value is 0.13 in the RC casing and -0.06 the SC casing.

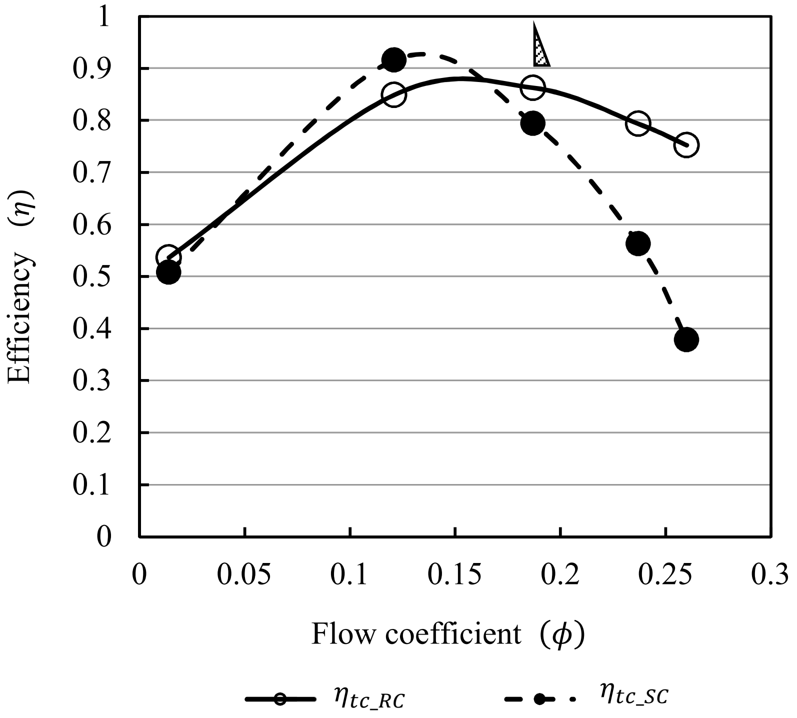

(a) Casing efficiency

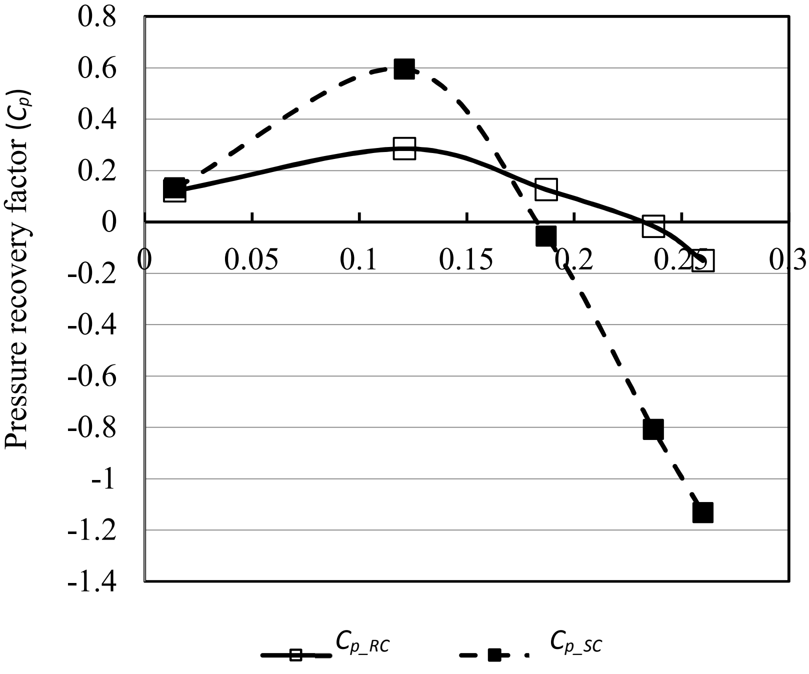

(b) Pressure recovery factor

Fig. 4.23 Casing performance

4.3 Energy loss

To evaluate the energy loss inside the casing for the design flow rate, the casing is divided into seven portions as shown in Fig. 4.24. In the SC casing, in Fig. 4.24 (a) the fan discharge portion assumes to be portion I, from which the casing circumference is divided into seven portions in the clock wise direction. In Fig. 4.24 (b), the SC casing is divided into seven areas clockwise from the tongue. Figure 4.25 (a) and (b) shows the RC casing and the SC casing fan of velocity streamline. In Fig. 4.25 (a) shows that the circulating flow dominants in parts II, III and V inside the RC casing. In Fig. 4.25 (b) shows that circulating flow occurs in parts II, III, IV, V, VI and VII of the SC casing.

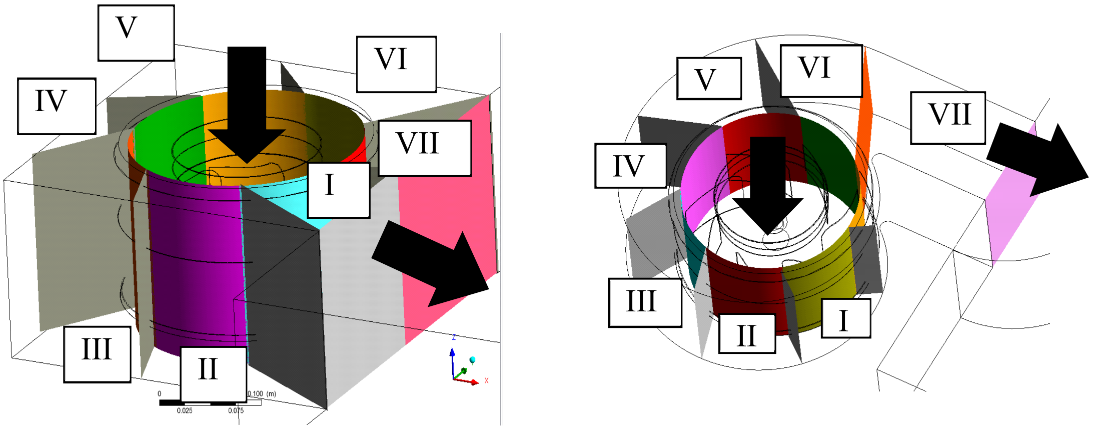

(a) Rectangular casing (b) Scroll casing

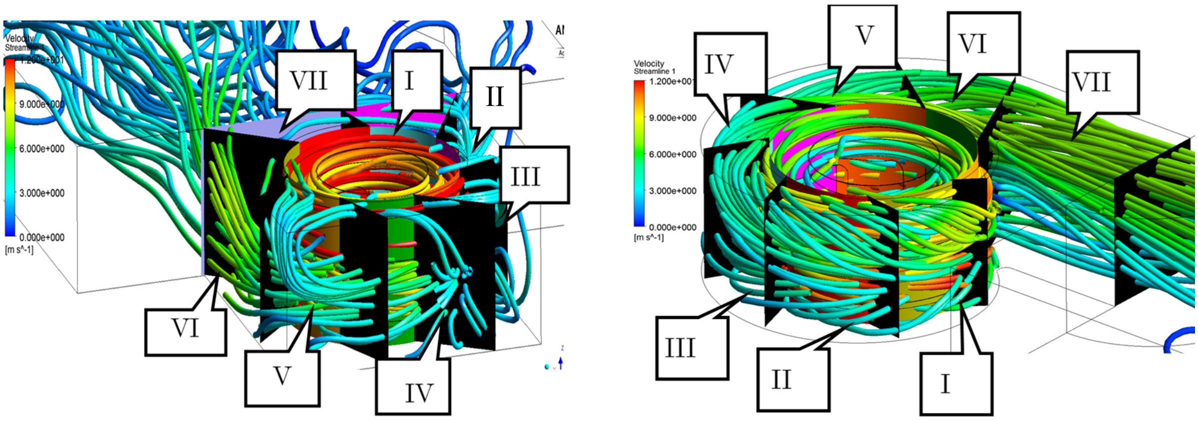

(c) Rear view of Rectangular casing (d) Front view Scroll casing

Fig. 4.24 Velocity streamline of simulation

The energy loss (Energy loss) in each portion of the casing calculates with equation (4.6). Where, E_p is the sum of the fluid energy entering and leaving the boundary of the named portion. Loss is calculated by summing of the energies (the positive energy entering to the boundaries and negative energy discharging from the boundaries) at the boundary of each portion.

$$E_p = \sum Q.P_t \tag{4.6}$$

Figure 4.25 plots the energy loss in term of blade load, $E_p/T\omega$. This figure shows the energy loss in each portion of the casing. The loss is dominant in parts II to V within the RC casing. The energy loss is very small in parts I and VI in the SC casing. Air is collected at the top of the shroud (Shroud). There is a wall friction loss inside the scroll casing. Wall friction losses occur in the scrolling region in parts II, III, IV and V and VII in the casing. The SC casing losses in parts I, III, IV, VI and VII are higher than the loss of the RC casing.

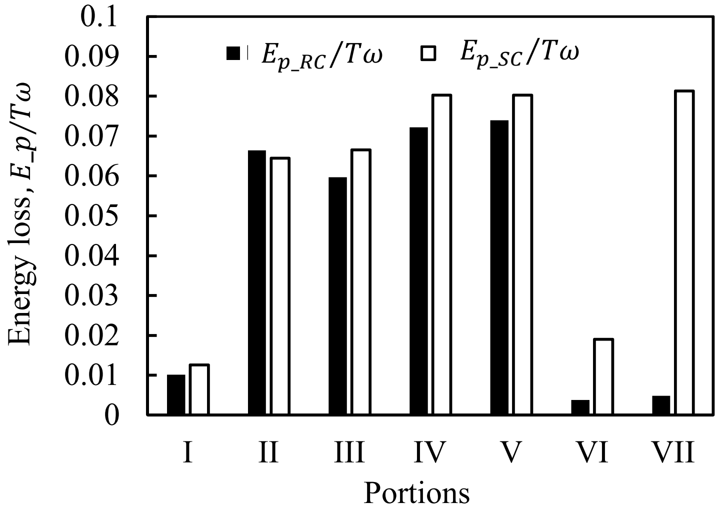

Fig. 4.25 Energy loss in casings

4.4 Summary

According to Fig. 4.1 (a) to 4.5 (a), for the RC casing fan, the flow separation occurs in all blade suction side in the low flow coefficient ($\phi = 0.014$), but the separation occurs only one blade, the blade B_2, in the large flow coefficient ($\phi = 0.26$). It means that increasing air flow rate induces the decrement of the flow separation in the internal flow. At the low flow rates, the air circulates in the casing circumference and it deposits backward of the casing, thus the casing flow doesn't fully continue to the fan exit. At the large flow rates ($\phi = 0.26$), the flow separation occurs in only blade B_2 and the casing flow generates to be going to the fan exit. In square casing (RC casing), the discharge flow from the impeller varies depending on the position in the circumference, and it generates a non-uniform flow.

According to Fig. 4.1 (b) to 4.5 (b), for the SC casing fan, the flow separation dominants on all blades suction side in the low flow ($\phi = 0.014$), that is why the casing (SC casing) flow can't continue to the fan exit. If the flow rate increases to the design flow rate ($\phi = 0.187$), the flow separation only occurs on the blades; B_1, B_6, B_7 and it may cause wake in the tongue region and the flow velocity reduces in the duct near it. For the large flow rate ($\phi = 0.26$), the flow separation occurs in leading edge of the blade pressure side. The uniform flow pattern generates from the impeller outflow to the circumferential location of the casing (SC casing) except the low flow rate, $\phi = 0.014$ and the high flow rate, $\phi = 0.26$.

According to Fig. 4.6 to Fig 4.10, the circumferential flow pattern to the casing is uniform for the SC casing in design flow rate ($\phi = 0.187$), but non-uniform for the RC casing. In all flow rate, the non-uniform flow pattern generates in the casing of the RC casing fan. The wake (jet flow or large circumferential flow) is generated in the circumferential of the casing backward. In the SC casing, for the high flow rate ($\phi = 0.121$), ($\phi = 0.237$) and ($\phi = 0.23$), although the uniform flow pattern occurs in the mid-span of the impeller, it occurs non-uniform in the circumferential of the impeller blade section B_4-B_5 and B_5-B_6. For the low flow rate ($\phi = 0.014$), the non-uniform flow pattern generates in the mid-span location and circumferential of the impeller to the casing.

According to Fig. 4.11 (a) to Fig. 4.15 (a), the static pressure distribution is still high at the upper corner of the casing for RC casing fan. Even through the flow rate changes from the low flow to the high flow rate, the static pressure is still high in the corner of the casing of RC casing fan. This means there is no flow velocity and most of the air collects in the upper corner. The static pressure distributions (refer to Fig. 4.11 (a) to 4.15 (a)) from the impeller outflow to the fan exit changes from high to low with respect to increasing the flow rate, i.e., the static pressure distribution is high in the fan exit cause of no flow velocity in the low flow rate ($\phi = 0.014$) but this pressure becomes low in the large flow rate ($\phi = 0.26$).

According to Fig. 4.11 (b) to Fig. 4.15 (b), the static pressure distribution in the scroll region near wall, tongue region and the duct is high at the low flow rate ($\phi = 0.014$). The static pressure is decreasing when the flow rate is increasing in the regions that mention above, i.e., the static pressure is high in the low flow rate ($\phi = 0.014$), but it is low in the large flow rate ($\phi = 0.26$).

For the RC casing fan, in the design flow rate and over it, the pressure is high at the back of the fan (refer to Fig. 4.13 (a) ~ Fig. 4.15 (a)), and it has a low distribution at the outlet but for the SC casing fan (refer to Fig. 4.13 (b) ~ Fig. 4.15 (b)), the impeller outlet pressure is almost the same as the fan discharge pressure. Cause of the above reason, the static pressure rises in RC casing is higher than these of SC casing at design flow rate and large flow rates. The casing pressure distribution obtains more uniform condition in the SC casing than in the case of a RC casing.

According to the figures: Fig. 4.16 to Fig. 4.20, although the flow rate change from low flow to high flow rate, the high static pressure still distributes in the circumferential of the impeller outflow to the casing backward for the RC casing. Although the high static pressure distributes from the impeller circumference to casing of the SC casing fan in the low flow rate ($\phi = 0.014$) and ($\phi = 0.121$), these pressure is significantly low down in the design flow and over design flow rate. But the static pressure distribution is not rapidly down in the casing of RC casing fan for design flow and overdesign flow rate. At the design flow rate, the static pressure distribution from the impeller outflow to the casing is about 3.3 Pa (P_{imp_out} =48.8 Pa and P_{fan_exit}= 52.15 Pa) for RC casing fan, but the value is about 1.5 Pa (P_{imp_out} =40.8 Pa and P_{fan_exit}= 39.4 Pa) for the SC casing fan. At the high flow rate ($\phi = 0.237$) and ($\phi = 0.26$), the negative static pressure distributes to the casing of the SC casing fan, but positive static pressure distributes to the casing of the RC casing fan.

Due to the performance of the impeller, the casing and the fan, RC casing (rectangular casing) fan gives more efficient flow characteristics at design flow rate. At the design flow rate, the type of casing has a little effect in impeller performance. The casing performance is a huge impact on fan performance.

The energy loss value in part II is 0.69 [W] in RC casing, 0.61 [W] in SC casing and RC casing loss is higher 3% than the loss in SC casing. The sum of losses of all portions, $E_p/T\omega$ is 0.4044[-] inside the SC casing, 0.2918[-] inside the RC casing. Thus, in the SC casing, the total loss is greater about 27.83% than RC casing.

According to the above discussions in Chapter 4, all the simulations were done with steady state. In this study, the value of flow rate ‘Q’ sets the same in RC casing fan and in SC casing fan. For example, for the steady simulation at the design flow rate, the value of flow rate ‘Q’ sets to 0.187. The flow rate set the same conditions in the simulation of RC casing and SC casing fan, and the resulting that the value of static pressure distribution in the RC casing is difference in the SC casing fan. The static pressure distribution from the impeller outlet to the exit of the fan (SC casing fan) is very lower than that of fan (RC casing fan) at the design flow rate and large flow rate (refers to Fig. 4.13 to 4.15 and Fig. 4.18 to 4.20). The efficiency (base on static and total pressure) of the RC casing fan is higher than that of SC casing fan in the design flow rate and large flow rate. The static pressure distribution of SC casing fan is significantly less in the design flow rate and it goes to the negative pressure in the large flow rate. This can cause to become low performance in the SC casing fan and the high the energy loss.

CHAPTER 5

Unsteady Flow Characteristics of Backward Impeller with Rectangular Casing

In this chapter, the performance and the internal flow pattern are analyzed for centrifugal fan with the steady and unsteady simulations. In this case, the only blade outlet angle of the impeller is changed, but the other geometries of the impeller don't change. For this study, the impeller attaches with the rectangular casing (RC casing). The circumferential flow pattern of this rectangular casing for each flow rate was discussed in Chapter 4 with steady simulation.

The flow characteristics of the centrifugal fans with different blade outlet angles are basically discussed on steady and unsteady simulations for the rectangular casing fan. The blade outlet angles of the impellers are 35° and 25° which are called impeller 'A' and impeller 'B' respectively. The turbofan design is usually made with the steady flow simulation. Then the flow out of the impellers are connected to the casing region only at the location that the impeller is in the simulation, even though the impeller is rotating and the flow characteristics are varied with the impeller location. When the flow separation is occurred in the impeller, the influence of the separation is restricted in the casing located at the impeller. But in the actual flow, the influence of separation of the impeller is spread wide to the circumferential location. In most cases, flow separation is responsible for lower performances and higher energy loss. Generally, the efficiency and loss calculations, however, revealed a significant discrepancy between the steady and unsteady simulation.

The objectives of this paper are to understand the influence of unsteady behavior in the impeller, the casing and the fan on performance, internal flow patterns. And it is discussed the responsibility for the above discrepancy, considering the physical aspects of the computations, steady Reynolds-averaged Navier-Stokes (RANS) and unsteady Reynolds-averaged Navier-Stokes (URANS).

5.1 Flow Characteristics

5.1.1 Flow pattern

The flow characteristics of simulation fans are discussed for each simulation conditions from the low flow rate $\phi = 0.014$ to the high flow rate $\phi = 0.22$. The flow characteristics, relative velocity and static pressure, are basically analyzed in the mid-span and circumferential location of the impeller.

Figure 5.1 to Fig. 5.4 shows the relative velocity contours of steady and unsteady flow patterns in the mid-span location. The steady and unsteady internal flow pattern of the impeller at the low flow coefficient, is shown in Fig. 5.1 (a) to (d). Figure 5.1 (a) shows the steady flow field of the fan with the impeller 'A' and Fig. 5.1 (b) shows the unsteady flow field of this fan. The steady flow pattern in the impeller 'A' is quite different in the unsteady flow pattern. The separation occurs in the suction side of the blades in both cases. The separation can lead to a distinct wake region. In Fig. 5.1 (b), the uniform flow pattern occurs in unsteady flow field in the fan with impeller ‘A’. In study flow field, the relative velocity is high in the outflow of the impeller ‘A’. The steady flow pattern in the circumference of casing is quite different in the unsteady flow pattern. The secondary flow of steady simulation is dominant and the wake occurs in the corner of the casing and fan exit.

Figure 5.1 (c) and (d) refer velocity contour of the impeller ‘B’ in the steady and unsteady flow field. The separation occurs in suction sides of all blades of the impeller ‘B’ for both steady and unsteady simulations. The internal flow pattern of the steady flow is almost the same in the unsteady flow pattern. The circumferential flow pattern of casing in steady is almost the same with it in the unsteady. The air deposits in the back ward of the casing circumference and fan exit.

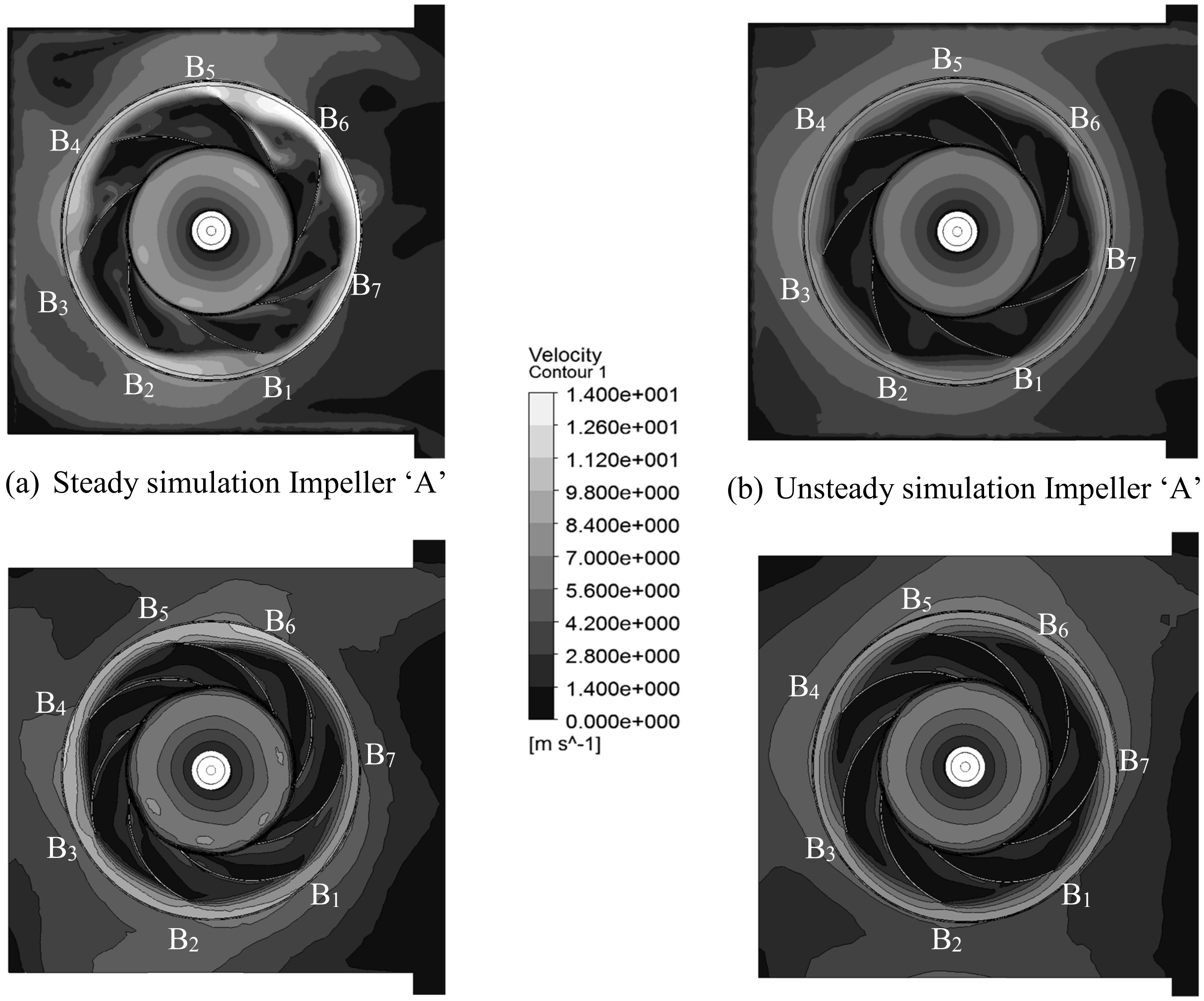

(a) Steady simulation Impeller ‘A’

(b) Unsteady simulation Impeller ‘A’

(c) Steady simulation Impeller ‘B’

(d) Unsteady simulation Impeller ‘B’

Fig. 5.1 Relative velocity distribution ($\phi = 0.014$)

The flow pattern of the centrifugal fan for the steady and unsteady simulation at the low flow rate ($\phi = 0.121$) is shown in Fig. 5.2 (a) to (d). The flow pattern of the impeller ‘A’ in the steady is quite different from the unsteady. In the steady simulation, the flow separation is dominant at suction sides of blades; B_1 through B_4 and then non-uniform flow pattern generates to the circumference of the casing. But in the unsteady simulation, flow field, the flow separations are occurring in suction sides of all blades and they generate almost the same pattern from inflow to the outflow of the impeller ‘A’. Then, the steady flow pattern in the casing is different from the unsteady. In steady flow field, the large amount of air is collected in fan exit.

In the flow rate ($\phi = 0.121$), the steady flow pattern of the centrifugal fan with the impeller ‘B’ is the same with the unsteady flow pattern as shown in Fig. 5.2 (c) and (d). The flow separation does not generate on the blade suction of the impeller ‘B’ for both steady and unsteady flow field. The inflow and outlet flow pattern of the steady simulation in the impeller ‘B’ are almost the same in unsteady simulation. The steady flow pattern of impeller ‘B’ in the casing is almost the same with the unsteady flow pattern.

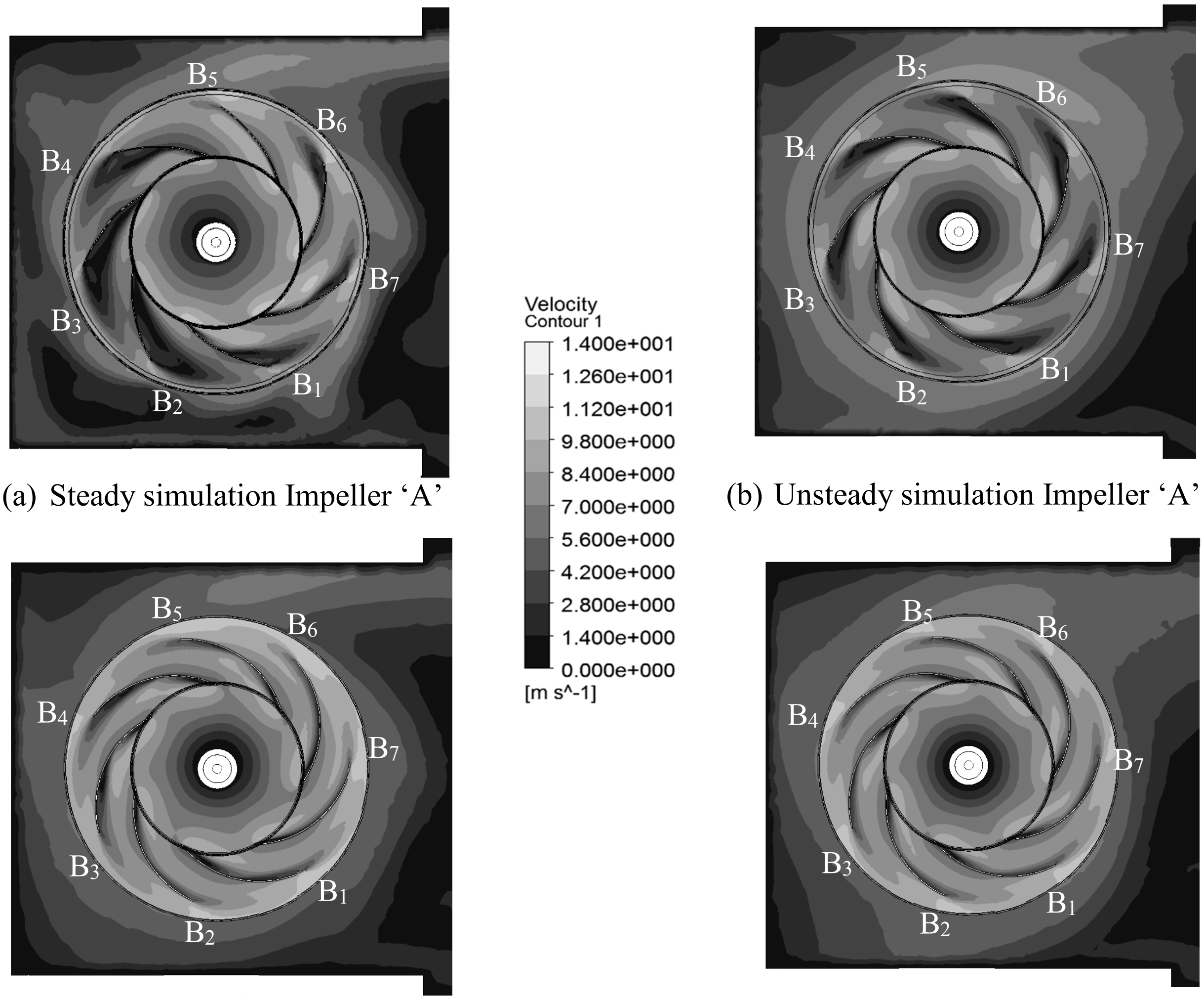

(a) Steady simulation Impeller ‘A’

(b) Unsteady simulation Impeller ‘A’

(c) Steady simulation Impeller ‘B’

(d) Unsteady simulation Impeller ‘B’

Fig. 5.2 Relative velocity distribution ($\phi = 0.121$)

Figure 5.3 shows the flow pattern in the design flow rate ($\phi = 0.187$). The flow patterns in steady and unsteady simulations inside the impeller is quite different at impeller ‘A’, but as the case of impeller ‘B’ is almost same. At the case of the impeller ‘A’ in Fig. 5.3 (a) and (b), the flow separation on the suction surface near the trailing edge of the blade is occurred at the back region, B$_2$, B$_3$, and B$_4$, that causes the large area of low velocity regions near the lower wall of the casing and the upper corner in steady simulation. The separation leads to a distinct wake region and higher static pressure. But in unsteady simulation, the separation of it is very small. The outflow from the casing near the upper wall is large in steady simulation. The uniform flow pattern occurs in unsteady flow field inside the impeller 'A', but non-uniform flow patterns occur in the steady flow field. The steady flow pattern in the circumferential direction of casing is quite different in the unsteady flow pattern. The secondary flow is dominant in the casing and the wake occurs in the corner of the casing and fan outlet in the steady flow.

Figure 5.3 (c) and (d) refers velocity contour of the impeller 'B' in steady and unsteady flow field. The separation occurs only at the leading edge of suction sides of blades inside the impeller 'B'. The steady flow pattern is little difference with the unsteady flow pattern inside impeller 'B'. In both steady and unsteady cases, the flow pattern is a little different in the circumferential direction of the casing.

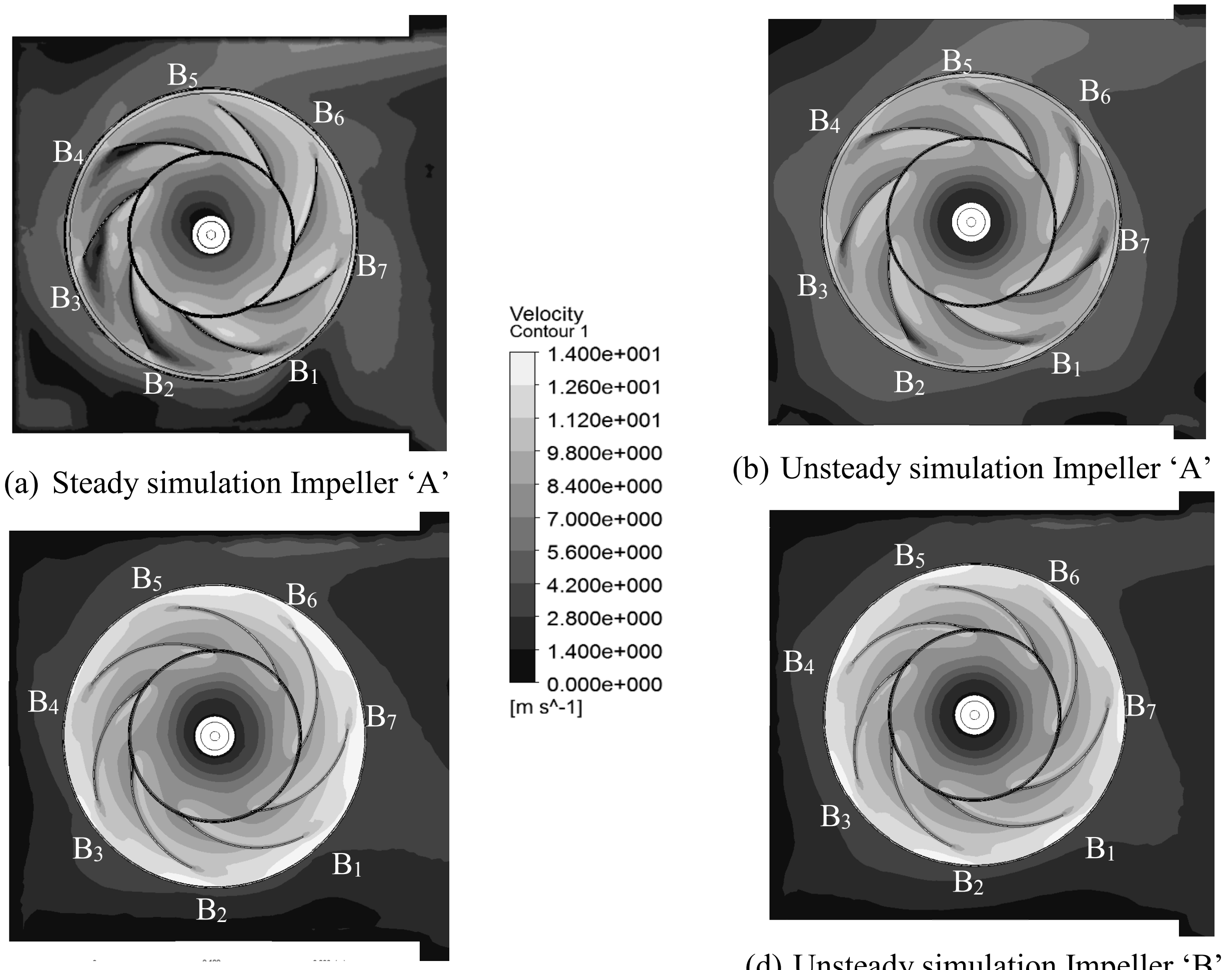

(a) Steady simulation Impeller 'A'

(b) Unsteady simulation Impeller 'A'

(c) Steady simulation Impeller 'B'

(d) Unsteady simulation Impeller 'B'

Fig. 5.3 Relative velocity distribution (ϕ = 0.187)

Figure 5.4 shows that the steady and unsteady of the flow pattern of centrifugal fan inside the impeller 'A' and 'B' at the large flow rate (ϕ = 0.22). Fig. 5.4 (a) shows that the non-uniform flow pattern occurs in steady flow field inside impeller 'A', but the uniform flow pattern occurs in the unsteady flow field. In steady flow, the separation on trailing edges of the suction side of blades; B_2, B_3, and B_4 cause the wake near the lower wall of the casing and the upper corner. In unsteady simulation, the separation is a little dominant on the suction of blades B_2 and B_7. The low velocity is a little dominant in the upper and the lower corner. In fan outflow, the unsteady flow behavior is better than steady, i.e., the outflow is rather uniform.

The unsteady flow pattern is almost the same in steady flow pattern inside the impeller 'B' shown in Fig. 5.4 (c) and (d). The uniform flow pattern is in both impellers. The flow separation doesn't occur in both steady and unsteady flow fields of the impeller 'B' and so the large flow velocity generates in the outflow of the impeller 'B' to the fan exit. The flow pattern in the casing is almost the same.

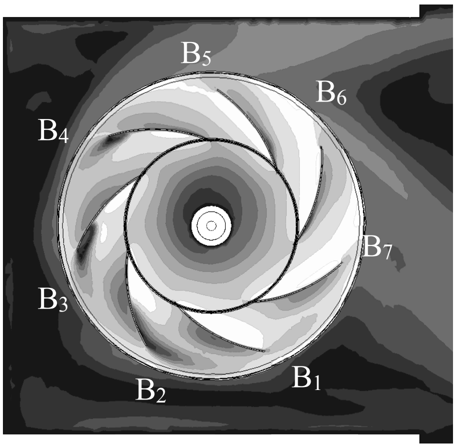

(a) Steady simulation Impeller 'A'

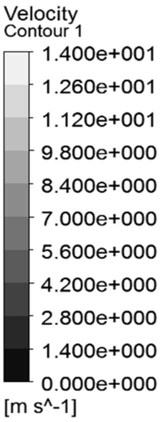

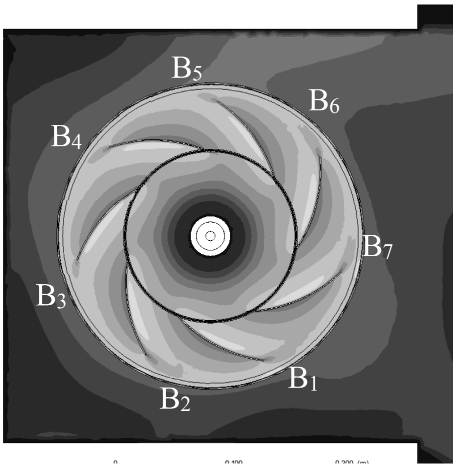

(b)Unsteady simulation Impeller 'A'

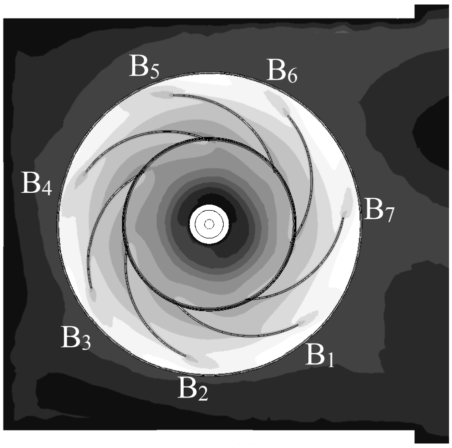

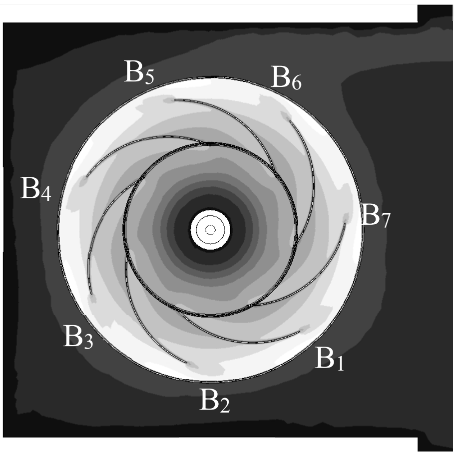

(c) Steady simulation Impeller 'B'

(d) Unsteady simulation Impeller 'B'

Fig. 5.4 Relative velocity distribution ($\phi = 0.22$)

Figure 5.5 through 5.8 shows the flow pattern at the outlet of the impeller with the impeller 'A'. The flow pattern in the steady simulation is compared with these of unsteady simulation. The figure (b) and (c) refers to the steady and unsteady flow pattern. The figure (b-1) through (b-4) and (c-1) through (c-4) show the relative velocity contour at each blade outlet section. In Fig. 5.5 (b) and (c) shows the steady and unsteady flow pattern of the impeller 'A' in the low flow rate ($\phi = 0.014$). The non-uniform flow pattern occurs in the steady but uniform flow pattern occurs in the unsteady. The non-uniform flow pattern dominants in high velocity region and the low velocity region; section B_4 to B_5 in Fig. 5.5 (b-3) and section B_5-B_6 shown in Fig. 5.5 (b-2).

In Fig. 5.6 (b) and (c) shows the steady and unsteady flow pattern of the impeller 'A' in the flow rate ($\phi = 0.121$). The non-uniform flow pattern occurs in the circumferential of the impeller in the steady but uniform flow pattern occurs in the unsteady. The non-uniform flow pattern dominants in the blade regions; B_1- B_2 in Fig. 5.6 (b-1) and B_4-B_5 shown in Fig. 5.6 (b-3).

In Fig. 5.7 (b) and (c) shows the steady and unsteady flow pattern of the impeller 'A' in the design flow rate ($\phi = 0.187$). The non-uniform flow pattern occurs in the steady but uniform flow pattern occurs in the unsteady. The non-uniform flow pattern dominants in the blade regions; B_1-B_7 in Fig. 5.7 (b-1), B_5-B_6 in Fig. 5.7 (b-1) and B_4-B_5 shown in Fig. 5.7 (b-3).

In Fig. 5.8 (b) and (c) shows the steady and unsteady flow pattern of the impeller 'A' in the large flow rate ($\phi = 0.22$). The non-uniform flow pattern occurs in the steady but uniform flow pattern occurs in the unsteady. The non-uniform flow pattern dominants in the blade regions; B_5-B_6 in Fig. 5.8 (b-1) and B_4-B_5 shown in Fig. 5.8 (b-3).

Figure 5.9 through 5.12 shows that the circumferential outflow pattern at the outlet of the impeller 'B'. The flow pattern in the steady simulation is compared with these of unsteady simulation. The figure (b) and (c) refers to the steady and unsteady flow pattern. The figure (b-1) through (b-4) and (c-1) through (c-4) show the relative velocity contour at the blade outlet sections.

In Fig. 5.9 (b) and (c) shows the steady and unsteady flow pattern of the impeller 'B' in the low flow rate ($\phi = 0.014$). The steady flow pattern is different from the unsteady in the circumferential of the impeller. The non-uniform flow pattern dominants in blade circumference; section B_2-B_1 and B_1-B_7 shown in Fig. 5.9 (b-1).

In Fig. 5.10 (b) and (c) shows the steady and unsteady flow pattern of the impeller 'B' in the flow rate ($\phi = 0.121$). The uniform flow pattern occurs in the steady and the unsteady simulations. The high velocity dominants in the blade regions; B_5- B_6 in Fig. 5.10 (b-2) and B_4-B_5 shown in Fig. 5.10 (b-3).

In Fig. 5.11 (b) and (c) shows the steady and unsteady flow pattern of the impeller 'B' in the design flow rate ($\phi = 0.187$). The uniform flow pattern occurs in the circumferential of the impeller in the unsteady simulation. The uniform flow pattern dominants in each blade regions of the unsteady simulations. The separation occurs only at the leading edge of suction sides of blades inside the impeller 'B'. The steady flow pattern is little difference with the unsteady flow pattern inside impeller 'B'. In both steady and unsteady cases, the flow pattern is a little different in the circumferential direction of the casing.

In Fig. 5.12 (b) and (c) shows the steady and unsteady flow pattern of the impeller 'B' in the large flow rate ($\phi = 0.22$). The steady flow pattern is little difference with the unsteady flow pattern inside impeller 'B'. In both steady and unsteady cases, the flow pattern is a little different in the circumferential direction of the casing.

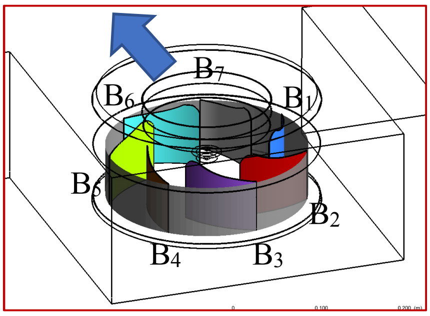

(a) Circumferential outflow location (Impeller ‘A’)

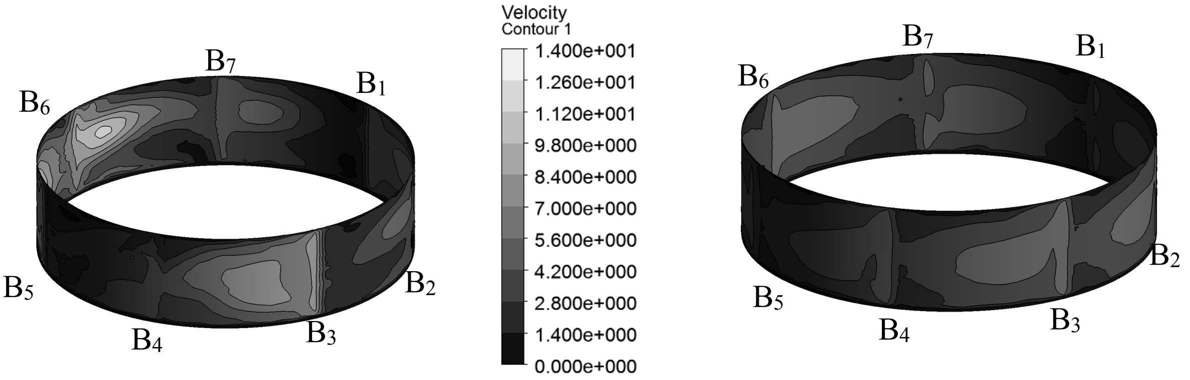

(b) Steady simulation Impeller ‘A’ (c) Steady simulation Impeller ‘A’

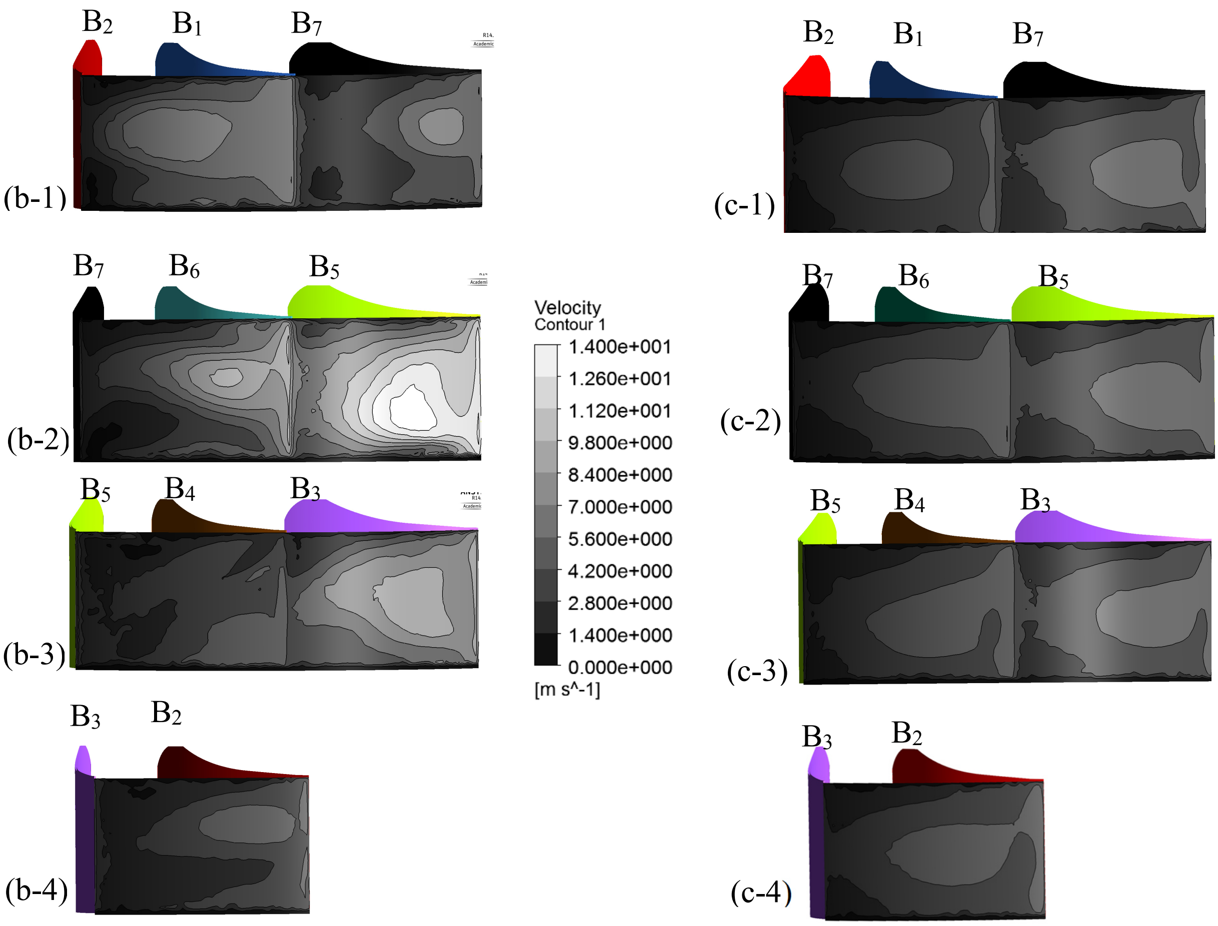

Fig. 5.5 Circumferential outflow pattern ($\phi = 0.014$)

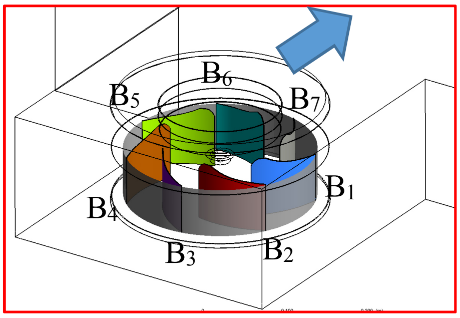

(a) Circumferential outflow location (Impeller ‘A’)

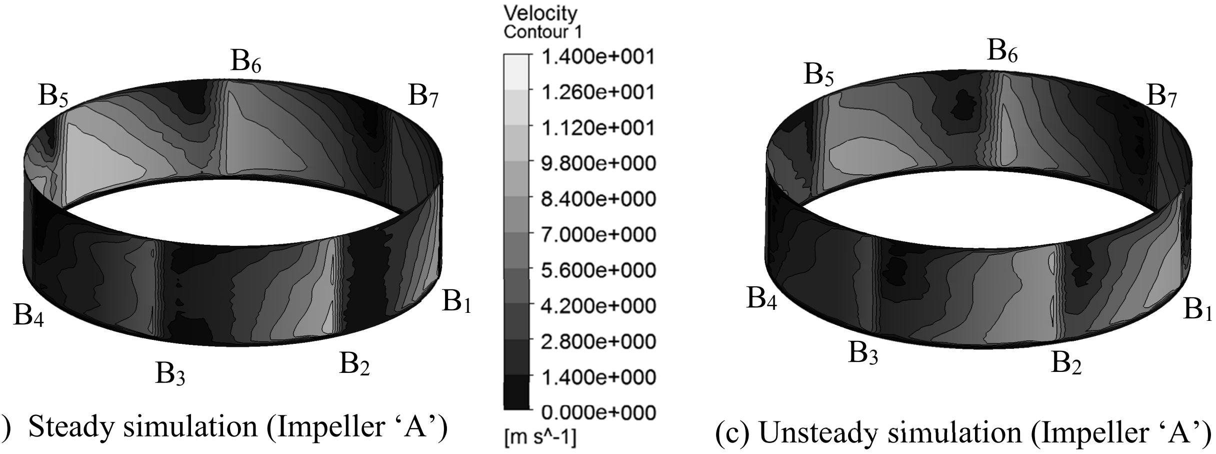

(b) Steady simulation (Impeller ‘A’)

(c) Unsteady simulation (Impeller ‘A’)

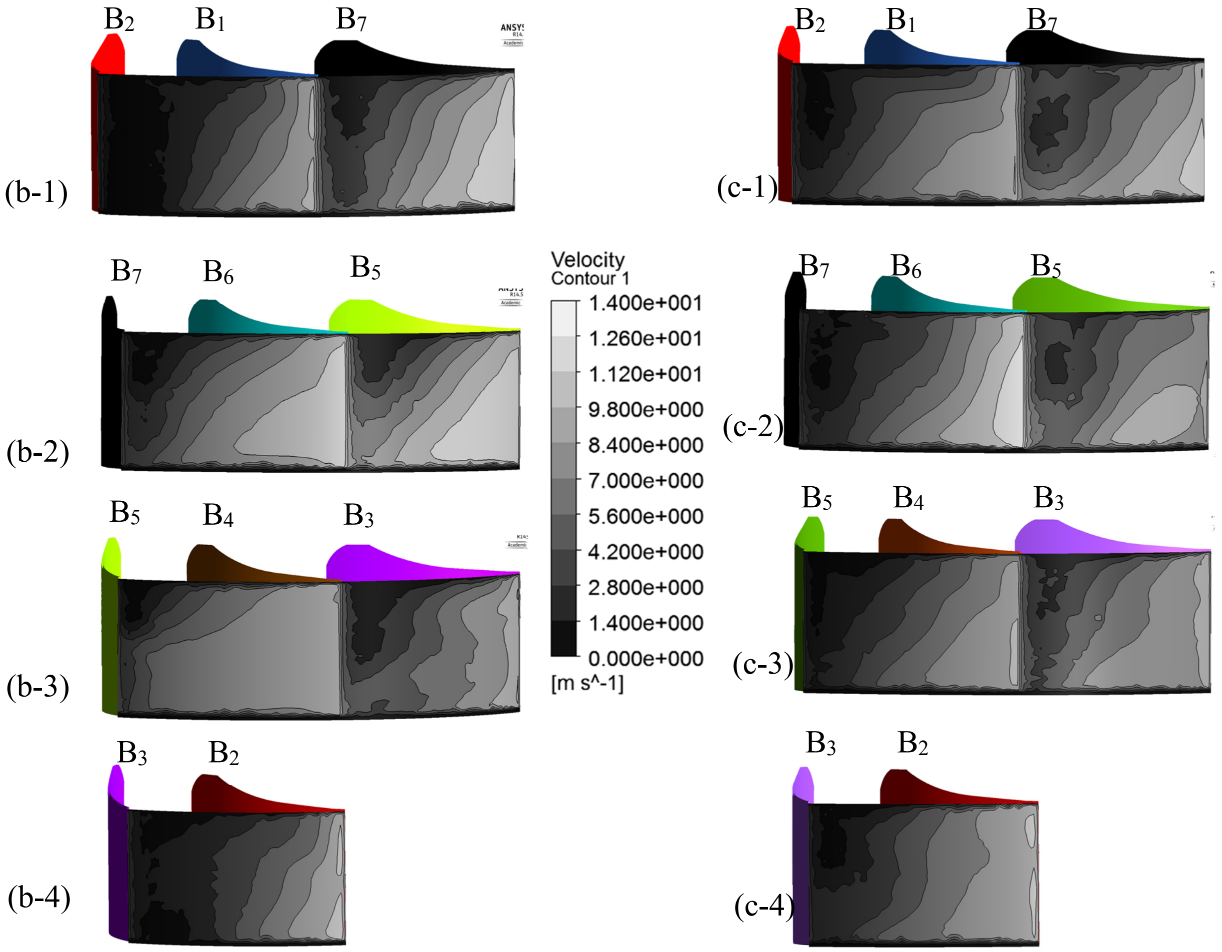

Fig. 5.6 Circumferential outflow pattern (ϕ = 0.121)

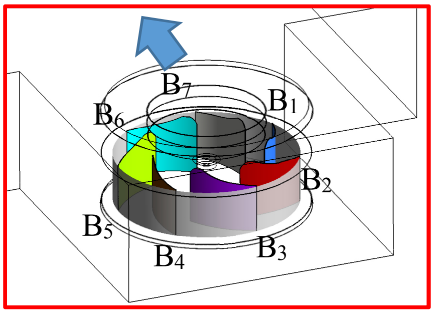

(a) Circumferential outflow location (Impeller ‘A’)

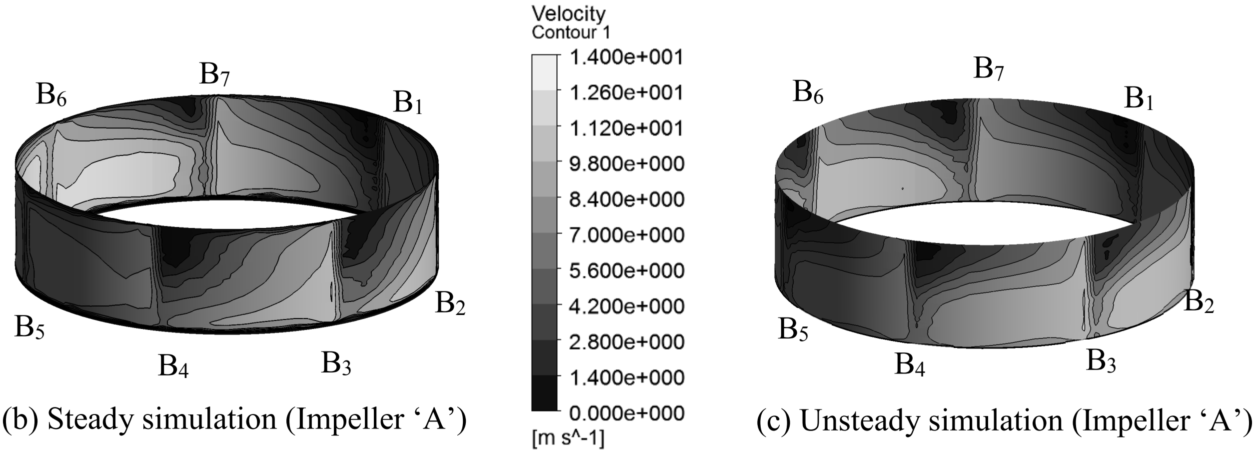

(b) Steady simulation (Impeller ‘A’)

(c) Unsteady simulation (Impeller ‘A’)

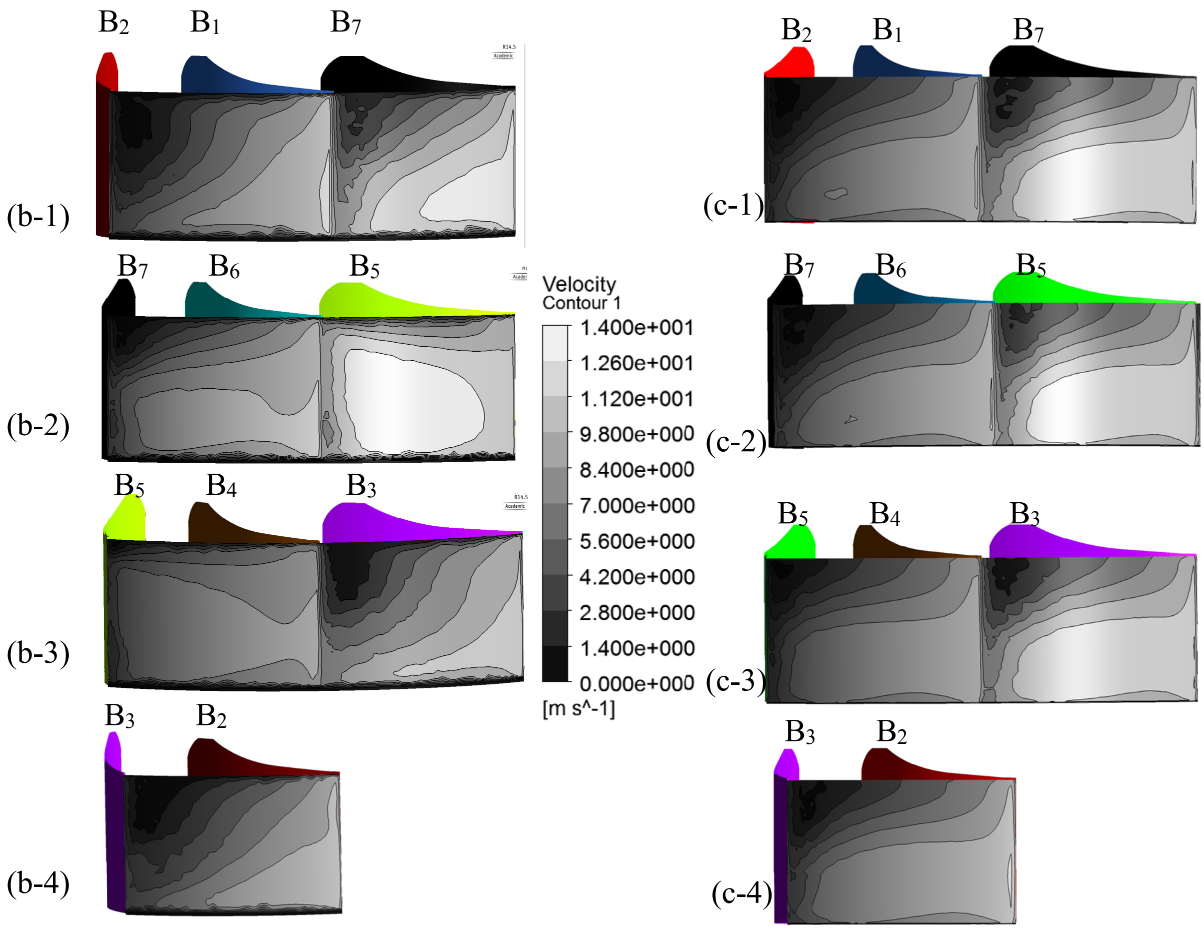

Fig. 5.7 Circumferential outflow pattern ($\phi = 0.187$)

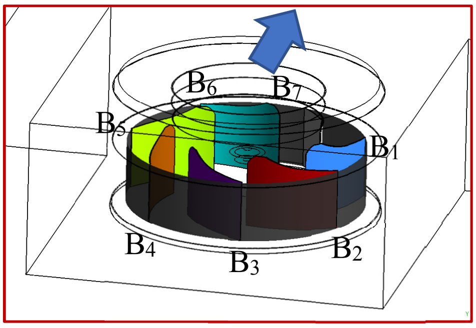

(a) Circumferential outflow location (Impeller ‘A’)

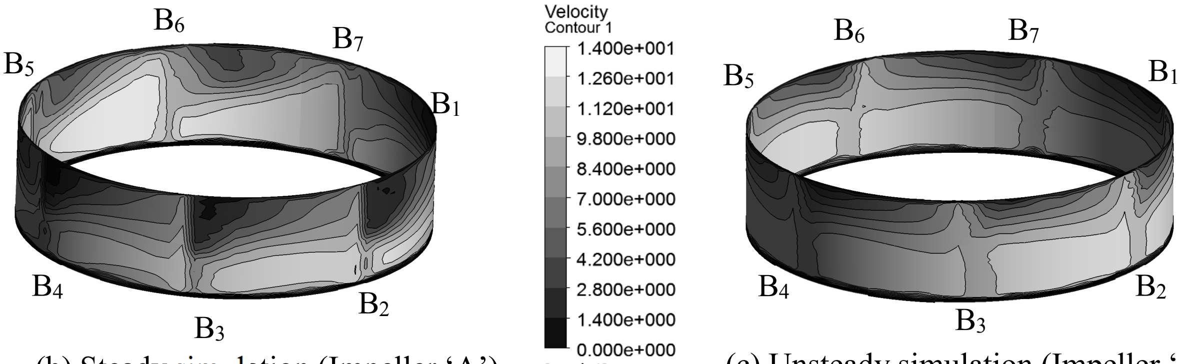

(b) Steady simulation (Impeller ‘A’)

(c) Unsteady simulation (Impeller ‘A’)

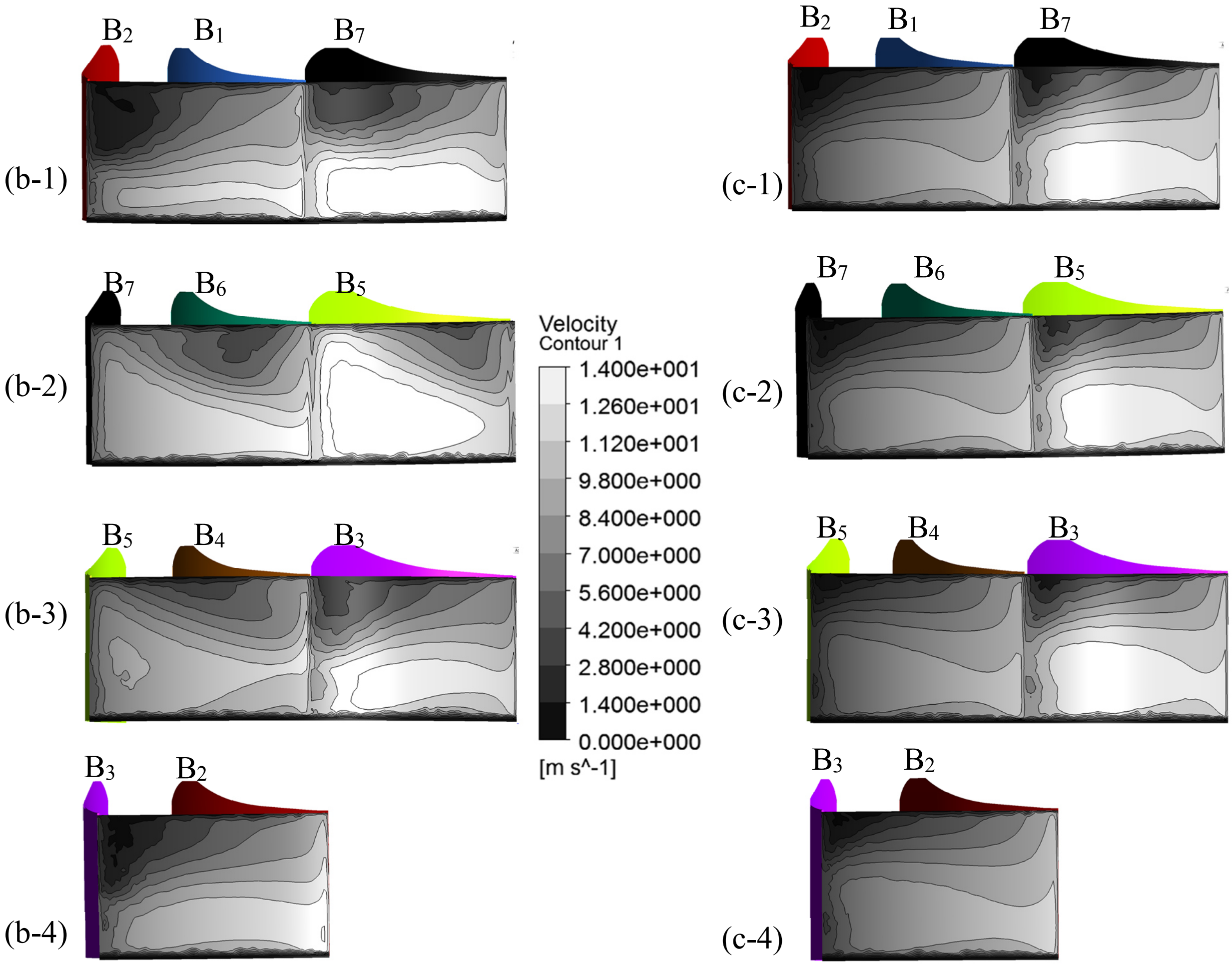

Fig. 5.8 Circumferential outflow pattern ($\phi = 0.22$)

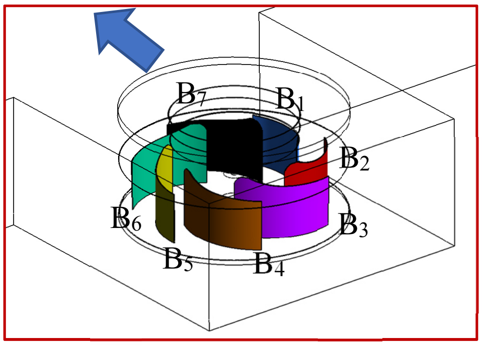

(a) Circumferential outflow location (Impeller 'B')

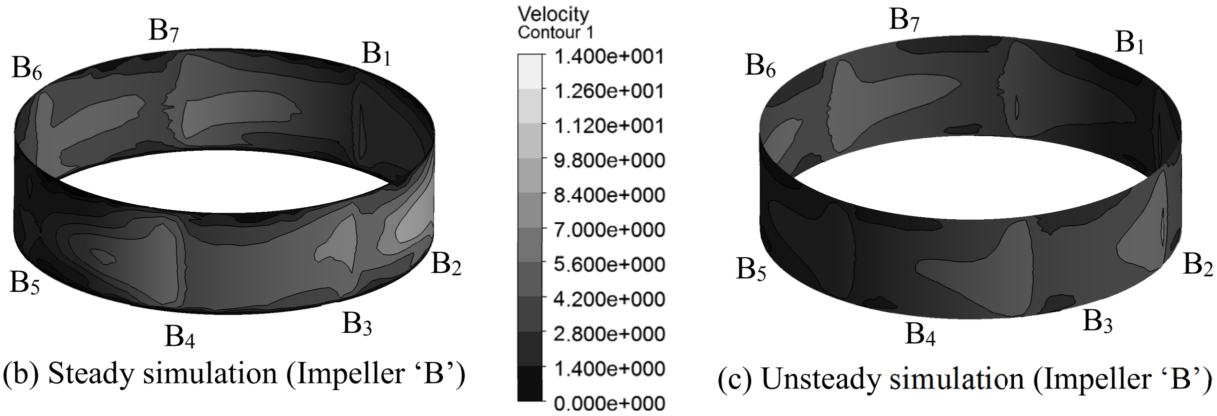

(b) Steady simulation (Impeller 'B')

(c) Unsteady simulation (Impeller 'B')

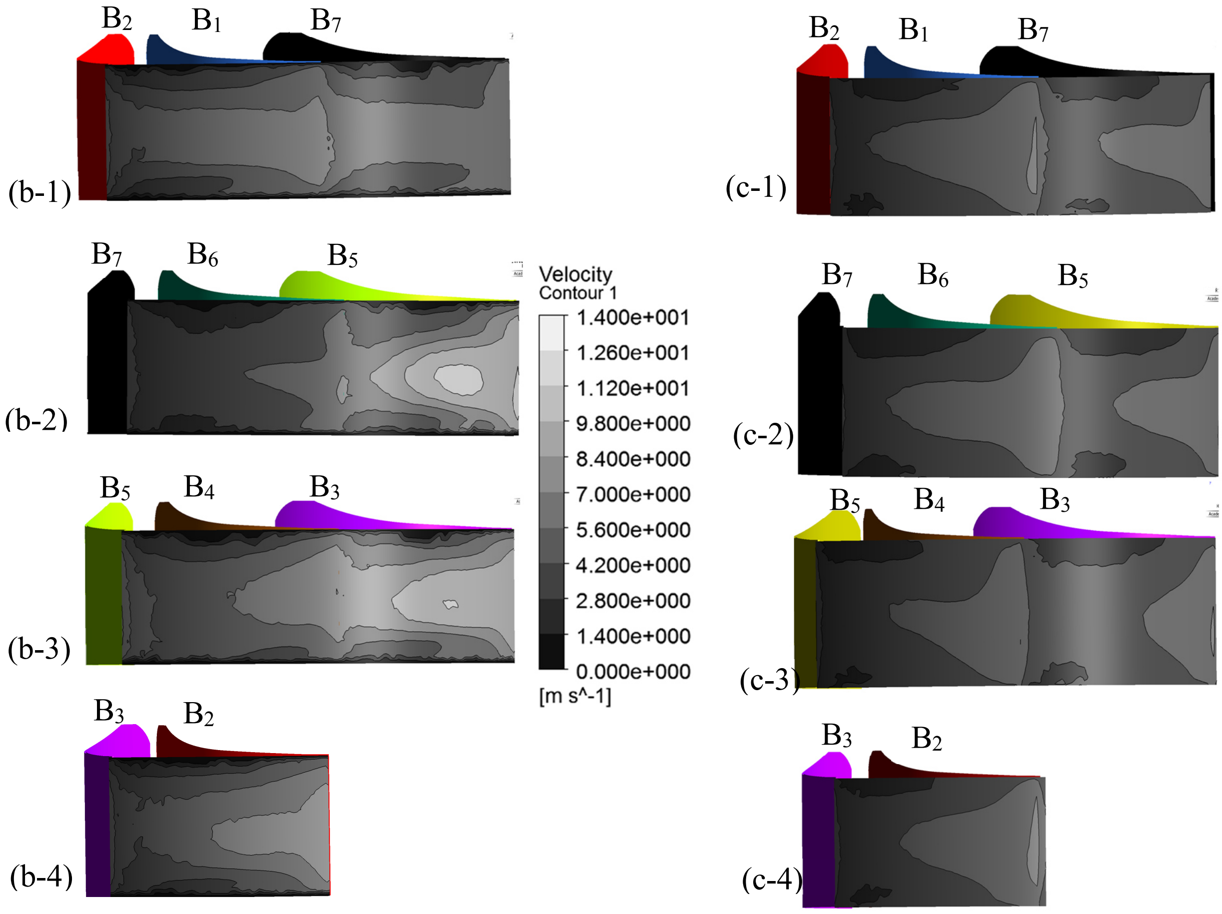

Fig. 5.9 Circumferential outflow pattern ($\phi = 0.014$)

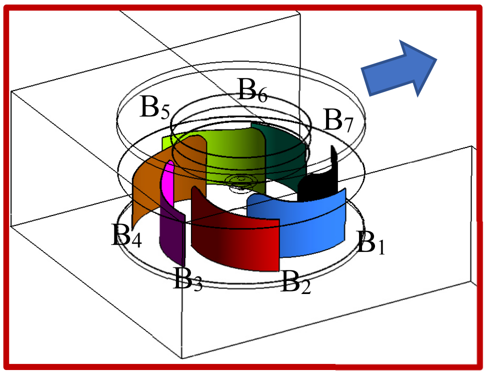

(a) Circumferential outflow location (Impeller ‘B’)

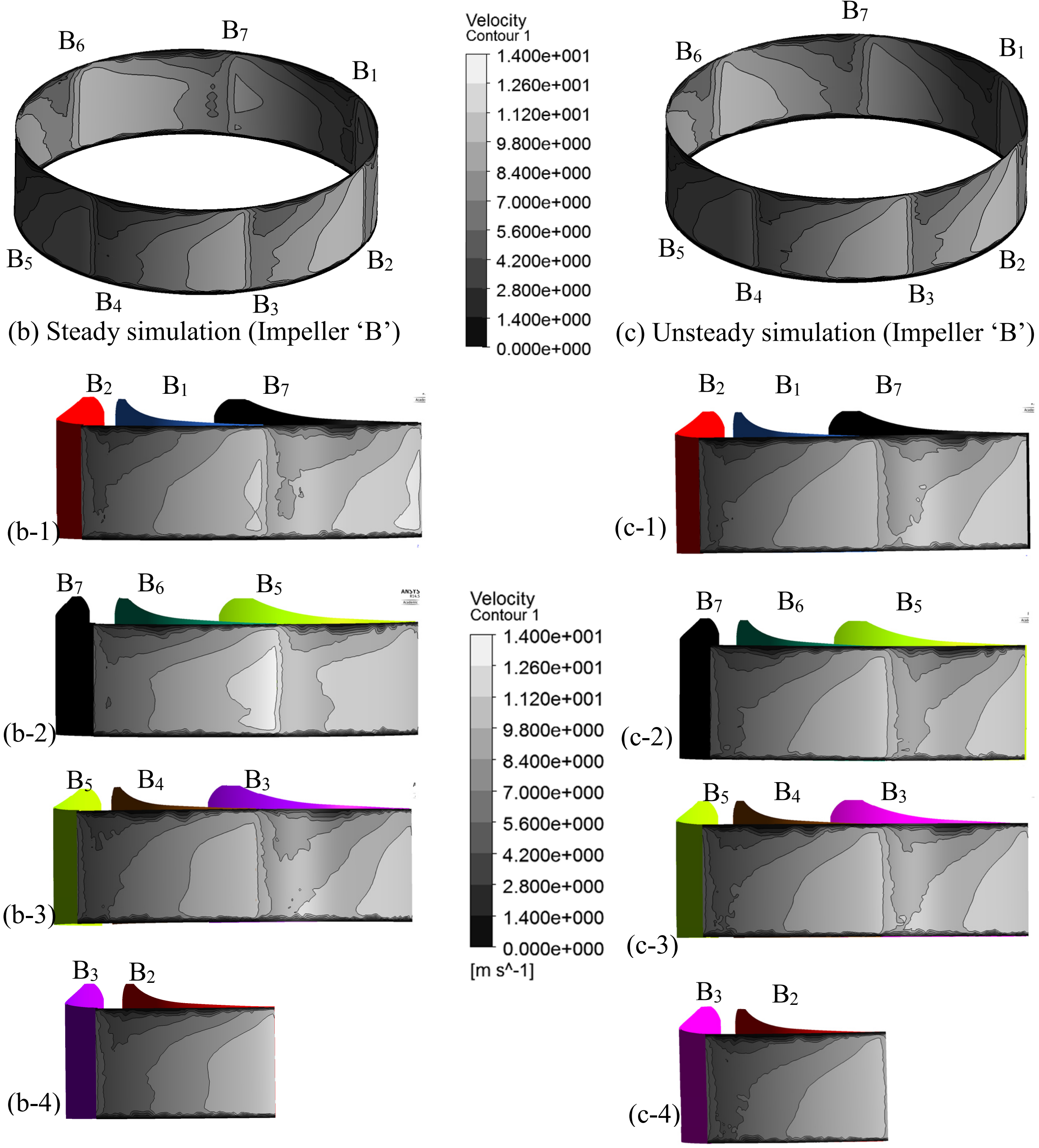

(b) Steady simulation (Impeller ‘B’)

(c) Unsteady simulation (Impeller ‘B’)

Fig. 5.10 Circumferential outflow pattern ($\phi = 0.121$)

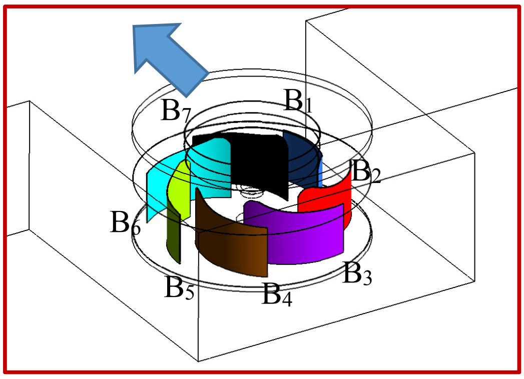

(a) Circumferential outflow location (Impeller 'B')

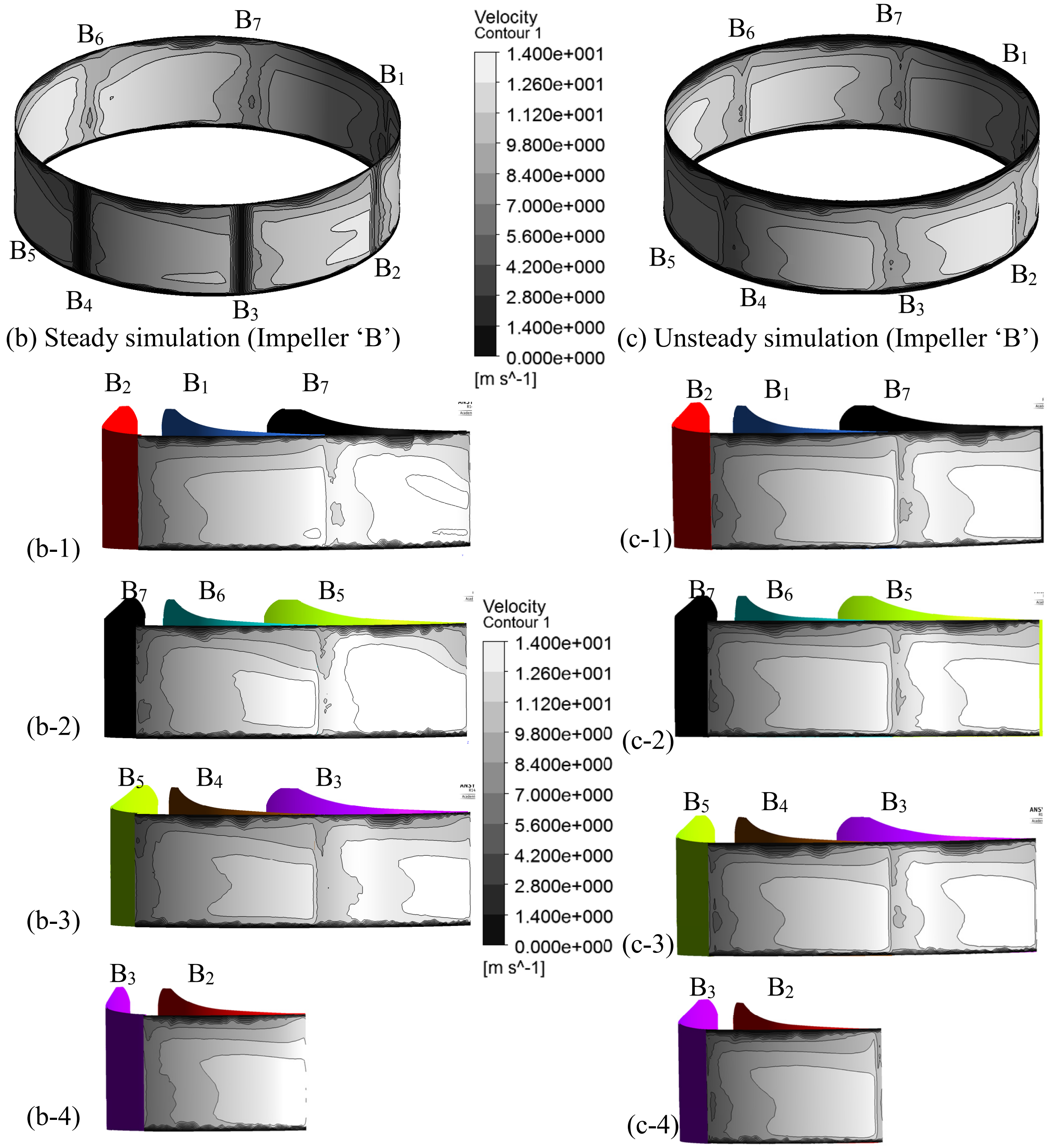

(b) Steady simulation (Impeller 'B')

(c) Unsteady simulation (Impeller 'B')

(b-1) (b-2) (b-3) (b-4)

(c-1) (c-2) (c-3) (c-4)

Fig. 5.11 Circumferential outflow pattern ($\phi = 0.187$)

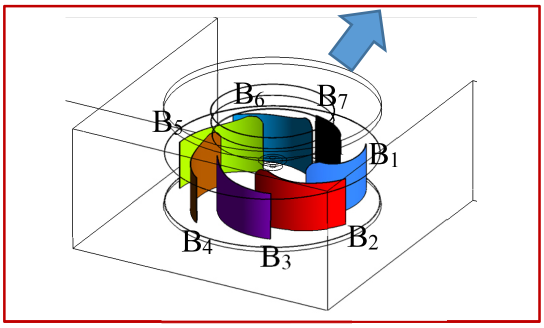

(a) Circumferential outflow location (Impeller ‘B’)

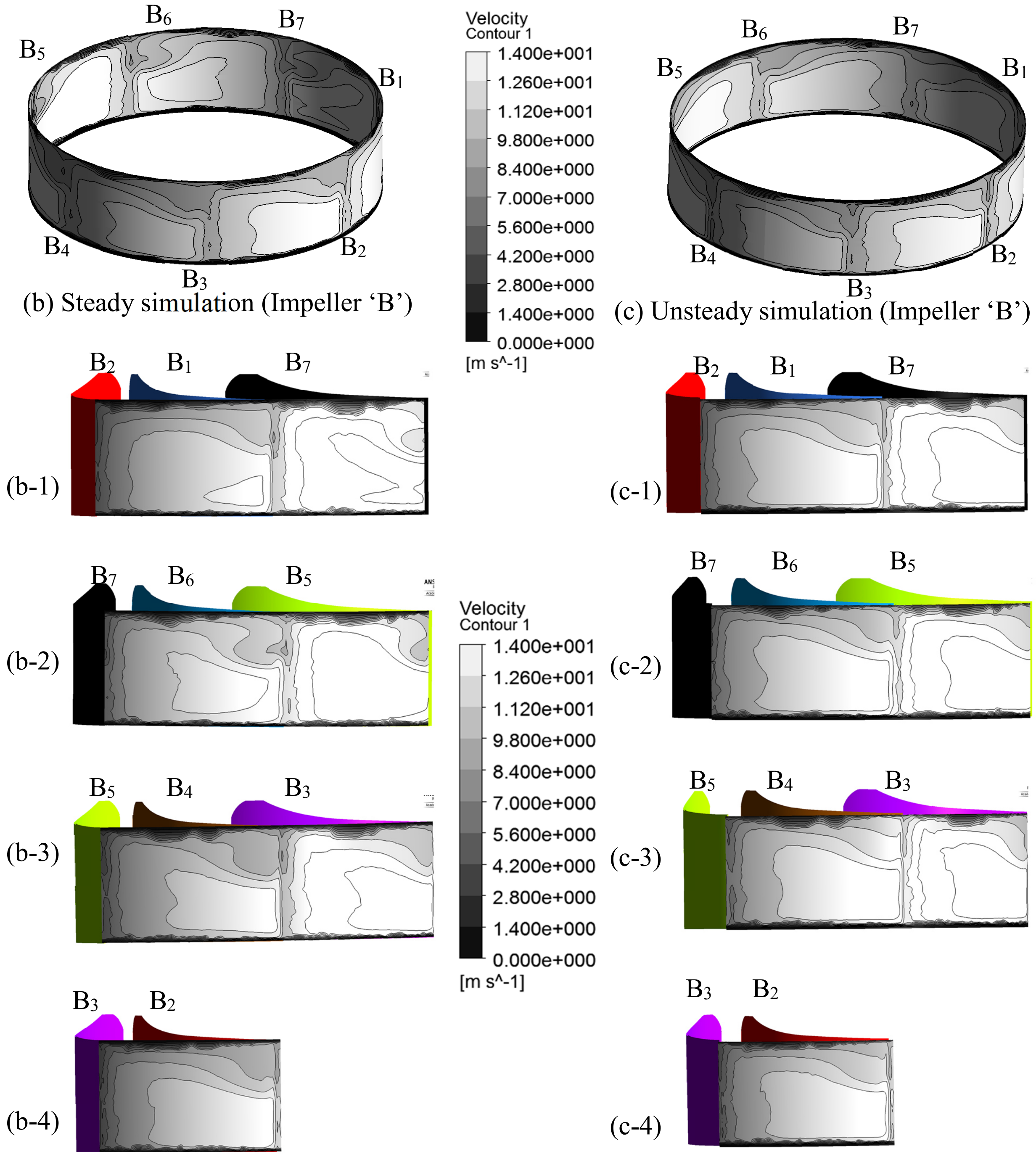

(b) Steady simulation (Impeller ‘B’)

(c) Unsteady simulation (Impeller ‘B’)

Fig. 5.12 Circumferential outflow pattern ($\phi = 0.22$)

Figure 5.13 through Fig. 5.15 show that the static pressure distribution in the mid-span location of the centrifugal fan with the impeller ‘A’ and ‘B’.

In flow coefficient (ϕ = 0.014), the static pressure contour of the steady and unsteady behavior of impeller ‘A’ and ‘B’ are shown in Fig. 5.13 (a) to (d). Figure 5.13 (a) shows the static pressure distributions of the steady flow field of the centrifugal fan with the impeller ‘A’. In Fig. 5.13 (a), the high static pressure distributes on the pressure sides of the blades suction B_1, B_3, B_5, B_6, from which to the circumference of the casing. Thus, the pressure distribution is non-uniform. In Fig. 5.13 (b), the uniform static pressure distributes in all blade sections of the unsteady flow field. The steady behavior for static pressure in the casing is quite a difference from the unsteady.

In Fig. 5.13 (c) and (d) show the static pressure distribution of the centrifugal fan with the impeller ‘B’. In Fig. 5.13 (c), the high static pressure distributes on the pressure side of the blades, B_2, B_3, B_4, and B_5. The static pressure distribution is a little difference in the circumference of the impeller. The uniform static pressure distributes in all blades sections of the impeller in the unsteady flow field. In the low flow coefficient (ϕ = 0.014), the steady static pressure distribution is difference in the static pressure of the unsteady. The steady static pressure behavior in the casing circumferential directions is similar with the unsteady.

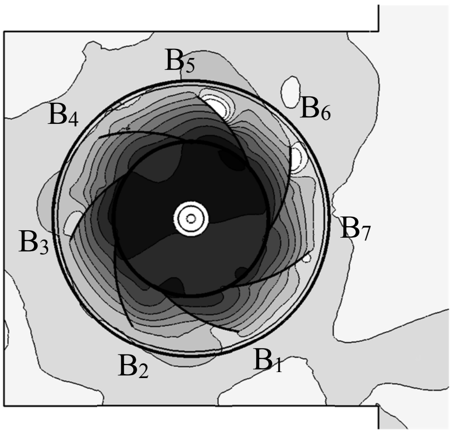

(a) Steady simulation (impeller ‘A’)

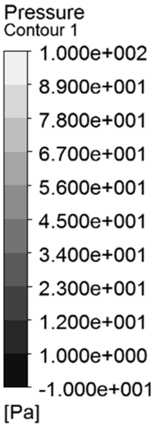

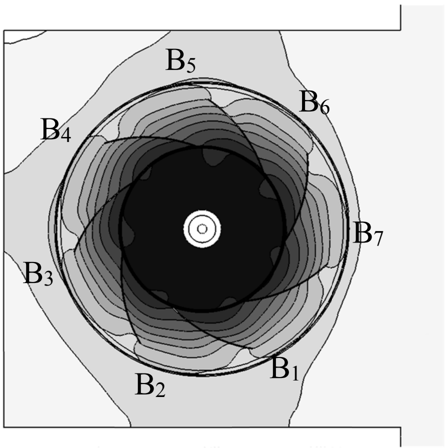

(b) Unsteady simulation (impeller ‘A’)

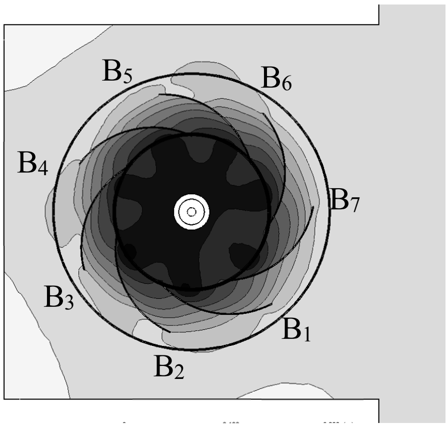

(c) Steady simulation (impeller ‘B’)

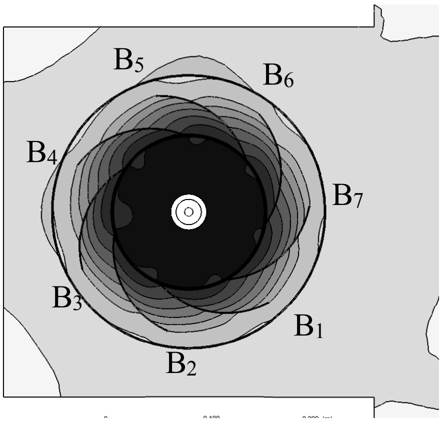

(d) Unsteady simulation (impeller ‘B’)

Fig. 5.13 Static pressure distributions (ϕ = 0.014)

Figure 5.14 (a) to (d) shows the steady and unsteady static pressure distributions of the centrifugal fan with the impeller ‘A’ and ‘B’ in the mid-span. In flow coefficient, $(\phi = 0.121)$ the static pressure contour of the steady and unsteady behavior of impeller ‘A’ shown in Fig. 5.14 (a) and (b). In Fig. 5.14 (a), the low static pressure distributes on the blades, B_1, B_2, B_6, and B_7 where the non-uniform static pressure distributes in the blade sections and circumference of the impeller from which to the casing. In Fig. 5.14 (b), the uniform unsteady static pressure distributes in all blade section. The steady static pressure distribution in the casing is a quite different from the unsteady.

In Fig. 5.14 (c) and (d) shows the steady and unsteady static pressure distribution of the impeller ‘B’. In Fig. 5.14 (c), the steady static pressure on each blade section and impeller ‘B’ outflow to the casing circumference is a little difference. The unsteady static pressure distribution generates as uniform in each blade section and circumference of the impeller ‘B’ outflow to the casing. The steady static pressure distributions in the circumference of the casing is similar to those of the unsteady. In Fig. 5.14 (c), in the steady simulation, the high static pressure occurs in the blade section B_1, B_2, B_3 and B_4 which distributes to the region of the rear casing wall, but the low pressure distributes on the region of middle of the rear casing wall.

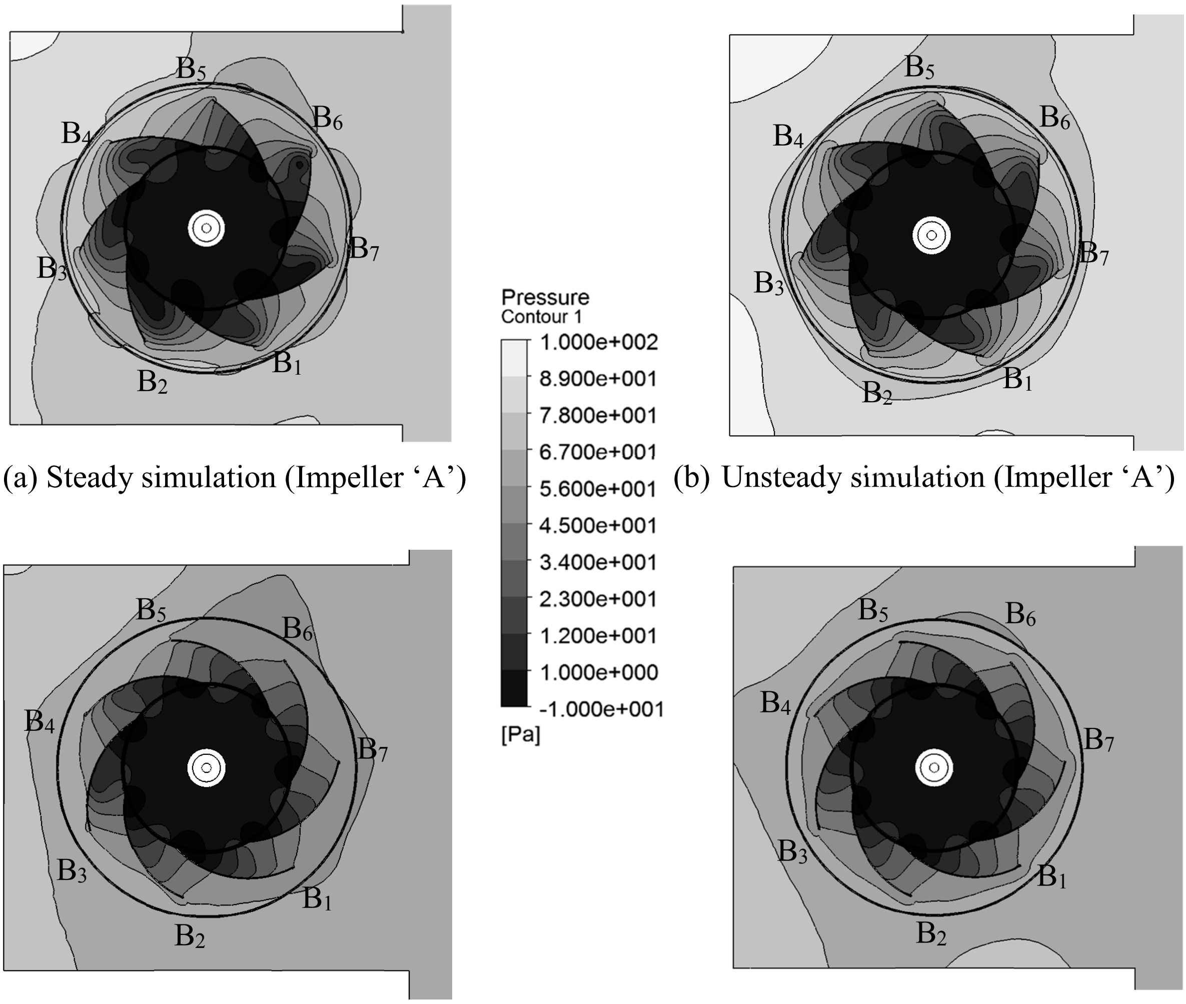

(a) Steady simulation (Impeller ‘A’)

(b) Unsteady simulation (Impeller ‘A’)

(c) Steady simulation (Impeller ‘B’)

(d) Unsteady simulation (Impeller ‘B’)

Fig. 5.14 Static pressure distributions $(\phi = 0.121)$

Figure 5. 15 shows the pressure distributions at the design flow coefficient, (ϕ = 0.187). Figure 5.15 (a) and (b) are the case of the impeller ‘A’. The results in steady simulation shows that the flow in the impeller of Fig. 5.15 (a) is varied in circumferential location. The pressure at the inlet of impeller is low in the region of the outlet, B_5 to B_7 and B_1 to B_2. But the pressure is large in the back region of the fan, B_3 to B_4. This pressure distribution continues to the impeller outlet. The static pressure is a little high in the impeller ‘A’ outflow region, between B_2 and B_5. In the casing, the pressure is lower at the fan exit, B_6, B_7, but larger at back region, B_3 to B_5. In the unsteady simulation, the pressure distribution in circumferential location is little varied in the casing and is high only at the corner. The discrepancy of steady and unsteady simulation is cause by the process of flow from the inlet to outlet of the impeller. Figure 5.15 (c) and (d) shows the case of the impeller ‘B’. The static pressure distribution in steady simulation is little difference with unsteady within the blade sections. The low steady static pressure distributes form the impeller outflow to the fan exit.

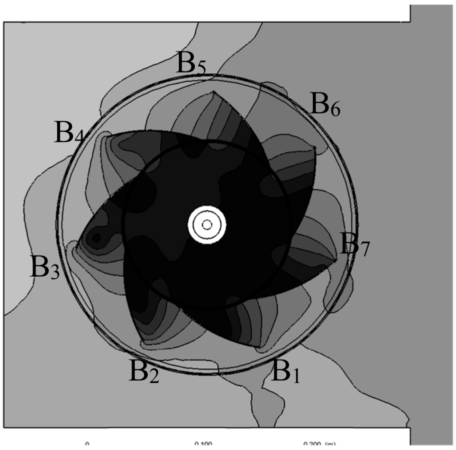

(a) Steady simulation (Impeller ‘A’)

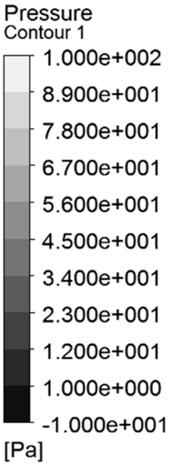

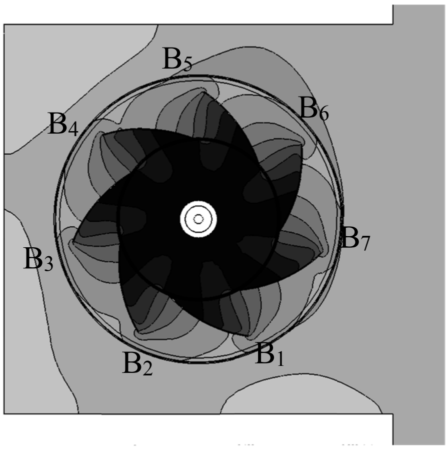

(b) Unsteady simulation (Impeller ‘A’)

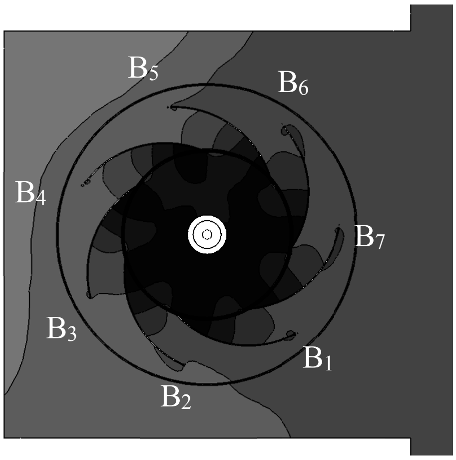

(c) Steady simulation (Impeller ‘B’)

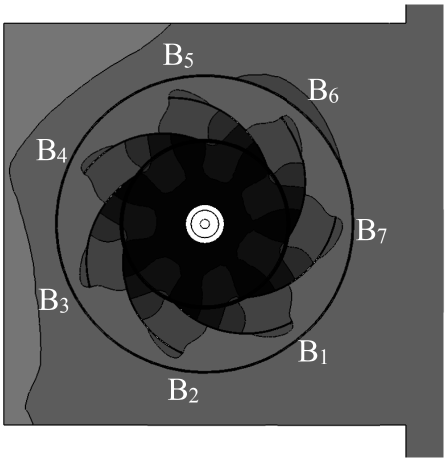

(d) Unsteady simulation (Impeller ‘B’)

Fig. 5.15 Static pressure distributions (ϕ = 0.187)

Figure 5.16 shows the pressure distributions of the at the large flow coefficient, (ϕ = 0.22). Figure 5.16 (a) and (b) are the case of the impeller ‘A’. The results in steady simulation shows that the flow in the impeller of Fig. 5.16 (a) is varied in circumferential location. The pressure at the inlet of impeller is low in the region of the outlet, B_1, B_7, B_6 and B_5 from which, the pressure distributes to the fan exit. But the pressure is large in the back region of the fan, B_3 to B_4. The static pressure is a little high in the impeller 'A' outflow region, between B_2 and B_5. In the casing, the pressure is lower at the fan exit, B_6, B_7, but larger at back region, B_3 to B_5. In the unsteady simulation, in Fig. 5.16 (b), the pressure distribution in circumferential location is little varied in the casing and is high only at the corner. Figure 5.16 (c) and (d) shows the case of the impeller 'B'. The static pressure distribution in steady simulation is little difference with unsteady within the blade sections.

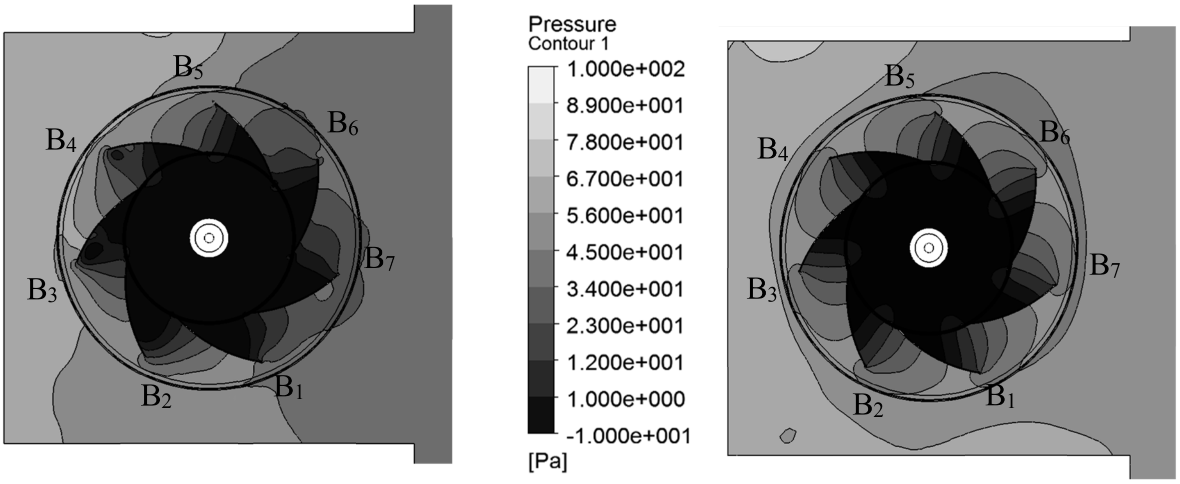

(a) Steady simulation (Impeller 'A')

(b) Unsteady simulation (Impeller 'A')

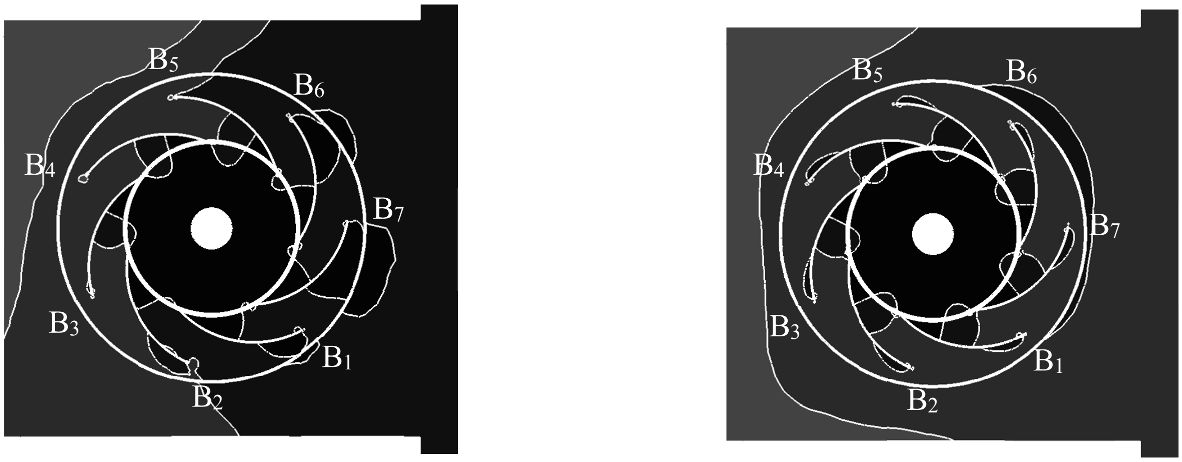

(c) Steady simulation (Impeller 'B')

(d) Unsteady simulation (Impeller 'B')

Fig. 5.16 Static pressure distributions (ϕ = 0.22)

5.1.2 Static pressure distribution

Figure 5.17 to Fig. 5.20 shows the circumferential static pressure distribution of the impeller (impeller 'A') which are compared base on the steady and unsteady simulation results. In these figures, (a), (a-1) to (a-4) refer to the steady simulation results and (b), (b-1) to (b-4) refers to the unsteady simulation results.

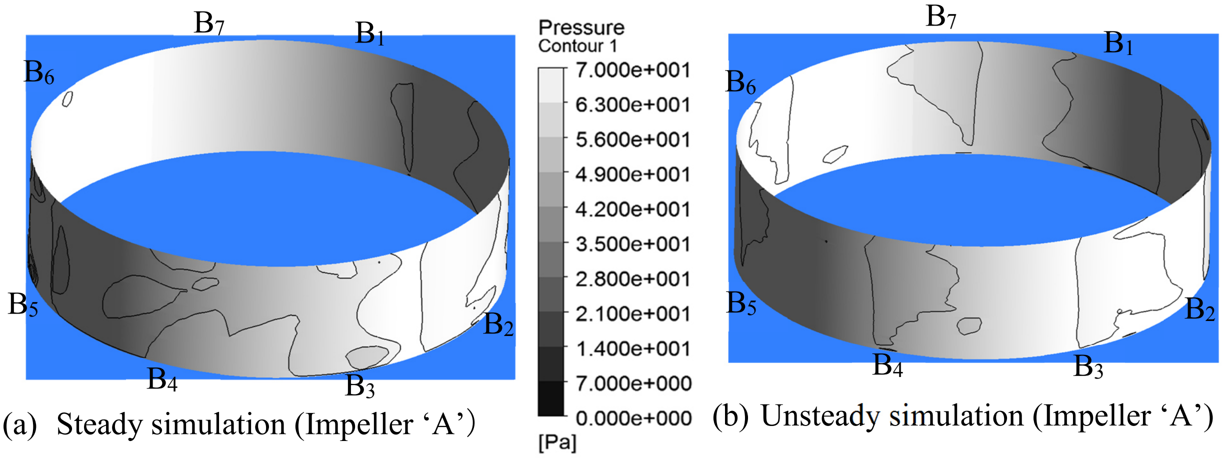

(a) Steady simulation (Impeller 'A')

(b) Unsteady simulation (Impeller 'A')

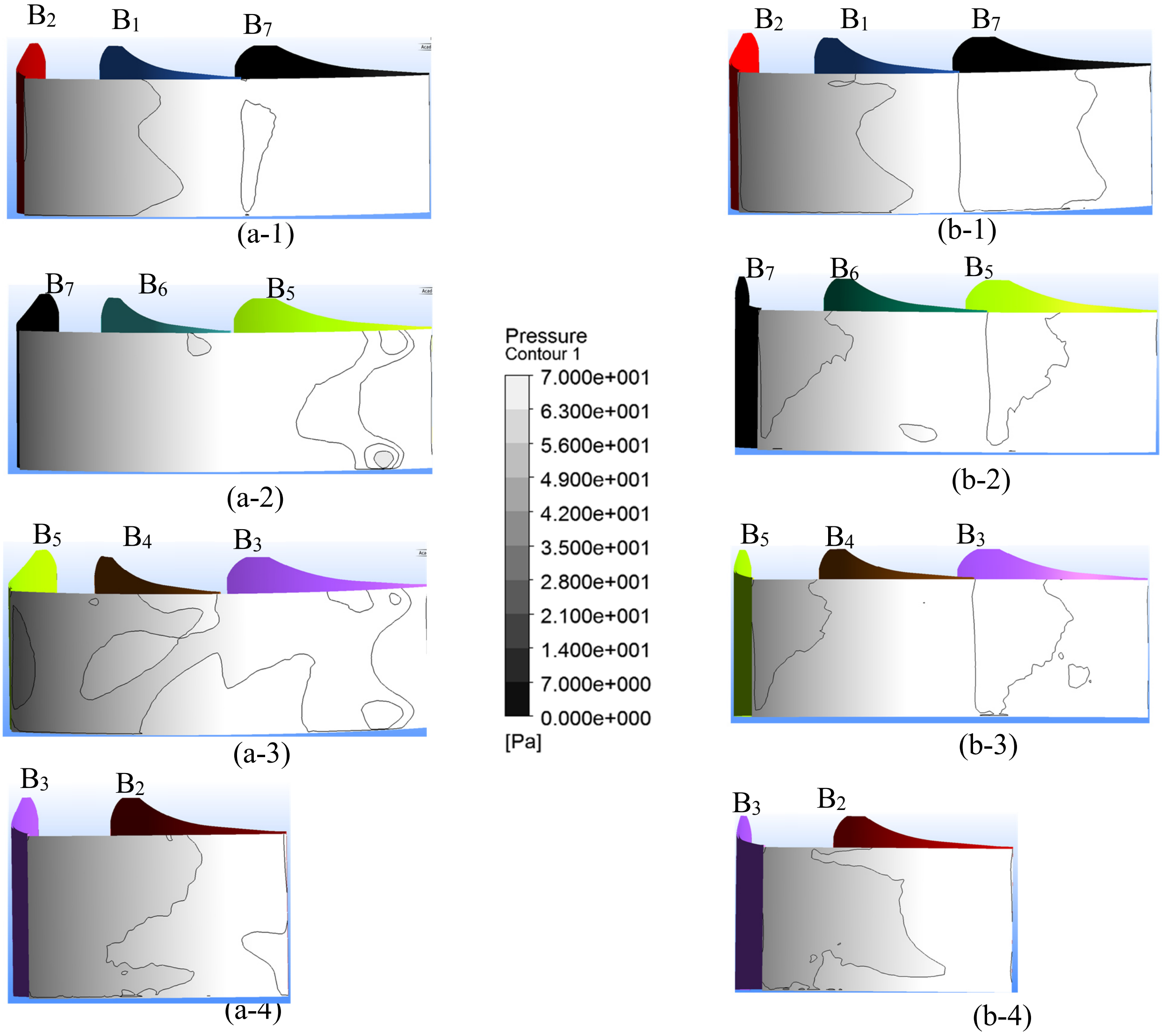

(a-1) (b-1)

(a-2) (b-2)

(a-3) (b-3)

(a-4) (b-4)

Fig. 5.17 Static pressure distributions ($\phi = 0.014$)

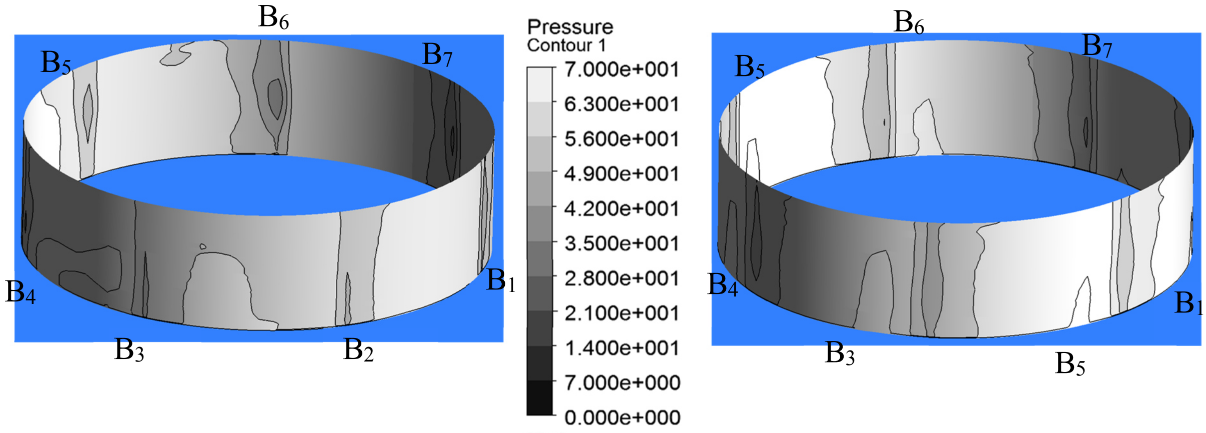

(a) Steady simulation (Impeller ‘A’)

(b) Unsteady simulation (Impeller ‘A’)

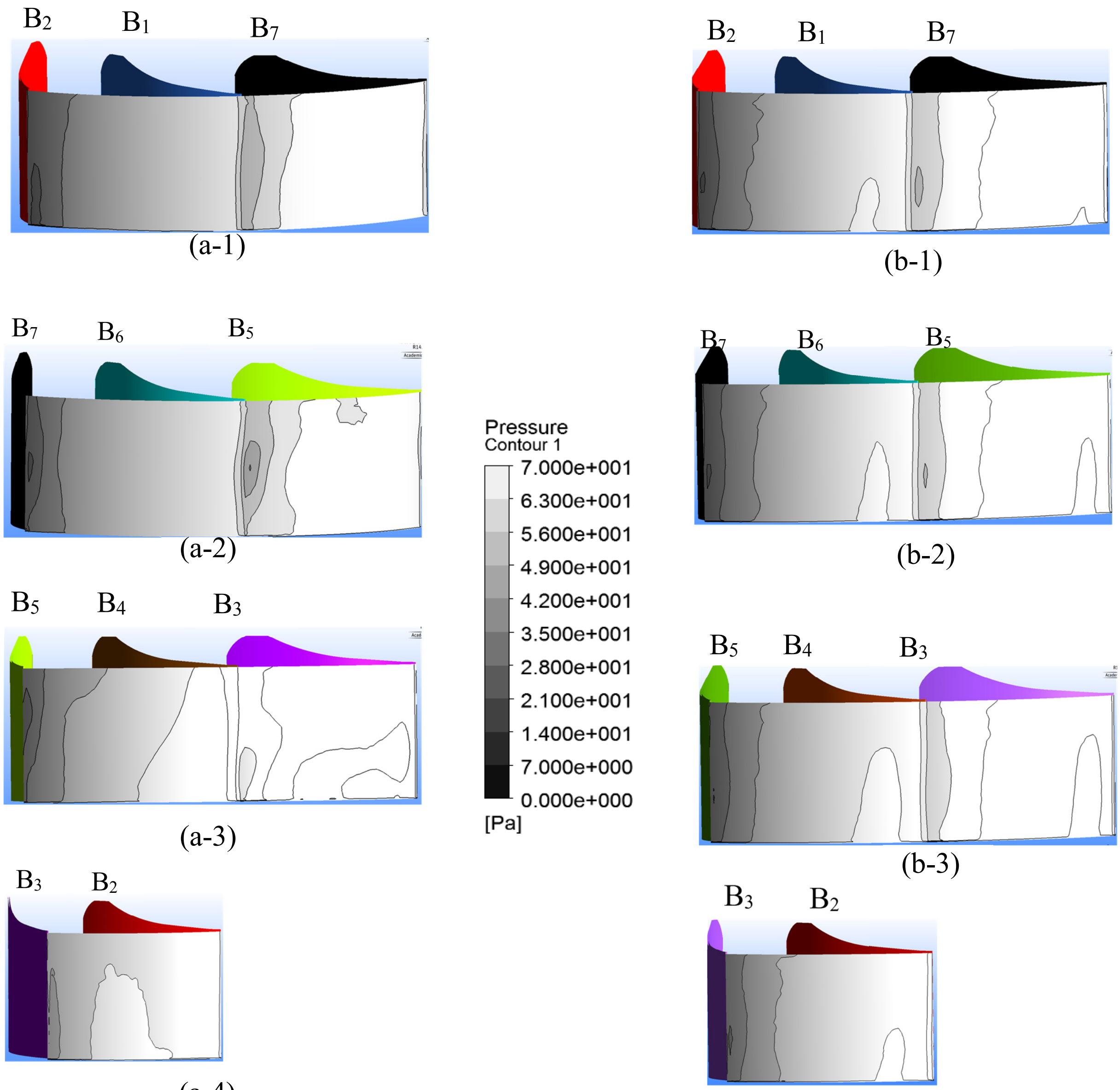

(a-1) (b-1)

(a-2) (b-2)

(a-3) (b-3)

(a-4) (b-4)

Fig. 5.18 Static pressure distributions (ϕ = 0.121)

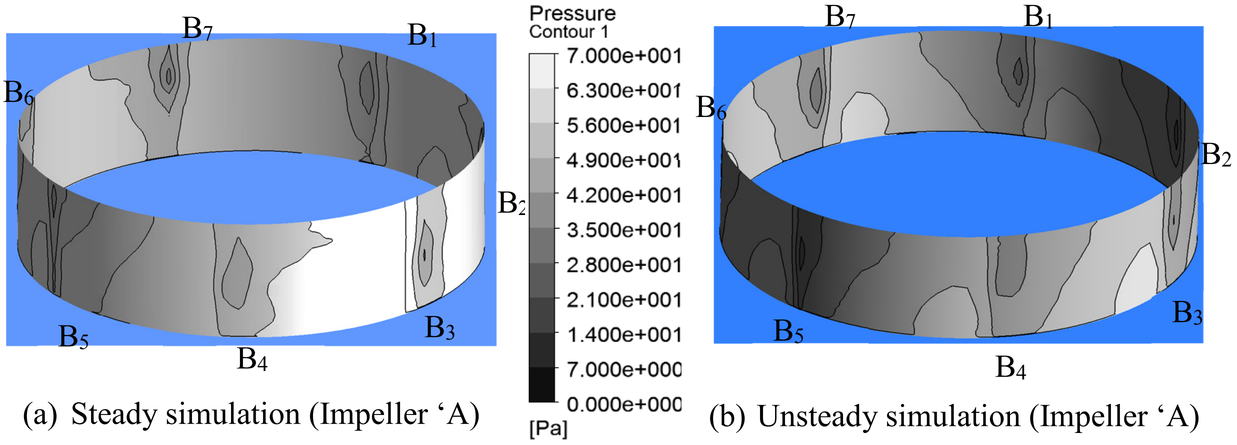

(a) Steady simulation (Impeller 'A)

(b) Unsteady simulation (Impeller 'A)

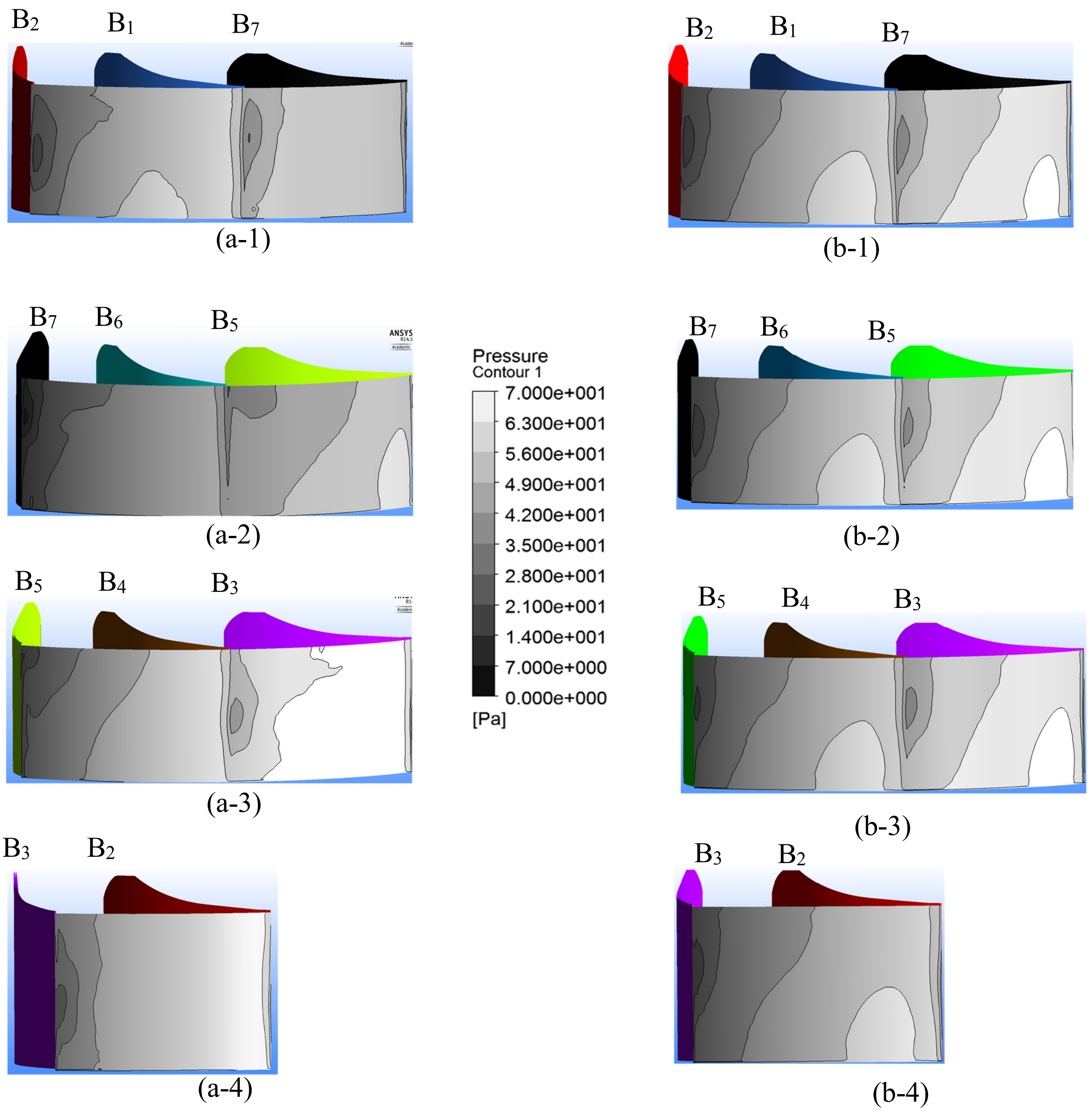

Fig. 5.19 Static pressure distributions ($\phi = 0.187$)

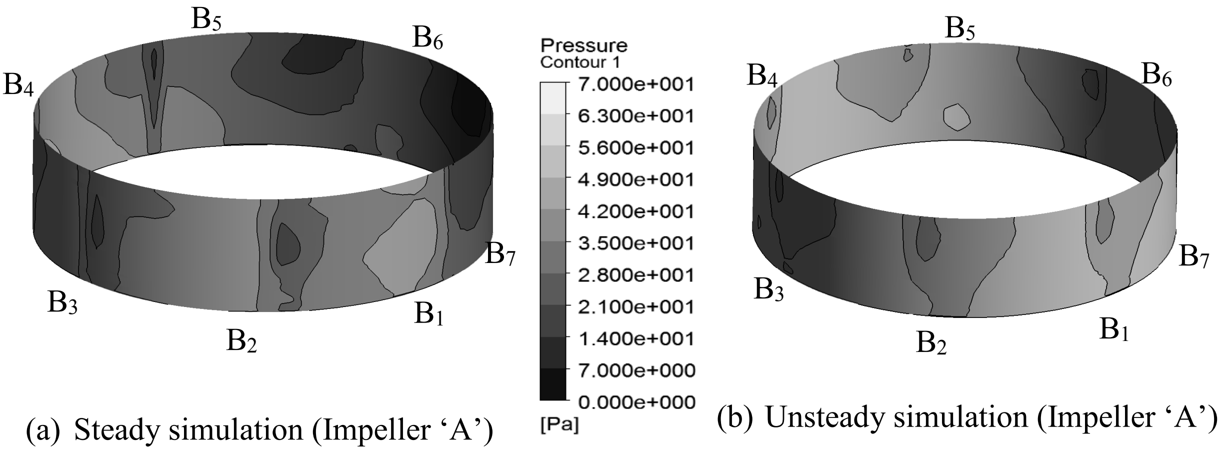

(a) Steady simulation (Impeller 'A')

(b) Unsteady simulation (Impeller 'A')

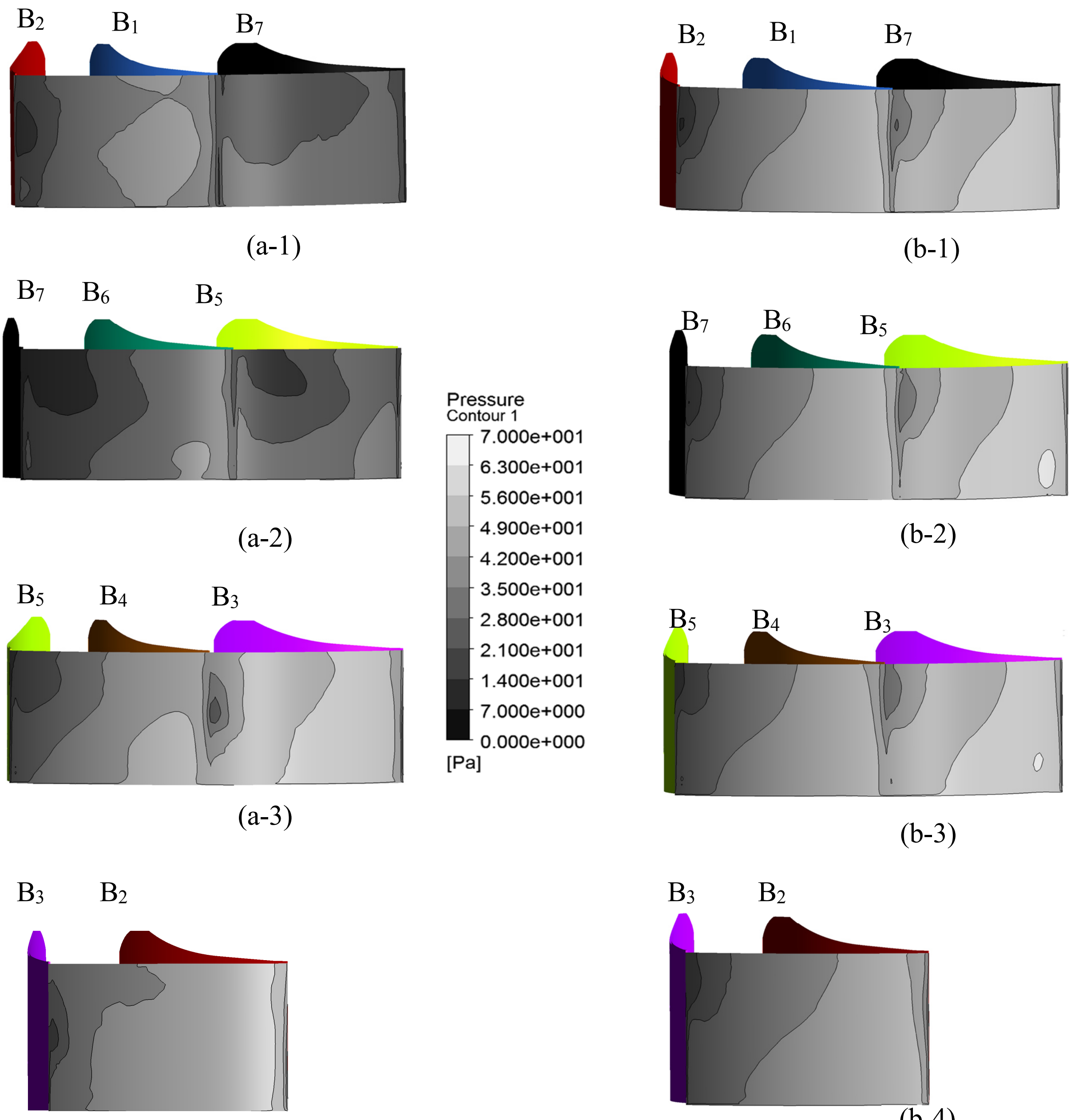

(a-1)

(b-1)

(a-2)

(b-2)

(a-3)

(b-3)

(a-4)

(b-4)

Fig. 5.20 Static pressure distributions (ϕ = 0.22)

Figure 5.17 show the static pressure distribution in the low flow rate ($\phi = 0.014$) that the comparison of the static pressure distribution in the steady simulation to the unsteady. In steady cases, the pressure distribution is non-uniform in each region. The high static pressure generates in B_6-B_7 in Fig. 5.17 (a-2), B_7-B_1 in Fig. 5.17 (a-1). This region is in the exit of the fan. In Fig. 5.17 (b), the static pressure distribution in each blade region is a little difference, and the dominant blade regions are B_1-B_2 in Fig. 5.17 (b-1) and B_2-B_3 in Fig. 5.17 (b-4).

Figure 5.18 shows the static pressure in the flow rate (ϕ=0.121) that the comparison of the static pressure distribution in the steady to the unsteady. In steady cases, the pressure distribution is non-uniform in each region. The high static pressure generates in B_3-B_4 and B_4-B_5 in Fig. 5.18 (a-3). The pressure distributes from this region to the casing back of the fan. In Fig. 5.18 (b), the static pressure distribution is a little difference.

Figure 5.19 shows the static pressure in the design flow rate (ϕ=0.187) that the comparison of the static pressure distribution in the steady to the unsteady. In steady cases, the high static pressure distributes in the circumference of the impeller in B_3-B_4 and B_4-B_5 shown in Fig. 5.19 (a-3) to the casing backward. In Fig. 5.19 (b), the static pressure distribution is uniform in each blade section.

Figure 5.20 shows the static pressure in the design flow rate (ϕ=0.22) that the comparison of the static pressure distribution in the steady to the unsteady. In steady cases, the high static pressure distributes in the circumference of the impeller in B_3-B_4 and B_4-B_5 shown in Fig. 5.20 (a-3) to the casing backward. In Fig. 5.20 (b), the static pressure distribution is uniform in each blade section.

Figure 5.21 to Fig. 5.24 shows the circumferential distribution of the static pressure for the impeller (impeller 'B') which are compared base on the steady and unsteady simulation results. In these figures, (a), (a-1) to (a-4) refer to the steady simulation results and (b), (b-1) to (b-4) refers to the unsteady simulation results.

Figure 5.21 shows the static pressure distribution in the low flow rate ($\phi = 0.014$) that the comparison of the static pressure distribution in the steady to the unsteady. In both steady and unsteady simulations, non-uniform static pressure distributes in the circumference of the impeller outlet. In steady cases, the pressure distribution is non-uniform in each region. The high static pressure generates in B_3-B_4 and B_4-B_5 in Fig. 5.21 (a-3). This region is in the back of the casing. The steady static pressure distribution is higher than in the unsteady.

Figure 5.22 shows the static pressure distribution in the flow rate (ϕ=0.121). In steady cases, the pressure distribution is non-uniform in each region. The high static pressure generates in B_3-B_4 and B_4-B_5 in Fig. 5.22 (a-3). The pressure distributes from this region to the casing back of the fan. In the unsteady of Fig. 5.22 (b), the static pressure distribution is uniform.

Figure 5.23 shows the static pressure distribution in the design flow rate (ϕ=0.187). In steady cases, the high static pressure distributes in the circumference of the impeller in B_3-B_4 and B_4-B_5 shown in Fig. 5.23 (a-3) to the casing backward. The pressure distribution is a little difference in each blade regions. In the unsteady of Fig. 5.23 (b), the static pressure distribution is uniform in each blade section.

Figure 5.24 shows the static pressure distribution in the high flow rate (ϕ=0.22). In steady cases, the low static pressure distributes in the circumference of the impeller in B_2-B_1 and B_1-B_7 shown in Fig. 5.24 (a-1) to the casing backward. In the unsteady of Fig. 5.24 (b), the static pressure distribution is uniform in each blade section.

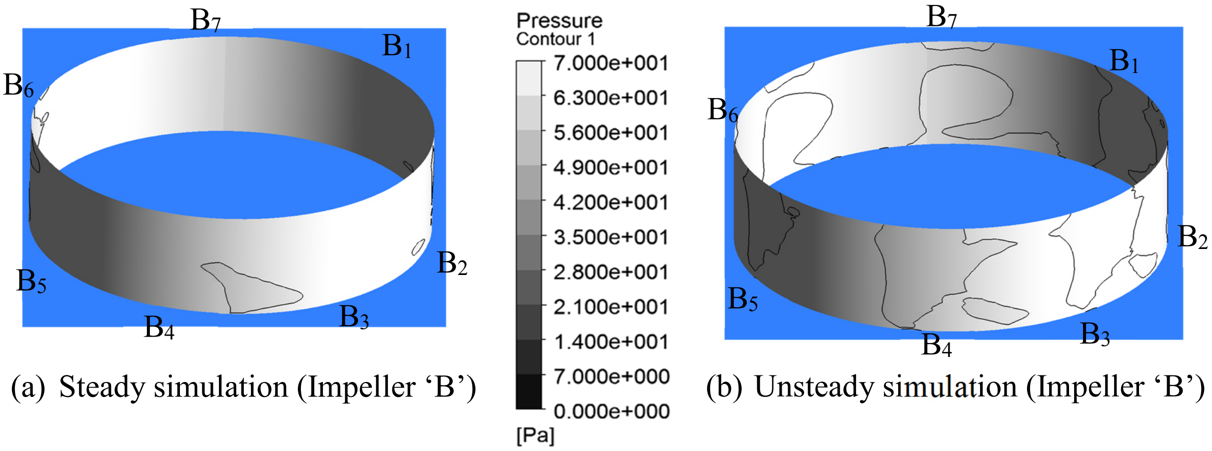

(a) Steady simulation (Impeller 'B')

(b) Unsteady simulation (Impeller 'B')

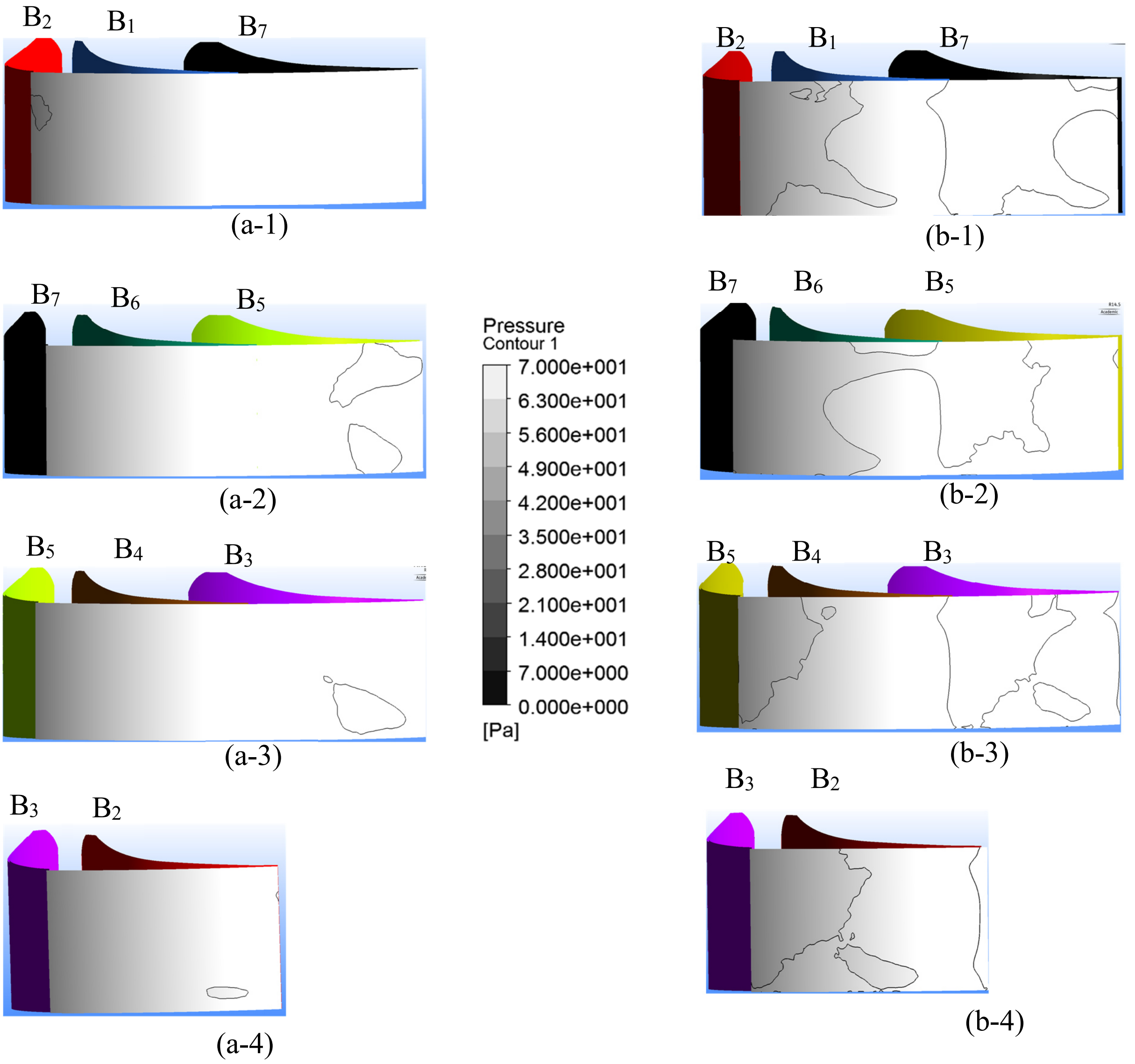

(a-1) (b-1)

(a-2) (b-2)

(a-3) (b-3)

(a-4) (b-4)

Fig. 5.21 Static pressure distributions (ϕ = 0.014)

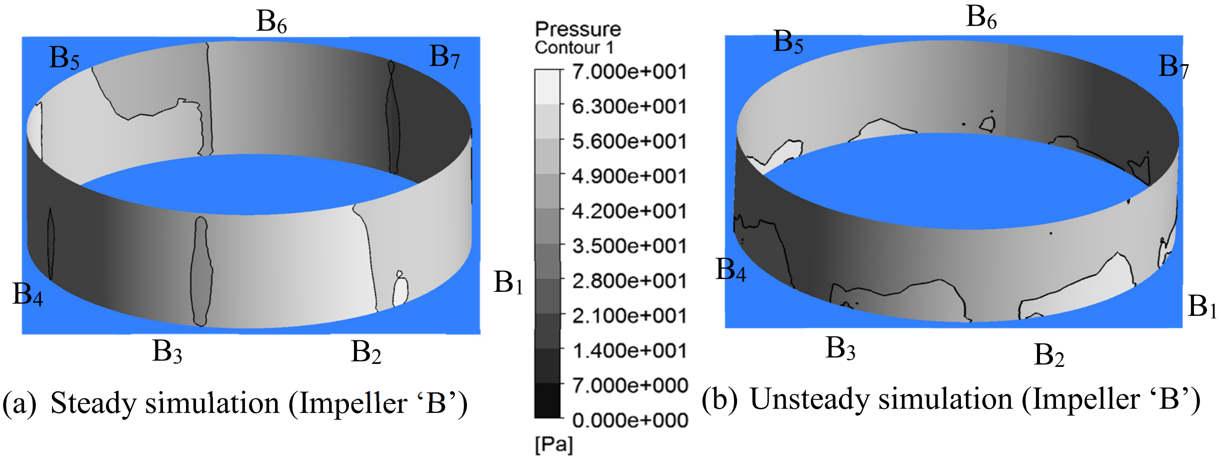

(a) Steady simulation (Impeller ‘B’) (b) Unsteady simulation (Impeller ‘B’)

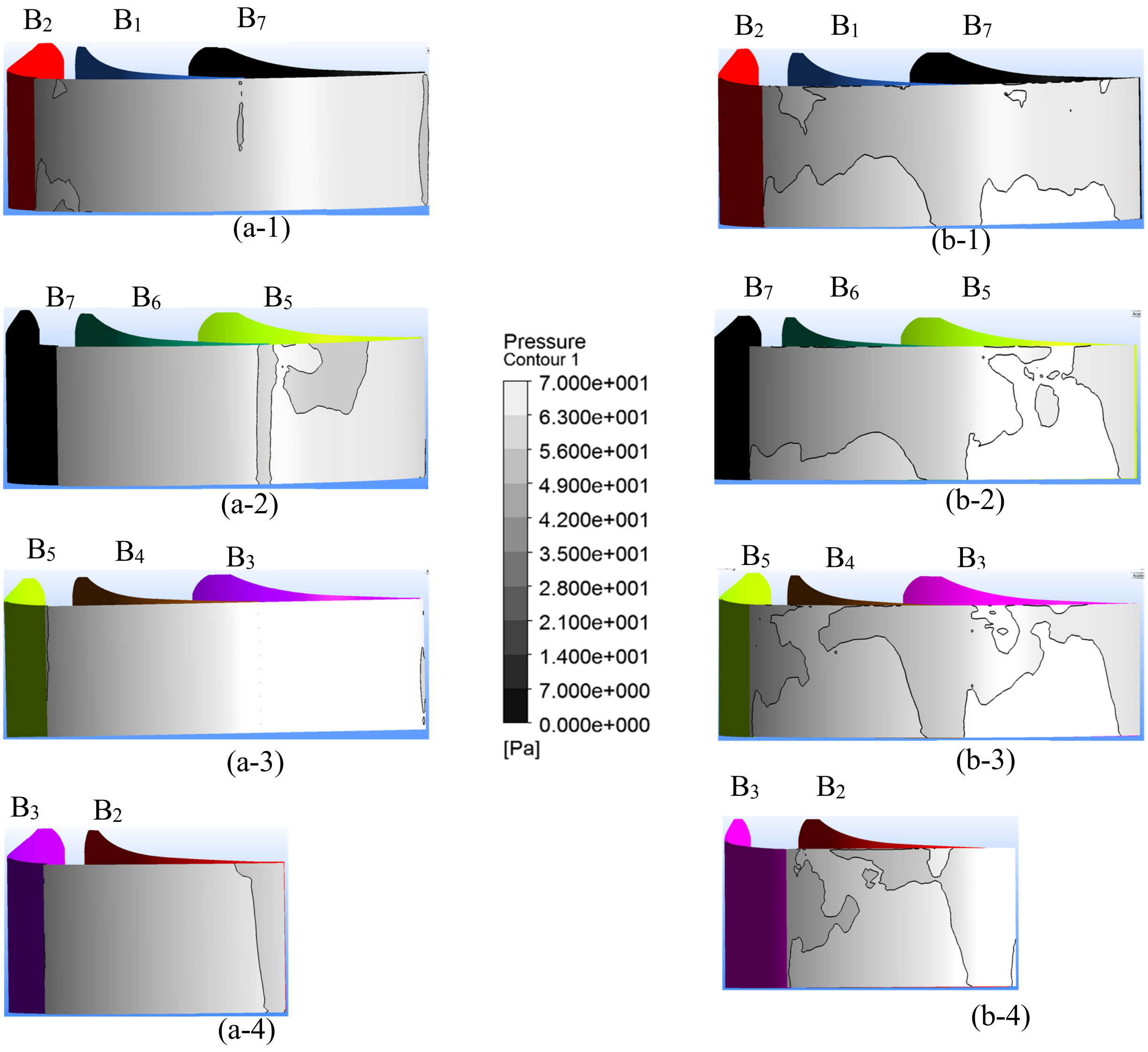

Fig. 5.22 Static pressure distributions ($\phi = 0.121$)

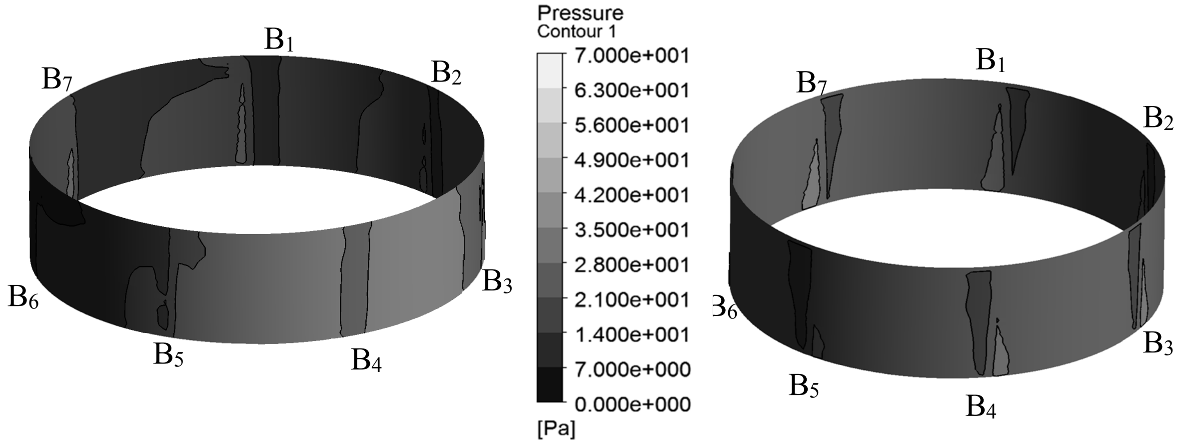

(a) Steady simulation (Impeller ‘B’)

(b) Unsteady simulation (Impeller ‘B’)

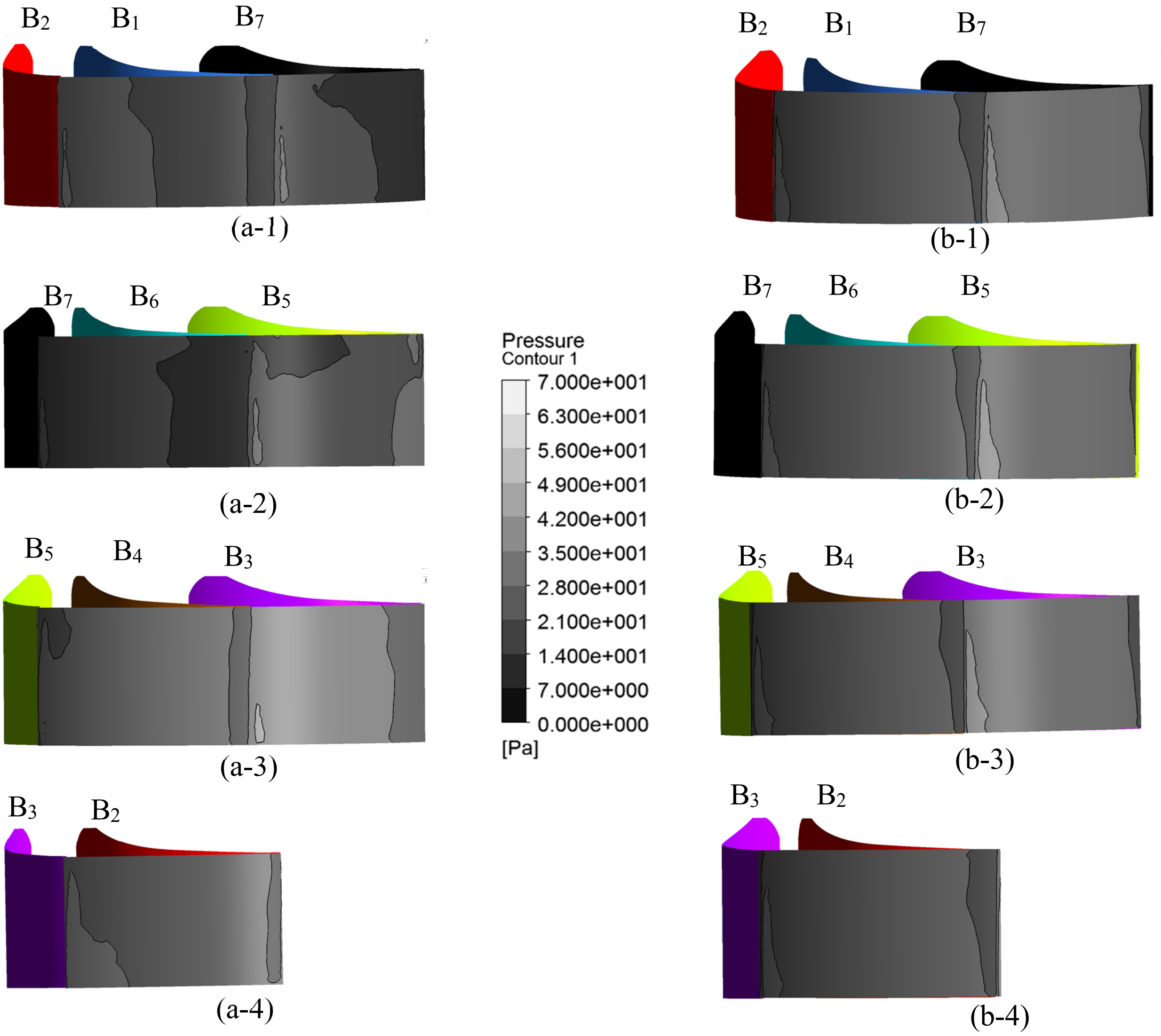

(a-1) (b-1)

(a-2) (b-2)

(a-3) (b-3)

(a-4) (b-4)

Fig. 5.23 Static pressure distributions ($\phi = 0.187$)

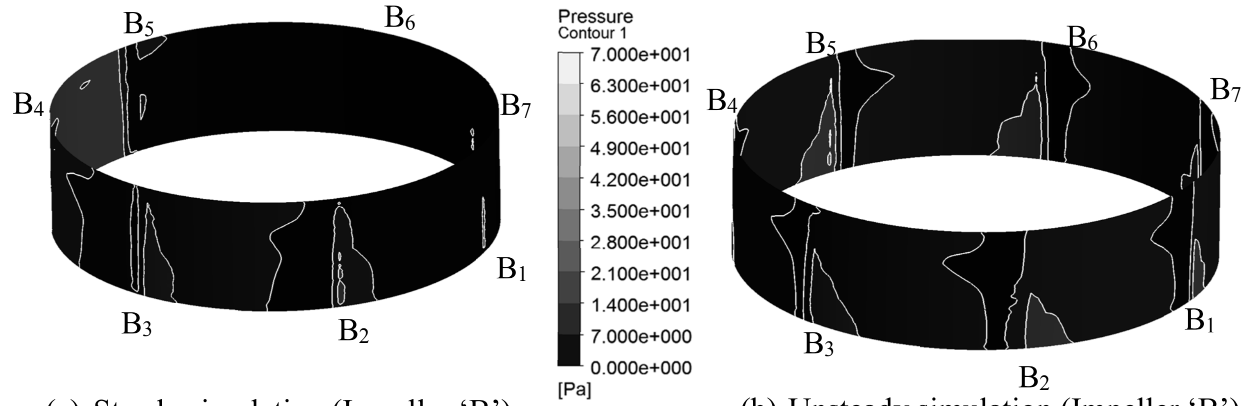

(a) Steady simulation (Impeller 'B')　(b) Unsteady simulation (Impeller 'B')

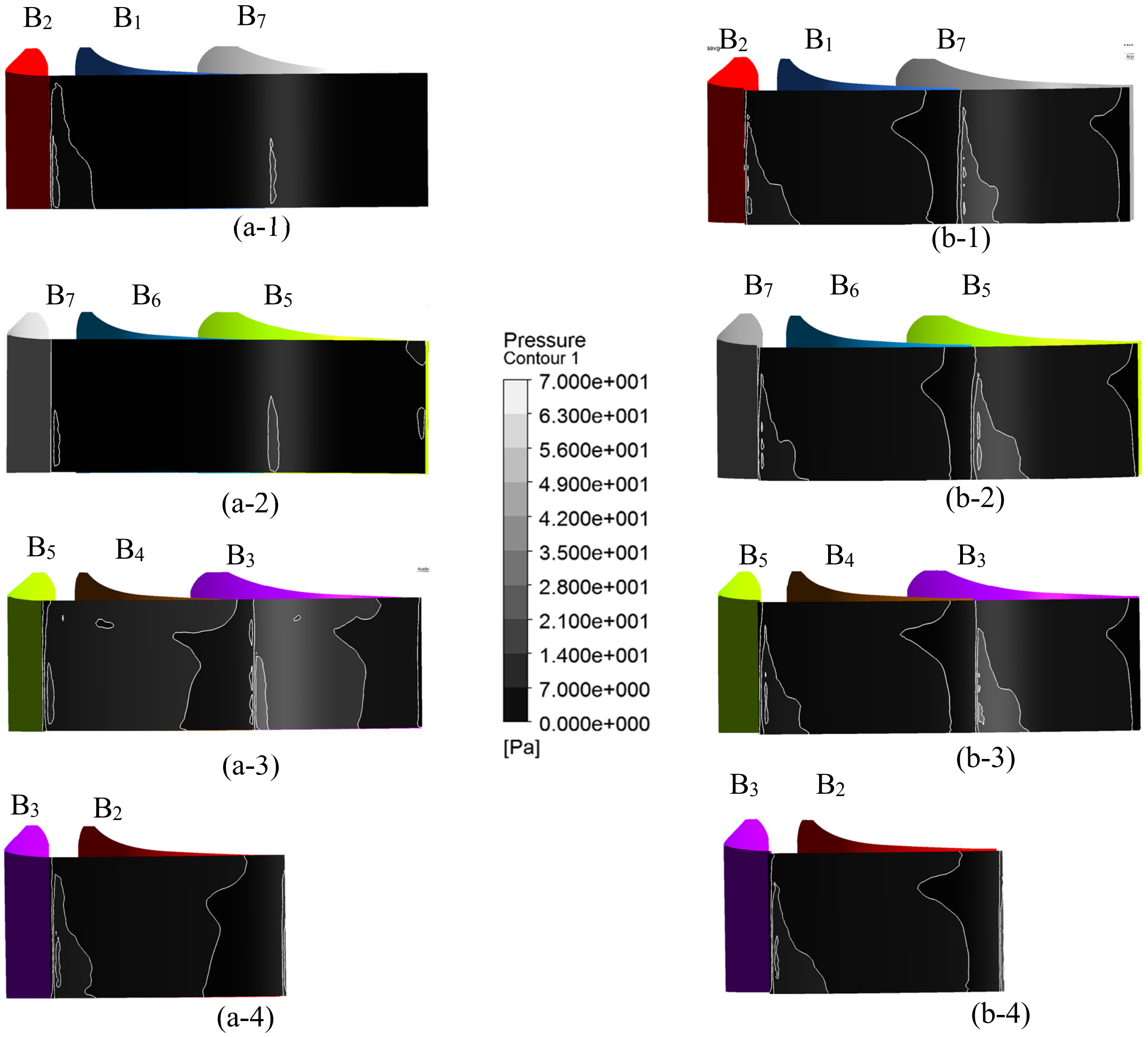

Fig. 5.24 Static pressure distributions (ϕ = 0.22)

5.2 Performance of the centrifugal fan base on Steady and Unsteady Simulation

Fan performance is typically defined by the pressure and power requirement over a range of fan-generated airflow. Understanding this relationship is essential to designing and operating a fan system.

In this study, the fan performance is graphically depicted the basic fan characteristics data of flow coefficients (ϕ), the static pressure coefficients (ψ_s) and the efficiency (η). In this result, the performance curves illustrate by comparing the performance characteristics, i.e., the rate of change between the flow and pressure, of both fan types having the impeller 'A' and the impeller 'B' having the difference blade outlet angle. The CFX calculation result of fan performance valid with the experimental one.

The flow rate coefficient, the static pressure coefficient, the total pressure coefficient, the efficiency in Fig. 5.25 to Fig. 5.26 is defined with the following equations.

The flow rate coefficient (ϕ):

$$\phi = \frac{60Q}{\pi^2 D^2 HN} \tag{5.1}$$

The static pressure coefficient (ψ_s):

$$\psi_s = \frac{2P}{\rho\pi^2 D^2 (N/60)^2} \tag{5.2}$$

The efficiency (η):

$$\eta = \frac{PQ}{T\omega} \tag{5.3}$$

Where, D is the outlet diameter of the impeller [m].

H is exit blade height [m].

N is rotating speed [rpm].

P is the static or total pressure rise [Pa].

Q is the air flow rate [m^3/s].

T is the impeller torque [N.m].

ρ_{air} is the density of air at $T = 25.4°\mathrm{C}$, ($\rho_{air} = 1.1829$ kg/m^3).

ω is an angular speed of the impeller [rad/s].

Figure 5.25 shows the comparison of the performance between the steady and unsteady simulation. Figure 5.25 (a) is the static and the total pressure coefficients of fans of impeller

‘A’ and ‘B’. For the impeller ‘A’, the static and total pressure coefficients in steady simulation is quite a difference from the unsteady simulation. But for the impeller ‘B’, these coefficients in steady simulation are almost the same in unsteady simulation. For the case of impeller ‘A’, the static and total pressure coefficients are lower than in unsteady simulation. Figure 5.25 (b) shows the efficiency of the fans of each impeller ‘A’ and ‘B’. For the impeller ‘B’, the efficiency in steady simulation is well coincident to the unsteady simulation except large flow rate. But for the case of impeller ‘A’, the efficiency in steady simulation is very low compared to the unsteady simulation. The difference between two is about 0.2 in all flow rate.

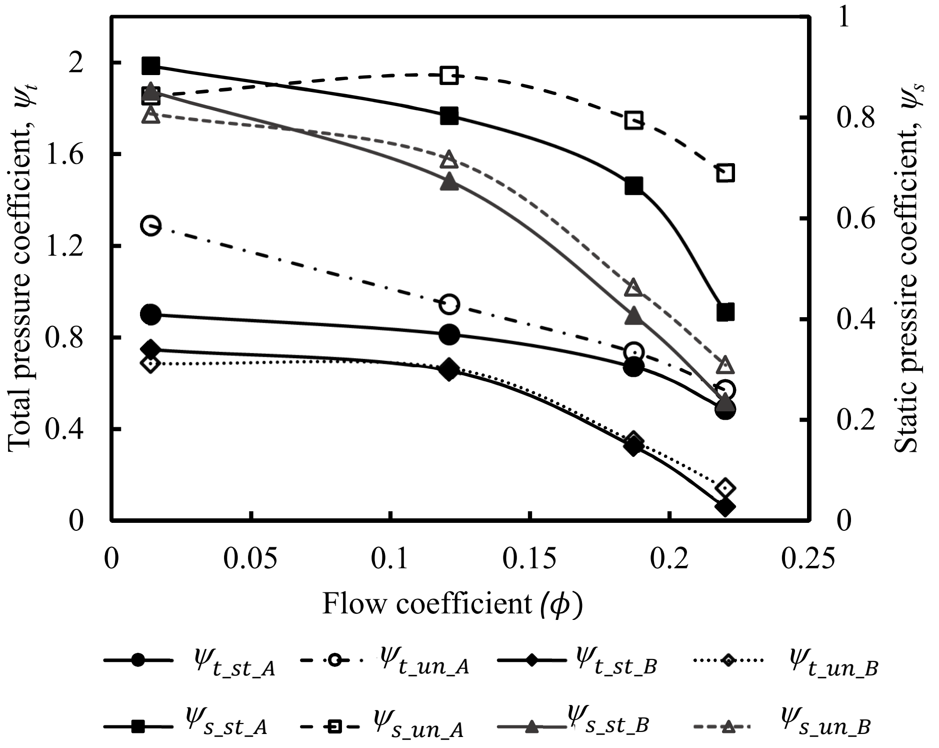

(a) Pressure

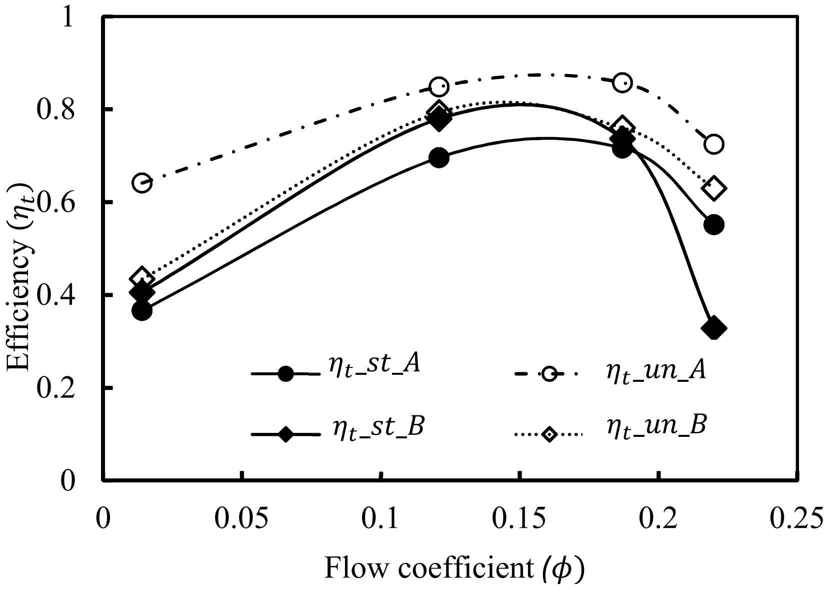

(b) Efficiency

Fig. 5.25 Fan performance

The impeller performances of the impeller ‘A’ and ‘B’ are shown in Fig. 5.25. The steady and unsteady flow characteristics of the impeller ‘A’ and ‘B’, the static and the total pressure coefficients show in Fig. 5.26 (a) and the efficiencies show in Fig. 5.26 (b).

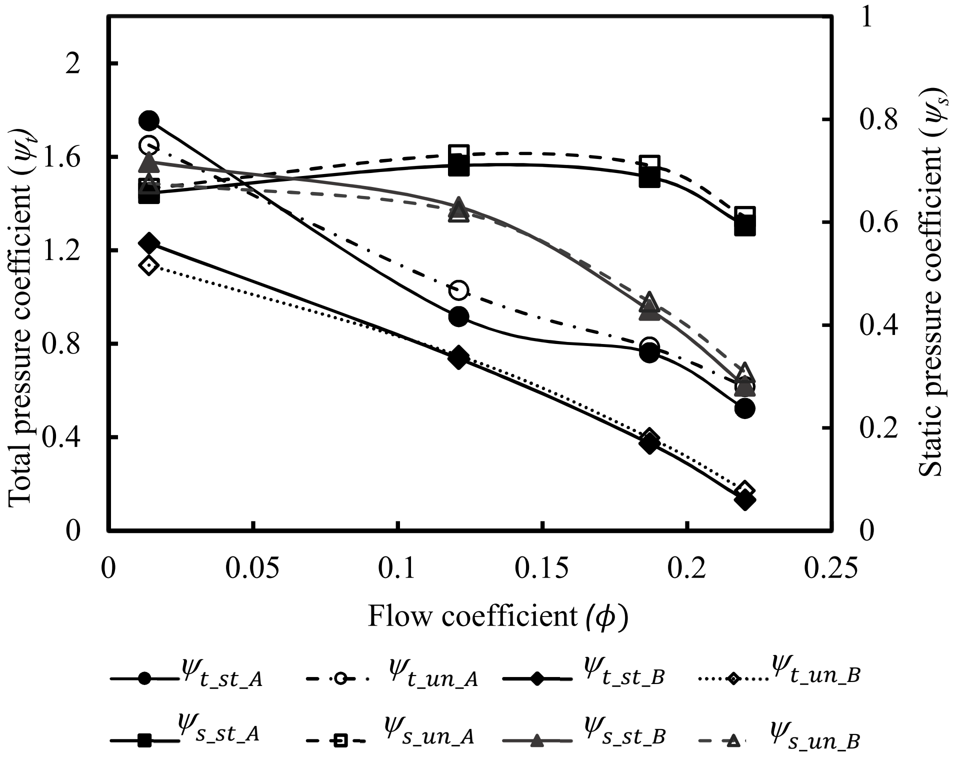

(b) Pressure

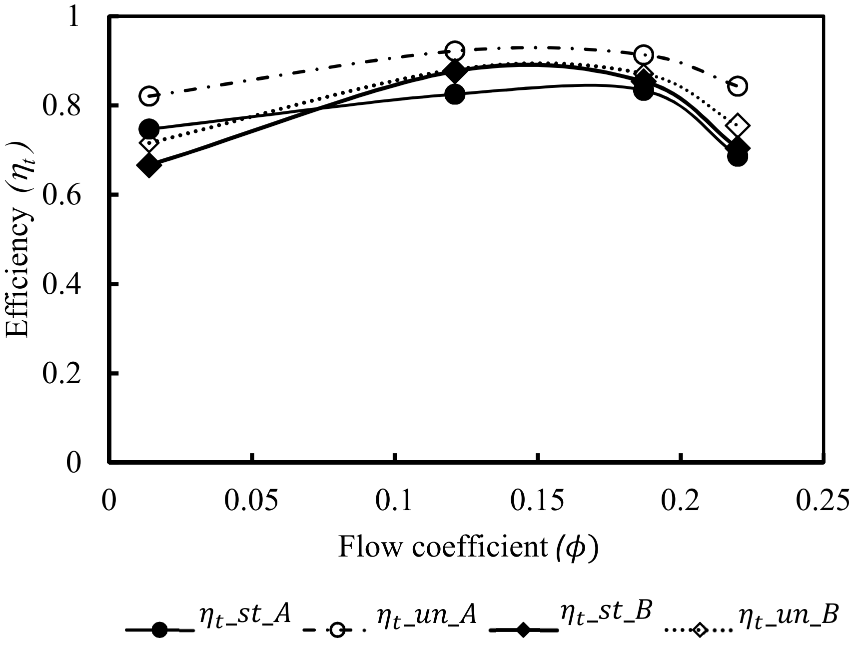

(b) Efficiency

Fig. 5.26 Impeller performance

The performance of static pressure and the total pressure coefficient of the impeller ‘B’ in steady simulation are almost the same in unsteady simulation. And for the case of the impeller ‘A’, the coefficients in steady simulation are almost same to the case of unsteady simulation. The total pressure coefficient of the impeller ‘A’ is higher than that of the impeller ‘B’ in all flow rate that is caused by the difference of the outlet angle of the impeller and the variation with flow rate is similar to the impeller ‘B’. But the variation of the static pressure coefficient of impeller ‘A’ with the flow rate is different from the case of the impeller ‘B’. The static pressure of the impeller ‘A’ is almost constant at wide flow rate but that of impeller ‘B’ is gradually decreased with the flow rate. Figure 5.26 (b) is the efficiency of the impeller. The efficiency of the impeller ‘A’ in steady simulation is lower about 0.1 than in unsteady simulation at all flow rate. The total pressure is almost same in both simulations but the blade load is different in steady and unsteady simulations. The efficiency of impeller ‘B’ is almost same in steady and unsteady simulations. The efficiency of the impeller ‘B’ in both steady and unsteady flow fields is higher than in the steady of the impeller ‘A’, but those values are lower than in the unsteady of the impeller ‘A’. This shows the difficulty of the decision of the impeller performance.

The casing performances, efficiency, are shown in Fig. 5.27. The casings have the impeller ‘A’ and the impeller ‘B’ which appreciate the casing performances by the steady and the unsteady. The casing efficiency in Fig. 5.27 is defined by the following equations, Eq. (5.4).

$$\eta_c = 1 + \frac{\Delta P_{t\_c}}{\Delta P_{t\_im}} \tag{5.4}$$

Where the ΔP_{t_c} and ΔP_{t_im} is pressure rise in casing and the impeller, respectively. In the casing, ΔP_{t_c} is always negative.

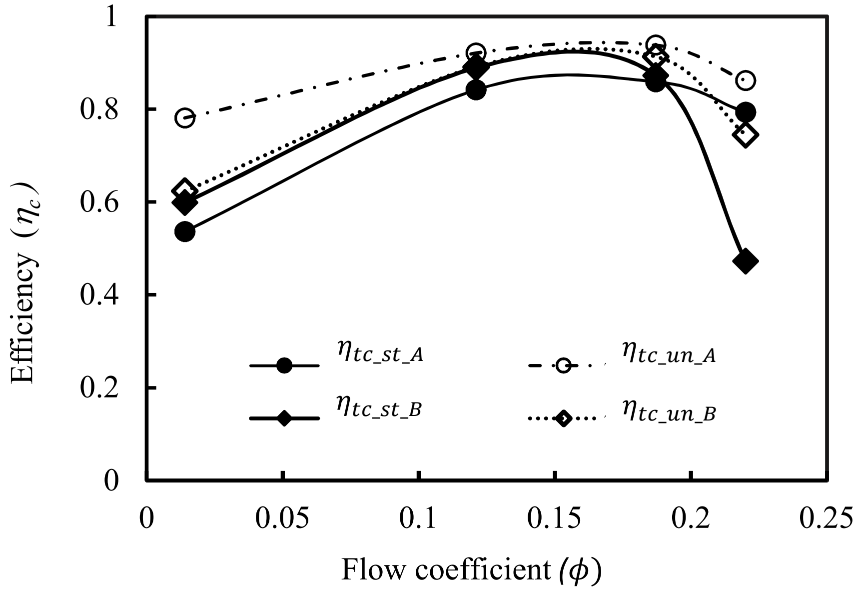

Fig. 5.27 Casing efficiency

The casing efficiency based on the total pressure is maximum at flow rate ($\phi = 0.187$) in all cases. The variation of the impeller ‘B’ is almost same in both simulations, except at large flow rate. At the impeller ‘A’ the difference between the steady and unsteady simulations are large, especially at the low flow rate. The difference of the impeller ‘A’ at design flow rate, ($\phi = 0.187$) is about 0.1. The difference of the fan efficiency is about 0.2 at impeller ‘A’ as shown in Fig. 5.25 (b), and the difference is caused by both the impeller and the casing efficiency difference.

5.3 Summary

According to Fig. 5.1 to Fig. 5.4, the non-uniform flow pattern dominants in the steady simulation for impeller ‘A’. Even though, the flow rate is increasing from the low flow to the high flow rate, the separation still occurs in the steady flow field. The separation doesn’t occur in the unsteady flow field in large flow rate. The uniform flow pattern generates

According to Fig. 5.5 to Fig. 5.8, the non-uniform flow pattern in the circumference of the impeller ‘A’ outflow generates in blade section B_4-B_6 from the steady simulation results. This is caused by the flow separation in the blade passage and the separation lead to become weak region in the casing back. From the unsteady simulation results, the internal flow pattern and circumferential flow pattern of the impeller ‘A’ is uniform in each blade passage.

According to Fig. 5.9 to Fig. 5.12, when the air enters in the impeller with the low flow rate ($\phi = 0.014$), the steady flow pattern is a big different from unsteady flow pattern. These steady flow pattern is absolutely the same with the unsteady flow pattern and it becomes the uniform flow pattern when the flow rate is large; i.e., the flow rate is between ($\phi = 0.121$) to ($\phi = 0.22$). The uniform flow pattern generates form the circumference of the impeller (impeller ‘B’) to the circumference of the casing.

According to the Fig. 5.13 to Fig. 5.16, the discrepancy of steady and unsteady simulation is cause by the process of flow from the inlet to outlet of the impeller. At the steady simulation, the impeller does not move in entire simulation time and the flow of the impeller passage is restricted in the fixed impeller passage. The blade load of the impeller ‘B’ is lower than the impeller ‘A’, and the separation of the boundary layer on the blade surface is hardly occurred. This flow characteristics makes small the difference between the steady and unsteady simulation. At the low flow rate, the fan exits pressure distribution in case of impeller ‘B’ is higher than these of impeller ‘A’. If the flow rate become large (at design flow rate and over this flow rate), the fan exit pressure in case of the impeller ‘B’ is lower than these of the impeller ‘A’.

According to Fig. 5.17 to Fig. 5.24, at the design flow rate, the steady and unsteady pressure distribution in the impeller ‘B’ is a little difference but it is big difference in the impeller ‘A’. In Fig. 5.21, static pressure distributions in the steady is large different at the low flow coefficients ($\phi = 0.014$). The non-uniform pressure distribution occurs in the circumference of the impeller. In the design flow and large flow rate, the pressure distribution is a little difference in each blade section of impeller ‘B’. The static pressure distribution of the impeller ‘B’ is lower than the impeller ‘A’.

In the mention above, the discrepancy of steady and unsteady simulation is caused by the process of flow from the inlet to outlet of the impeller. At the steady simulation, the impeller does not move in entire simulation time and the flow of the impeller passage is restricted in the fixed impeller passage. In the unsteady simulation, the impeller rotates during the flow passes through the blade passage and the inlet condition and outlet condition of the impeller are varied during the flow passing. This operates to average the flow in the impeller. The static pressure distribution in steady simulation is little difference with unsteady within the blade sections. This flow characteristics makes small the difference between the steady and unsteady simulation. The blade load of the impeller 'B' is lower than the impeller 'A', and the separation of the boundary layer on the blade surface is hardly occurred.

CHAPTER 6

CONCLUSION

In this research, the investigations on the effect of casing types, rectangular casing and scroll casing (RC casing and SC casing) on performance of centrifugal fan had been presented by experiment and computational simulation.

(1) The performances: the efficiency and the pressure of the rectangular casing fan is higher than that of scroll casing fan. The performance curve of the RC casing fan is slightly reduced at the wide range of the flow rate. At low flow rates, the performances of the impeller are not affected depend on the casing shape. Thus, the rectangular casing fan can be used with the wide range flow rate.

(2) The energy loss in the casing (RC casing) is smaller than that of casing (SC casing). The total loss in the SC casing is greater than RC casing at large flow rate, the shape of casing geometry is influence on fan loss and the efficiency of fan.

(3) The circumferential flow characteristics of the impeller and the casing of the RC casing is non-uniform in each flow rate and the variation with the flow rate is slightly varied. The flow characteristics of the SC casing is uniform only at design flow rate but the variation with the flow rate is large. Thus, the performance of the RC casing fan is not varied with flow rate and is better at large flow rate.

Next, it is discussed to the impeller of the circumferential variation to the simulation condition. The unsteady simulation is discussed compared to the steady simulation. The two types blades, large blade load and small one is compared. The following results are obtained.

(1) The results of the fan performances are different in steady and unsteady simulation at the large blade load that the flow separation occurs in the blade passage.

(2) The circumferential variation of the flow characteristics, flow separation from the blade surface becomes large in steady simulation. That is, the effect of the local flow condition is large in the steady simulation.

(3) The flow pattern in steady simulation is strongly influenced to the local condition compared to the unsteady simulation. In steady case, the impeller does not move in entire simulation time, but in the unsteady simulation, the impeller rotates during the flow passes through the blade passage. The velocity variation changes in each timestep. This fact should be considered in case of the performance analysis for the turbomachinery.

(4) The differences of the flow characteristics between steady and unsteady simulation is not so large at the small blade load. When the flow separation doesn't occur in the blade passage, the influence of the circumferential variation of casing geometry is comparatively small.

References

[1] Yokoi, Y., Inagaki. S.: Experimental Study of Flow Feature in Spiral Casing of Turbo Fan, J. of TSJ, "Turbomachinery", Vol.33-4, pp.241-249, (2005).

[2] Qi, D., Zhang, Y., Wen, S., and Liu, Q.: Measurement and Analysis of Three-Dimensional flow in a Centrifugal Fan Volute with Large Volute Width and Rectangular Cross Section, IMechE, Vol.220, pp.133-153, (2006).

[3] Yamazaki, Komatsu, S., Obata, T., and Yokoyama, S.: Investigating of Flow Pattern in a Backward-Curved Fan and Influence of Its Fan Shape on performance and Noise, Trans. of JSME, Vol.65-636, pp.2770-2776, (1999).

[4] Yu, Li, S., He, W., Wang, W., Huang, D., and Zhu, Z.: Numerical Simulation of Flow Field for a Whole Centrifugal Fan and Analysis of the effect of Blade Inlet Angle and Impeller Gap, HVAC & R Research, Vol.11-2, pp.263-283, (2005).

[5] Jeona, W.H., and Leeb, D.J.: A numerical study on the flow and sound fields of a centrifugal impeller located near a wedge, J. Sound, and Vibration, Vol.266, pp.785-804, (2003).

[6] Behzadmehr, A., Piaud, J.B., Oddo, R., and Mercadier, Y.: Aero-Acoustical Effects of Some Parameters of a Backward–Curved Centrifugal Fan Using, DoE, Vol.12-2, pp.353-365, (2006).

[7] Yamashita, S.: Silent and Super Link System of Ceiling Recessed Type Packaged Air Conditioner, Refrigeration, Vol.67-776, pp.622-627, (1992).

[8] Hayashi, H., Nakamura, K.: Flow Characteristics of Turbo Fan with Rectangular Casing, J. of TSJ, "Turbomachinery", Vol. 39, No. 10, p. 624-631, (2011).

[9] Kodama, Y., Hayashi, H., Sanagi, T., and Kinoshita, K.: Noise Generated by Centrifugal Fan without Scroll Casing (Effects of the distance between the leading edge of blades and the wall of mouthpiece, the geometry at the outlet of the bellmouth and the gap of mouthpiece), Trans. of JSME, Vol. 63-613, pp.3025-3032, (1997).

[10] Skin Friction Coefficient -- CFD-Wiki, the free CFD (https://www.cfd-online.com/Wiki/Skin_friction_coefficient#References)